SOUTHWEST RESEARCH INSTITUTE

6220 CULEBRA ROAD • POST OFFICE DRAWER 28510 • SAN ANTONIO, TEXAS, USA 78228-0510 • (512) 684-5111 • TELEX 244846

ANALYSIS OF CHECK VALVE SWING ARMS

Task 1
Evaluation of Commercial Swing Arms
FINAL REPORT

SwRI Project No. 06-3893-100

to

TU Electric Co.
Comanche Peak S.E.S.
P.O. Box 1002
Glen Rose, TX 76043

March 1991

APPROVED:

Gerald R. Leverant, Director
Materials & Mechanics Department

Prepared by:

H. C. Burghard, Jr.
M. L. Bartlett

Thomas C. Tybovich, Manager
Quality Assurance

SAN ANTONIO, TEXAS
HOUSTON, TEXAS • DETROIT, MICHIGAN • WASHINGTON, DC

Table of Contents

LIST OF TABLES

LIST OF FIGURES

(Continued)

LIST OF FIGURES (Continued)

(Continued)

LIST OF FIGURES (Continued)

(Continued)

LIST OF FIGURES (Continued)

1.0 INTRODUCTION

1.1 Background

A program was undertaken at the Comanche Peak Steam Electric Station (CPSES) to evaluate the suitability for service of the swing arms in a specific group of check valves supplied by a single manufacturer and installed at the station. Comanche Peak is a nuclear-powered electric generation station consisting of two 1150 Mw units. The valve swing arms selected for testing in the program were removed from valves ranging in size from 3-inch to 16-inch. The particular valves involved were from a representative population of Unit 1 and Unit 2 systems. A schematic diagram of one type of check valve, illustrating the overall configuration and function of the swing arms, is shown in Figure 1-1.

The material of the valve bodies from which the sample swing arms were obtained is cast stainless steel (Type 316) in three cases and cast carbon steel for the remainder. The swing arm material was selected by the valve manufacturer and called out on vendor drawings as 17-4PH (H1100), but there are no certified test or inspection records for these components. Actual detailed material specifications were provided from the drawing for 4-inch swing arms. The manufacturing drawings for one of the 4-inch valves called out the swing arm material as 17-4PH per AMS 5398 [1], heat treated to condition H1100 per MIL-H-6875 [2]. The current ASTM specification for cast 17-4PH stainless steel is A 747 CB7Cu-1 [3].

As part of the overall CPSES program, certain nondestructive inspections, mechanical properties tests, and metallurgical evaluations of the selected swing arms were performed at Southwest Research Institute (SwRI). The procedures employed and the results obtained in those inspections and evaluations are presented in this report.

1.2 Sample Materials

A total of 16 intact swing arms were furnished to SwRI by CPSES for the purposes of this program. The particular valve sizes included in the group were as follows:

2 - 16-inch	3 - 6-inch
1 - 10-inch	4 - 4-inch
2 - 8-inch	4 - 3-inch

A listing of the individual samples with their CPSES identification numbers and the corresponding sample numbers assigned for the purposes of the laboratory evaluations is presented in Table 1-1.

In general, the swing arms are configured as a curved bar of rectangular cross section with cylindrical bosses at each end. The axes of the two bosses are oriented perpendicular to one another with one boss drilled to accept a hinge pin and the other drilled to accept the valve disk stud. Photographs of selected samples illustrating the general sizes and configurations are shown in Figures 1-2 and 1-3. Photographs of each individual sample and diagrams showing their principal dimensions are contained in Appendix A.

1.3 Scope of Laboratory Evaluation

The laboratory evaluations were organized to establish the mechanical properties and the metallurgical characteristics of all the sample swing arms. Each sample was inspected visually and at low magnification (10-50X) and by radiographic procedures.* Fracture toughness tests were performed on compact tension specimens from all 16 samples, uniaxial tensile tests were performed on selected samples and hardness measurements were made on all samples. Metallographic examinations of selected sections from all samples were performed to identify microstructural features and to characterize certain flaws identified in the nondestructive inspections. These examinations also served to expose any flaws in the arms at the transition to the valve boss disk** which might have gone undetected in the nondestructive inspections. In addition, the bulk chemical compositions were determined for all 16 samples.

---

* Liquid penetrant inspections of all 16 swing arm samples were performed at CPSES prior to shipment to SwRI.

** This region was identified as the zone of highest in-service bending stresses in earlier investigations at CPSES.

TABLE 1-1

SWING ARM SAMPLE IDENTIFICATION

Valve Size	SwRI Sample No.	CPSES Valve No.
16-in.	239	2CT-0025
	240	2CT-0077
10-in.	255	2CC-0317
8-in.	242	2AF-0038
	243	2AF-0167
6-in.	244	2AF-0014
	256	2FW-0198
	257	2CH-0024
4-in.	245	1AF-0098
	258	1AF-0093
	259	1AF-0101
	260	1AF-0106
3-in.	246	1CH-0346
	261	2CC-003
	262	2CC-004
	263	XDD-0048

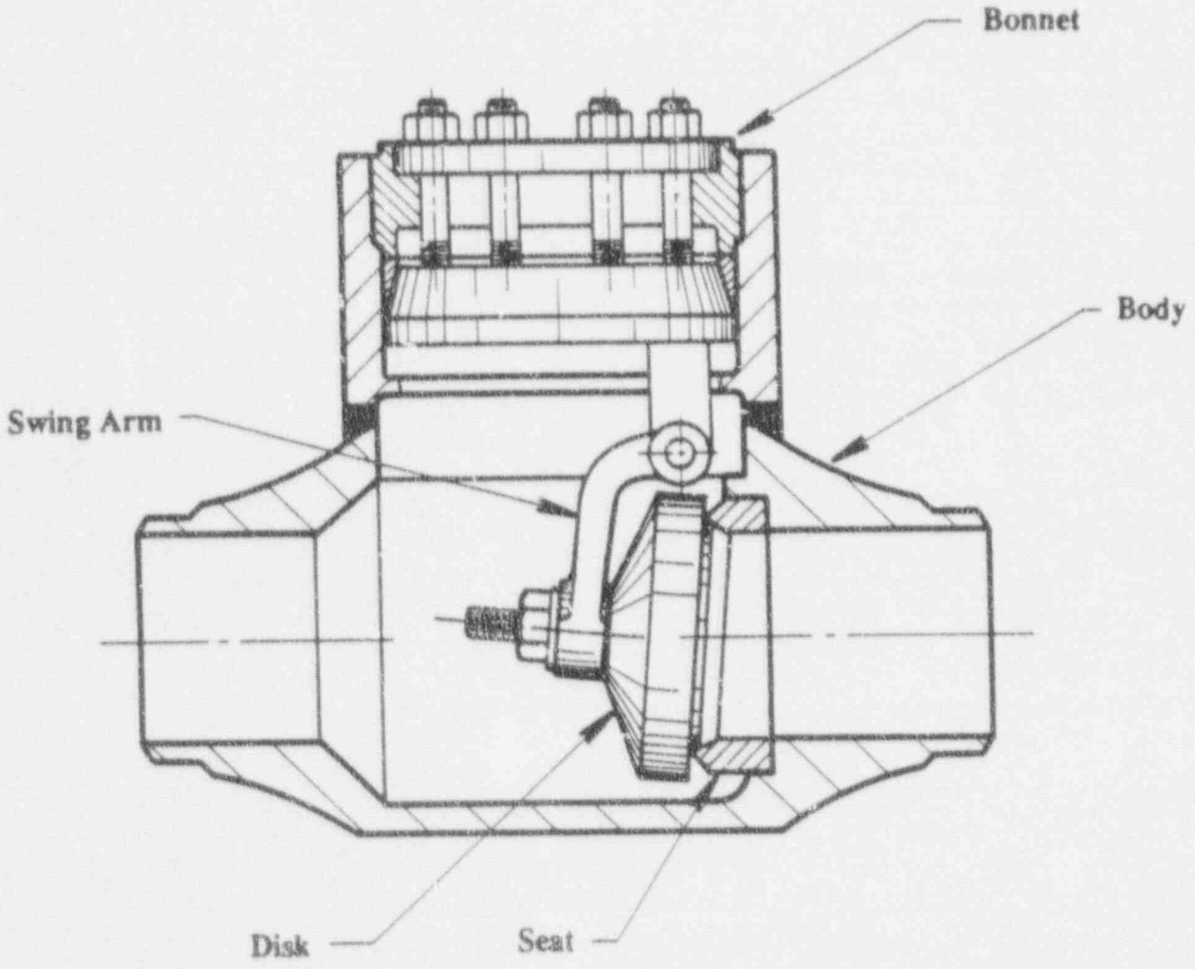

FIGURE 1-1. SCHEMATIC DIAGRAM OF CHECK VALVE. Valve shown employs a pressure-seal bonnet. Others in the system employ bolted bonnets. The general configuration and function of the swing arms are similar for both types.

45433

FIGURE 1-2. SWING ARM FROM 16-INCH CHECK VALVE.
Sample No. 240.

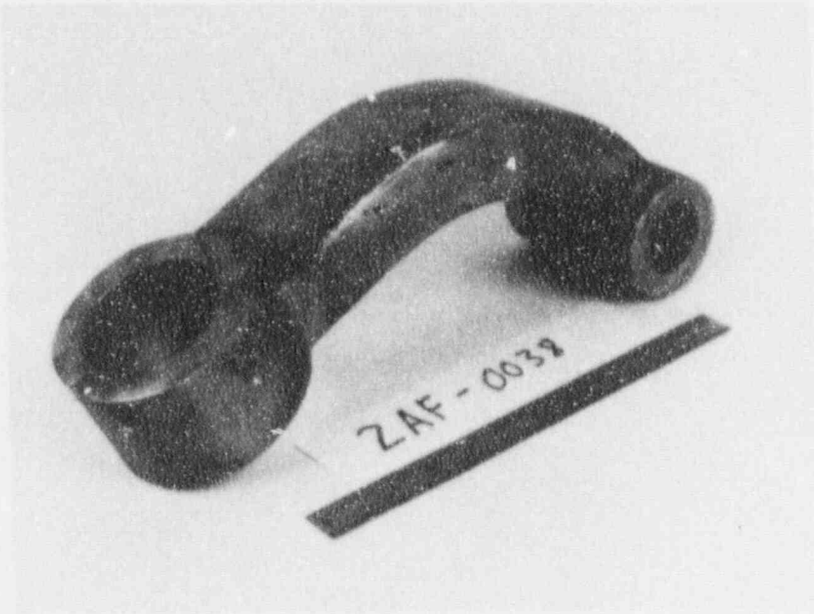

45815

(a) Sample No. 242. 8-inch check valve.

46525

(b) Sample No. 258. 4-inch check valve.

FIGURE 1-3. SWING ARM SAMPLES

2.0 NONDESTRUCTIVE INSPECTIONS

All of the swing arm samples were inspected visually and by liquid fluorescent penetrant (LP) techniques. In those cases where the visual or LP inspections indicated possible significant flaws, the areas of interest were examined at low magnification (10-50X) in the stereomicroscope. Each individual sample was also radiographed to provide for identification of internal flaws.

In the course of the visual inspection, each individual sample was immersion etched in Fry's reagent* to highlight any major variations in structure and possible weld repairs.

2.1 Visual and Liquid Penetrant Inspections

In general, no significant external flaws were noted in the visual inspections. In certain cases, (mainly the larger arms), relatively deep surface pits were noted but these were generally identified as smooth, open features in the stereomicroscope examinations and could not be classified as detrimental flaws.

Weld repairs were evident on most of the large arms and in several cases considerable weld repair had been performed on the disk attachment bosses. The etching response of the weld deposits suggested that the filler material was an austenitic stainless steel (Type 308 or similar). A summary of the observed weld repairs is presented in Table 2-1 and photographs of representative examples are shown in Figures 2-1 and 2-2. In the case of the two 16-inch swing arms, the weld repairs in the disk attachment boss were such that, after final machining, the weld deposit extended completely through the radial thickness of the boss [Figure 2-1(a)]. Metallographic examinations established that the depths of all other weld repairs were on the order of 0.06-inch.

The liquid penetrant inspections performed at CPSES did not produce any recordable flaw indications. Certain surface features did retain penetrant to a slight degree, however, and these were marked for stereomicroscope examination

2.2 Radiographic Inspections

All 16 swing arms were inspected radiographically. The inspections were performed with an X-ray source operated at 160-290 KV and 4-5 Ma. Either Kodak T or Kodak AA film was

---

* ASTM E 407, No. 79. 40 ml HCl + 5 g $CuCl_2$ + 30 ml H_2O + 25 ml ethanol

used and the source to film distance for all exposures was 27 inches. In all cases except for Sample No. 255, the radiographs were either free of recordable indications or exhibited only isolated or scattered minor flaw indications in the arm portion of the sample. These were classified as Level 1 inclusions or voids to Level 3 shrinkage in accordance with ASTM E 446 reference radiographs. The radiograph for Sample No. 255 (10-inch arm) exhibited larger flaw indications which were classified as Level 6 shrinkage. These were located in the straight portion of the arm approximately 3 inches from the disk attachment boss. A summary of the radiographic inspection results is given in Table 2-2.

TABLE 2-1

SUMMARY OF WELD REPAIRS

Valve Size	Sample No.	Location and Extent of Repair
15-in.	239 240	Through-thickness repairs in disk attachment boss.
10-in.	255	Shallow repairs in disk attachment boss and arm.*
8-in.	242 243	Shallow repairs in disk attachment boss and arm.
6-in.	244	Shallow repairs in disk attachment boss and arm.*
	256 257	No repairs.
4-in.	245	Single repair in arm at disk attachment boss.
	258 259 260	No repairs.
3-in.	246	No repairs.
	261	Single repair in arm.
	262 263	Shallow repairs in disk attachment boss.*

* Metallographic examinations established that those welds designated as "shallow" were on the order of 0.06-in. depth.

TABLE 2-2

RADIOGRAPHIC INSPECTION RESULTS

Valve Size	Sample No.	Radiographic Indications*
16-inch	239	Two Level 3 CA shrinkage. Scattered Level 1, CA shrinkage.
	240	Two Level 3 CD shrinkage.
10-inch	255	Several Level 6 inclusion/void indications.
8-inch	242	Isolated Level 2, CA shrinkage.
	243	Scattered Level 1 inclusions and Level 2, CA shrinkage.
6-inch	244	Scattered Level 2 CA shrinkage and Level 1 inclusions/voids.
	256	Single Level 1 CA shrinkage and scattered Level 1 inclusions/voids.
	257	Isolated Level 1 inclusion/void.
4-inch	245 258	No recordable indications.
	259	Scattered Level 1 inclusions/voids.
3-inch	246	No recordable indications.
	260 261	Isolated Level 1 inclusions/voids.
	262 263	No recordable indications.

* Indications are classified in accordance with ASTM E 446 reference radiographs. [Ref. 8, pg. 8-1]

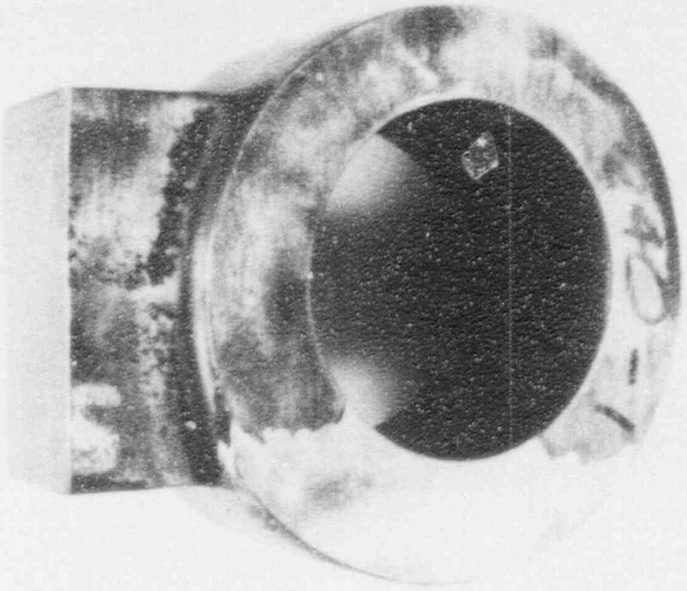

46222 (a) Sample No. 240 (16 in.). Top View.

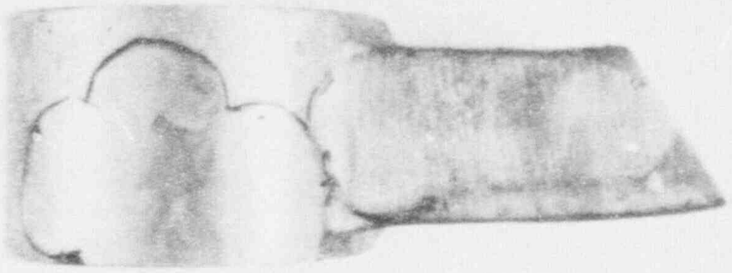

44077 (c) Sample No. 242 (8-in.)

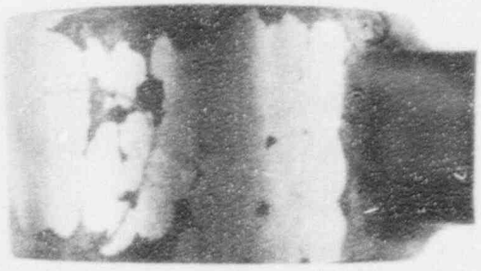

47083 (b) Sample No. 255 (10 in.).

FIGURE 2-1. WELD REPAIRS IN SWING ARMS.
Immersion etched in Fry's reagent.

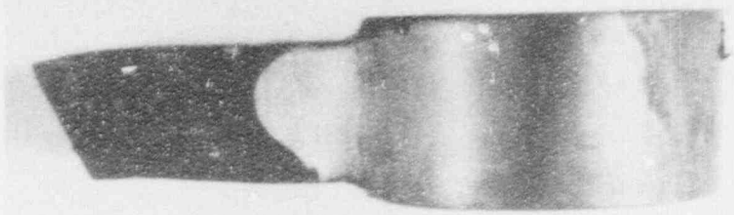

47177 (a) Sample No. 244 (6 in.).

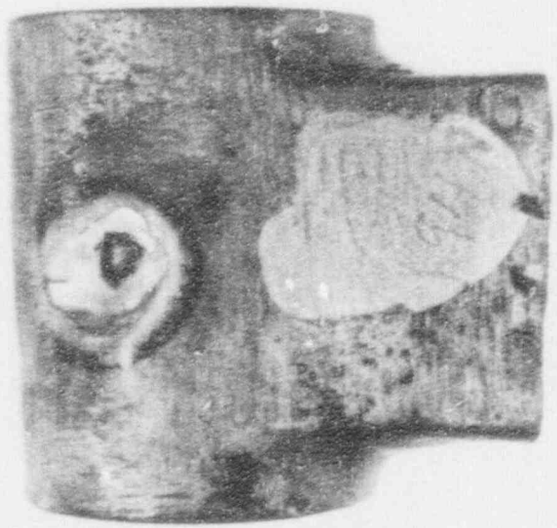

47118 (b) Sample No. 261 (3 in.). Top view.

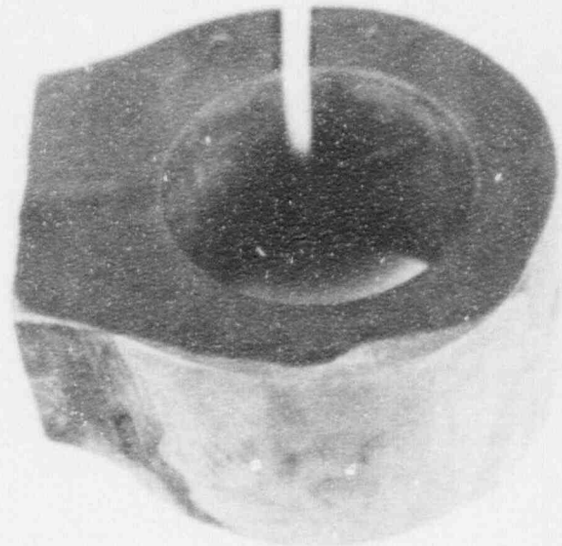

47169 (c) Sample No. 262 (3-in.). Top view. Saw cut and punch marks on far side were made for residual stress measurement. See Section 3.3.

FIGURE 2-2. WELD REPAIRS IN SWING ARMS. Immersion etched in Fry's reagent.

3.0 MECHANICAL PROPERTIES, COMPOSITION AND RESIDUAL STRESS

3.1 Hardness and Tensile Properties

Conventional Rockwell hardness measurements were made on longitudinal sections from each of the 16 swing arms. The sections were selected from those cut for metallographic examination (see Section 4.0) and were all located at the junction of the arm with the disk attachment boss. In those cases where multiple sections were examined, five hardness measurements were made on each of two sections, one near the edge and one near the centerline of the arm. In cases where only one section was taken, the hardness was measured on the side of the specimen nearest the centerline. In all cases, the section was ground to a 400 grit finish prior to measurement. The results of the hardness measurements are presented in Table 3-1.

The average hardness values for the entire group of samples, except for No. 260, were in the range of HRC 28-40 (BHN 271-372).* These values equal or exceed the minimum value of HRC 28 (BHN 271) specified by ASTM A 747 for CB7Cu-1 (H1100) cast stainless steel.** There were no significant variations in hardness among duplicate sections of any one sample or among various locations on any one section. The range of approximate ultimate tensile strengths corresponding to the range of measured hardness values is 130-182 ksi.

The hardness of Sample No. 260 was measured as HRC 21-HRB 96 (BHN 224). This value is substantially below the range of values for the other 15 samples and below the specified minimum hardness for CB7Cu-1 (H1100) material. The corresponding approximate ultimate strength for this hardness level is 106 ksi. It is of interest to note that the metallographic examination established that Sample No. 260 was improperly heat treated (see Section 4.1).

---

* The majority of the 15 samples exhibited hardness values in the range of HRC 35-40 (BHN 322-372).

** The hardness values and strength requirements specified for A 747 CB7Cu-1 (H1100) material are cited in this section for reference only. The swing arms were not manufactured to specifically conform to that specification. Neither AMS 5398 or MIL-H-6875 specify hardness or strength requirements for the H1100 condition.

Hardness measurements were also made on two laboratory heat-treated specimens which had been cut from one of the 16-in. swing arms. One specimen (No. 239-4a) had been given a complete heat treat cycle including homogenization, solution annealing and aging to produce the H1100 condition. The second specimen was simply reaged at 1100°F. In both cases, a slight increase in hardness was noted (HRC 35-36 vs. HRC 32, see Table 3-1). This change in properties demonstrated that the thermal treatment that produced the initial condition was somehow different from the laboratory full-cycle treatment and that the initial condition was not fully aged. These observations are consistent with the fact that both of the 16-in. arms exhibited a unique microstructure (see Section 4.1). However, it should be noted that the initial hardness is consistent with the H1100 condition and that the microstructure indicates a heat-treated condition (not as-cast).

Uniaxial tensile tests were performed on specimens from four of the swing arm samples. The particular samples selected for testing were those where sufficient material for tensile specimens remained after removal of the fracture toughness specimen blanks. These included one 16-in., two 8-in., and one 6-in. arm. The tests employed sub-size, round specimens per ASTM A 370 with 0.25-in. dia. x 1.0-in. lg. gage sections. The results are presented in Table 3-2. In two cases (Sample Nos. 239 and 243), the measured tensile properties conformed to the requirements of ASTM A 747 for cast CB7Cu-1 stainless steel in the H1100 condition.

The yield strength for Sample No. 242 was below the minimum value specified for CB7Cu-1 (H1100) material (104.5 ksi vs 110.0 ksi) while the ultimate strength was relatively high (174.6 ksi vs 135.0 ksi min.). The large difference between the ultimate and yield strength is unusual for cast 17-4 (H1100) material. In the case of Sample No. 244, the yield strength met the minimum specified by A 747 CB7Cu-1 (111.7 ksi vs 110.0 ksi) but the ultimate strength was below the minimum value required by that specification (129.1 ksi vs. 135.0 ksi).

3.2 Chemical Composition

Chemical analyses were performed on specimens from each of the 16 samples to determine the bulk chemical composition. Particular care was exercised in the removal of the individual specimens to avoid inclusion of any repair weld deposits. In one case, an additional

specimen containing only weld metal was analyzed. The results of the analyses are listed in Table 3-3. The composition limits specified by A 747 CB7Cu-1 and AMS 5398 and those for Type 308 austenitic stainless steel welding filler are included in the table for comparison. The compositional limits of A 747 CBCu-1 and AMS 5398 do not correspond exactly. The principal difference is that the maximum chromium content for AMS 5398 is lower by 1% (16.70% vs. 17.70%). The composition limits do overlap, however, so that simultaneous conformance to both specifications is possible.

The compositions of 10 of the sixteen samples conformed to the requirements of A 747 CBCu-1 and AMS 5398 except for a few minor variations.* Five of the remaining six samples (Nos. 239, 240, 257, 262, 263) had chromium contents slightly below the minimum values required by the two specifications cited.**

In the case of Sample No. 260, the nickel content was substantially above the specified maximum (6.12% vs 4.70% max.) and the copper was below the minimum (1.96% vs 2.50% min.).

The composition of the weld deposit sample is completely consistent with the specified composition for Type 308 stainless steel bare filler wire.

3.3 Residual Stress

The level of residual stress in the disk attachment boss was investigated by saw cutting the boss and measuring the opening or closure of the cut. In this procedure, small punch marks were made on the top of the boss on each side of a position 90° from the long axis of the arm. The initial spacing of the punch marks was measured and a saw cut was made on the boss centerline between the marks. The spacing of the marks was measured again after the saw cut. The typical locations of the punch marks and saw cut are shown in Figure 2-2.

---

* Minor deviations were noted in the nickel or chromium contents for Samples No. 255 and 256 but the values determined were only slightly outside of the range on the specifications considering the product analyses allowances. These deviations are not considered as significant.

** Comparison with the requirements of A 747 CB7Cu-1 is made for reference only. The swing arms were not manufactured in strict accordance with that specification.

The spacing measurements obtained for each sample are listed in Table 3-1. Over the entire group of samples, the maximum opening observed was 0.003-inch and the maximum closure noted was 0.004-inch. A first approximation of the residual stress in the boss ring is given the following formula.*

$$\sigma_{max} = \frac{Et}{\pi(1-\nu^2)} \cdot \frac{\Delta C}{D_i + \Delta C/a}$$

where

E = modulus of elasticity

ν = Poisson's ratio

D_i = initial diameter

ΔC = Opening or closure

t = thickness of ring

The residual stress values calculated in this manner are also listed in Table 3-4. In the case of 10 of the 16 samples, the indicated level of residual stress (tension or compression) was only 1.0 ksi or less. Of the remaining six samples, the maximum tensile residual stress indicated was 3.6 ksi and occurred for one of the 4-inch arms (Sample No. 245). The maximum compressive stress indicated was 3.8 ksi and occurred in one of the 6-inch arms.

In view of the fact that these approximated values are small relative to anticipated in-service stress,** no further evaluation of the residual stress was made.

---

* Based on elastic stress formulas for a thin ring considering the opening or closure as a change in circumference.

** See Section 5.0.

TABLE 3-1

HARDNESS DAT

Valve Size	Sample No.	Hardness - HRC											
		Center						Edge					
		1	2	3	4	5	Avg.	1	2	3	4	5	Avg.
16-in.	239	30	30	33	32	34	32	37	35	37	37	36	36
	240		37	37	38		37		37	37	36		37
	239-4a*	34	33	35	36	34	35	--	--	--	--	--	--
	239-4b**	36	36	36	36	37	36	--	--	--	--	--	--
10-in.	255	40	38	39	41	40	40	39	41	39	39	42	40
8-in.	242	39	38	41	39	40	39	30	39	40	39	37	39
	243	39	41	41	40	41	40	--	--	--	--	--	--
6-in.	244	30	30	31	31	31	31	27	29	30	28	28	28
	256	34	33	34	35	35	34	32	32	30	32	31	31
	257	41	40	39	42	39	40	38	38	39	39	39	39
4-in.	245	34	35	34	34	36	35	36	37	34	38	37	36
	258	33	33	34	33	34	33	28	29	32	33	31	31
	259	35	35	34	34	35	35	33	34	33	34	34	34
	260	21	22	21	21	20	21	97†	95†	97†	96†	96†	96†
3-in.	246	30	32	32	32	36	32	31	32	33	36	30	32
	261	36	34	36	36	36	36	35	34	35	37	35	35
	262	36	35	35	35	37	36	31	34	31	33	31	32
	263	31	35	36	35	36	35	31	34	37	36	35	35

* Reheat treated specimen (2150°F 2 hrs., FC to 1900°F 30 min., AC; 1100°F 4 hrs., AC)
** Reaged specimen (1100°F 4 hrs., AC)
† Rockwell B scale (HRB)

TABLE 3-2

TENSILE PROPERTIES DATA

Valve Size	Sample No.	Gage Section	0.2% Yield Strength - ksi	Ultimate Strength - ksi	Elongation %	Reduction of Area - %
15-in.	239	0.25-in. x 1.0-in.	129.5	151.8	17.0	43.5
8-in.	242		104.5	174.6	8.0	12.4
	243		148.2	174.5	11.0	28.5
6-in.	244		111.7	129.1	14.0	30.6
ASTM 747 CB7Cu-1 (H1100)*			110.0 min.	135.0 min.	9 min.	--

* The tensile properties specified for A 747 CBCu-1 material are listed for reference only. The swing arms were not manufactured in strict conformance to that specification.

TABLE 3-3

CHEMICAL COMPOSITION

Valve Size	Sample No.	Composition - wt.%										Conforms** to listed Specs.
		C	Mn	Si	Ni*	Cr*	Mo	Cu	Cb	P	S	
16-in.	239	0.06	0.14	0.18	4.07	14.54	0.10	3.05	0.11	0.016	0.014	N
	240	0.06	0.20	0.36	3.93	14.85	0.09	3.02	0.17	0.015	0.013	N
10-in.	255	0.05	0.25	0.98	4.97	15.27	0.12	3.19	0.21	0.021	0.018	N
8-in.	242	0.04	0.48	0.58	4.15	15.81	0.07	2.99	0.25	0.013	0.010	Y
	243	0.05	0.32	0.61	4.12	15.31	0.10	3.04	0.21	0.021	0.016	Y
6-in.	244	0.06	0.45	0.54	4.32	16.85	0.28	2.79	0.17	0.020	0.018	Y
	256	0.04	0.63	0.64	3.80	15.30	0.17	3.02	0.22	0.017	0.004	Y
	257	0.05	0.22	0.23	3.83	15.08	0.07	2.87	0.18	0.013	0.013	N
4-in.	245	0.04	0.50	0.64	4.06	16.20	0.10	3.09	0.23	0.020	0.013	Y
	258	0.06	0.45	0.52	3.76	15.84	0.10	2.86	0.26	0.016	0.011	Y
	259	0.05	0.45	0.52	3.70	15.94	0.11	2.86	0.27	0.016	0.011	Y
	260	0.06	0.37	0.24	6.12	16.47	0.84	1.96	0.16	0.016	0.012	N
3-in.	246	0.04	0.57	0.54	4.22	16.06	0.17	3.22	0.24	0.024	0.012	Y
	261	0.05	0.38	0.50	3.83	15.50	0.10	2.95	0.22	0.014	0.011	Y
	262	0.05	0.20	0.22	3.89	14.88	0.11	2.93	0.18	0.013	0.012	N
	263	0.06	0.21	0.19	3.80	14.84	0.11	2.94	0.17	0.013	0.012	N
	ASTM A 747 CB7 Cu-1	0.07 max	0.70 max	1.00 max	3.60-4.70	15.50-17.70	--	2.50-3.20	0.15-0.35	0.035 max	0.03 max	
	AMS 5398†	0.06 max	0.70 max	0.50-1.00	3.60-4.70	15.50-16.70	--	2.50-3.20	0.01 0.35	0.04 max	0.03 max	
	240-W††	0.06	1.02	0.38	9.47	20.33	0.05	0.13	0.01	0.021	0.005	--
	Type 308 SS Filler Wire	0.08 max	1.00-2.50	0.30-0.65	9.00-11.00	19.50-22.00	0.75 max	0.75 max	--	0.03 max	0.03 max	--

* Variation of 0.18% and 0.25% above the maximum and below the minimum specified values for Cr and Ni, respectively, are allowed for product analyses in accordance with ASTM A 781.

** Y = yes; N = no. Comparison to listed specifications is made for reference only. The swing arms were not manufactured in strict conformance to these specifications.

† AMS 5398D also specifies maximum contents for three other elements as follows: 0.05 max Al, 0.02 max Sn, 0.05 max N. Analyses were not performed for these elements.

†† Weld metal from repair zone.

TABLE 3-4

RESIDUAL STRESS

Valve Size	Sample No.	C-in.		AC in.	Approximate Stress - ksi
		Initial	Final		
16-in.	239	0.460	0.460	0	0
	240	0.524	0.523	-0.001	-0.6
10-in.	255	0.467	0.463	-0.004	-3.2
8-in.	242	0.501	0.500	-0.001	-1.0
	243	0.505	0.507	+0.002	+2.0
6-in.	244	0.451	0.447	-0.004	-3.8
	256	0.444	0.444	0	0
	257	0.459	0.459	0	0
4-in.	245	0.389	0.392	+0.003	+3.6
	258	0.440	0.440	0	0
	259	0.503	0.502	-0.001	-1.2
	260	0.532	0.532	0	0
3-in.	246	0.460	0.459	-0.001	-1.6
	261	0.590	0.591	+0.001	+1.6
	262	0.472	0.472	0	0
	263	0.522	0.524	+0.002	+3.1

4.0 METALLOGRAPHIC EVALUATION

Metallographic sections were taken from each of the 16 swing arm samples and examined to characterize the microstructural features in the region of the junction of the arm with the valve disk boss. In each case, the sections were taken completely through the thickness and in planes parallel to the long axis of the arm. One sample arm from each valve size group was sectioned at three locations; on the centerline and near each side of the arm (typically 0.1 inch from the outside). A schematic diagram illustrating this method of sectioning is shown in Figure 4-1. In cases where noticeable surface flaws were present, the location of one of the three sections was shifted to pass through the flaws. The remaining samples in each size group were sectioned at only one location. The single section was taken either at the centerline or at the location of visible surface flaws. The sections were ground and polished by conventional metallographic techniques, and examined at 50-1000x in the optical metallograph. These examinations were made both in the as-polished condition and after etching in Vilella's reagent.*

In addition to the systematic metallographic sectioning of all 16 samples, selected samples were sectioned in a manner to locate and characterize the microstructural features corresponding to selected radiographic flaw indications. Also, in cases where the routine sections revealed any linear-type flaw, the sections were sequentially ground and examined to establish the flaw size. The results of the metallographic characterization of specific flaws are presented in Section 5.0.

4.1 Microstructural Features

17-4PH stainless steel is a CrNiCu alloy steel in which the strength and hardness is developed by a combination of an austenite-to-martensite transformation followed by precipitation hardening. Typical heat treatments involve an initial solution heat-treatment at 1900°F to austenitize the steel and completely dissolve the copper. The part is quenched from the solutionizing temperature to develop a martensitic structure and then reheated to a temperature in the range of 900-1150°F to temper the martensite and precipitate a copper-rich phase within the martensite. The final hardness (and strength) depends on the precipitation treatment temperature, with the higher

* ASTM E 407 No. 80. 5ml HCl, 1 g picric acid, 100 ml ethanol.

hardness corresponding to the lower end of the temperature range. The typical microstructure for this alloy is a martensitic matrix with dispersed ferrite islands or stringers. The ferrite content can range from 1% to 8% depending on the composition of specific heats of material and the distribution of ferrite varies with fabrication processes. The copper-rich precipitate is submicroscopic in size for the lower aging temperatures and is only barely resolved by conventional metallography for the higher aging temperature.

In general, all but one of the swing arm samples were characterized by a martensitic-type matrix with dispersed ferrite. However, a wide variety of detailed microstructural features were observed among the sixteen samples. Representative microstructural features selected from the entire group of samples are illustrated in Figures 4-2 through 4-7. The particular microstructural features observed for each of the sixteen samples are presented in Appendix B.

The shape and distribution of ferrite varied considerably among the several samples and, in some cases, within a single section of one sample. Figure 4-2 illustrates both stringer-type ferrite and irregular ferrite islands observed in a single section. This difference is attributed simply to the orientation of particular grains relative to the plane of polish. The island features in Figure 4-2(b) probably represent cross-sectional views of stringers such as those in Figure 4-2(a). Another similar situation with ferrite stringers and discrete ferrite islands is shown in Figure 4-3. In this case, the stringers are thinner [Figure 4-3(a)] and the islands appear both as small, ellipsoidal shapes and larger irregular shapes. Again, the differences are consistent with different grain orientations.

Other variations in ferrite morphology are shown in Figure 4-4. Distinct intergranular network ferrite was often observed as in Figure 4-4(a). In other cases, the ferrite was distributed in long, thin, connected stringers to develop a cell-type network within the matrix, see Figure 4-4(b). These two types of ferrite distribution are also likely to be associated with grain morphology and orientation. Intergranular ferrite in an elongated grain structure, such as columnar grains in a casting, would present the network feature of Figure 4-4(a) in a plane oriented transverse to the elongated grains and the cell-type structure in a plane parallel to the grains. The nearly complete network evident in Figure 4-4(c) is simply another manifestation of intergranular ferrite.

In certain cases, the ferrite content of the microstructure was found to be very low. Examples illustrating that situation are shown in Figure 4-5. The ferrite content in those photomicrographs is on the order of 1% or less. Three of the four 3-inch swing arms (Nos. 261, 262, 263) were characterized by a very low ferrite content.

In general, all but one sample exhibited a distinctly martensitic matrix. In most cases, the matrix consisted of the usual tempered martensite with very fine-scale features and some evidence of a very fine precipitate. Examples of this type of matrix structure are shown in Figures 4-2 and 4-3. A similar tempered martensite structure is also evident in Figure 4-4(c) but, in this case, there is a variation in etching response with light etching in the immediate vicinity of the grain boundaries. This latter feature suggests a slight compositional variation across individual grains and probably indicates incomplete homogenization. The degree of variation in the case of Figure 4-4 is slight, however, and probably does not significantly influence the mechanical properties. Of all the 16 swing arms, 10 samples, including No. 255 (10-in.), No. 243 (8-in.), Nos. 244 and 256 (both 6-in.), Nos. 245, 258 and 259 (all 4-in.), and Nos. 246, 261, 262 and 263 (all 3-in.) exhibited the typical tempered martensite structure. In the case of three of the 3-inch samples, the structure was somewhat coarser with more distinct martensite needles (Figure 4-5).

Three samples [Nos. 239 (16-in.), No. 242 (8-in.) and No. 257 (6-in.)] exhibited a matrix with distinctly different microstructural features from those described above. Examples of this type of microstructure are shown in Figures 4-6(a) and 4-6(b). These structures are also martensitic but are characterized by coarse martensite needles some of which are extremely long in particular grains. These features probably reflect some differences in thermal history from the group described earlier, but it should be noted that there were no consistent, notable differences in composition or hardness of these three samples as compared to the entire group. The hardness of two of the samples (Nos. 242 and 257) did tend toward the high side of the hardness range, however.

One 16-in. sample (No. 240) exhibited mixed matrix features with typical tempered martensite and coarse, lath-type martensite at various locations in the same section. A photomicrograph from that sample is shown in Figure 4-6(c).

Although detailed differences in microstructure were observed among 15 of the 16 samples, all of the features may be classified as one or another variation of a martensitic structure. Most differences in ferrite morphology can be attributed to grain orientation effects and the variations in matrix structure. Although indicative of differences in thermal history (including heat treatment), these microstructural variations do not necessarily indicate significant differences in properties. This factor is born out by the generally uniform hardness values measured for the 15 samples. All of the microstructural features of this group are normal for heat-treated 17-4PH castings.

Sample No. 260 (4-in.) exhibited distinctly dendritic features as illustrated in Figure 4-7 (also see Figure B-14, Appendix B). The original dendritic grains of the as-cast condition were not evident but the dendritic pattern was retained in the etching response. This factor indicates that the sample was probably solution annealed after casting, but it is clearly evident that it was not adequately homogenized. Such a lack of homogenization would definitely affect response to subsequent heat treatment. It is of interest to note that the hardness of this sample was significantly lower that of the other 15 (HRB 96 vs. HRC 34-40) and that it was the one sample with a composition distinctly different from the typical 17-4 pH composition. Also, when tested with a small magnet, Sample No. 260 was noticeably less magnetic than the rest of the samples.

A general observation among all 16 swing arm samples was that shrinkage microvoids were observed at random locations in the metallographic sections. Typical examples are shown in Figures 4-8 and 4-9. These were always small (0.001-005 in. across) and generally isolated with a maximum concentration such as shown in Figure 4-9(a).* Microvoids of this type are a common feature for steel castings and are not considered as detrimental flaws.

4.2 Weld Repairs

Certain of the routine longitudinal sections (A-A, B-B and C-C in Figure 4-1) intersected weld repairs made in the vicinity of the valve disk boss. In addition, one metallographic

---

* Except for those cases where distinct radiographic indications were obtained. Those cases are treated separately in Section 5.1.

section was taken from the valve disk boss of Sample No. 240 for the specific purpose of examining the HAZ of the through-thickness weld repair. Photomicrographs from the several sections containing weld repairs are shown in Figures 4-10 through 4-13.

In every case, the weld metal exhibited a totally different etching response from that of the base metal. The only effect the etchant had on the welds was to delineate a columnar structure. Otherwise, the weld metal was unetched. These features indicate that the weld repairs were made with an austenitic stainless steel filler metal; not an alloy to match the 17-4PH base metal. This observation is consistent with the one case where chemical analysis positively identified the weld deposit as Type 308 austenitic stainless steel (see Section 3.2 and Table 3-3).

In the case of Sample No. 239 (16-in.), the microstructure of the HAZ consisted of equiaxed grains outlined by intergranular ferrite and light etching zones (Figure 4-10). This microstructure is totally different from that of the base metal remote from the weld. (Compare Figures 4-10 and B-1.) This factor, together with the strong columnar etching response of the weld metal, indicates that the casting was not heat treated (or was improperly heat treated) after the weld repair was made.

The microstructure of the HAZ in the other 16-in. swing arm (Sample No. 240) was also distinctly different from that of the base metal. In this case, the HAZ was characterized by equiaxed, martensitic grains either outlined by light etching boundaries or without distinct boundaries (see Figure 4-11). These features are distinctly different from the base metal which exhibited coarse martensitic features with distinct intergranular ferrite pools (compare Figure 4-11 and B-2). Again, this difference in structure between the base metal and the HAZ indicates that the casting was not properly heat treated after the weld repair.

In the case of the other three weld repairs examined, the microstructure of the HAZ was generally similar to that of the base metal. The HAZ of Sample No. 243 (8-in.) exhibited equiaxed grains outlined by intergranular ferrite essentially identical to the base metal structure [see Figure 4-12(a)]. Distinct ferrite stringers, typical of the base metal structures were present

immediately adjacent to the fusion lines in Samples No. 256 (6-in.) and No. 245 (4-in.), see Figures 4-12(b) and 4-13. These microstructural features at the weld repairs indicate that these three samples (No. 243, 246 and 256) were properly heat treated after the weld repairs.

It should be noted that, even though the weld was made with an austenitic filler metal, no specific defects such as voids, lack-of-fusion or underbead cracking were observed in those weld repairs which were sectioned. Also, Figure 4-13 illustrates that the weld repair in that case was only 0.06-in. deep. Similar, relatively shallow penetration was also observed in other cases of repairs at locations outside of the disk attachment bosses.

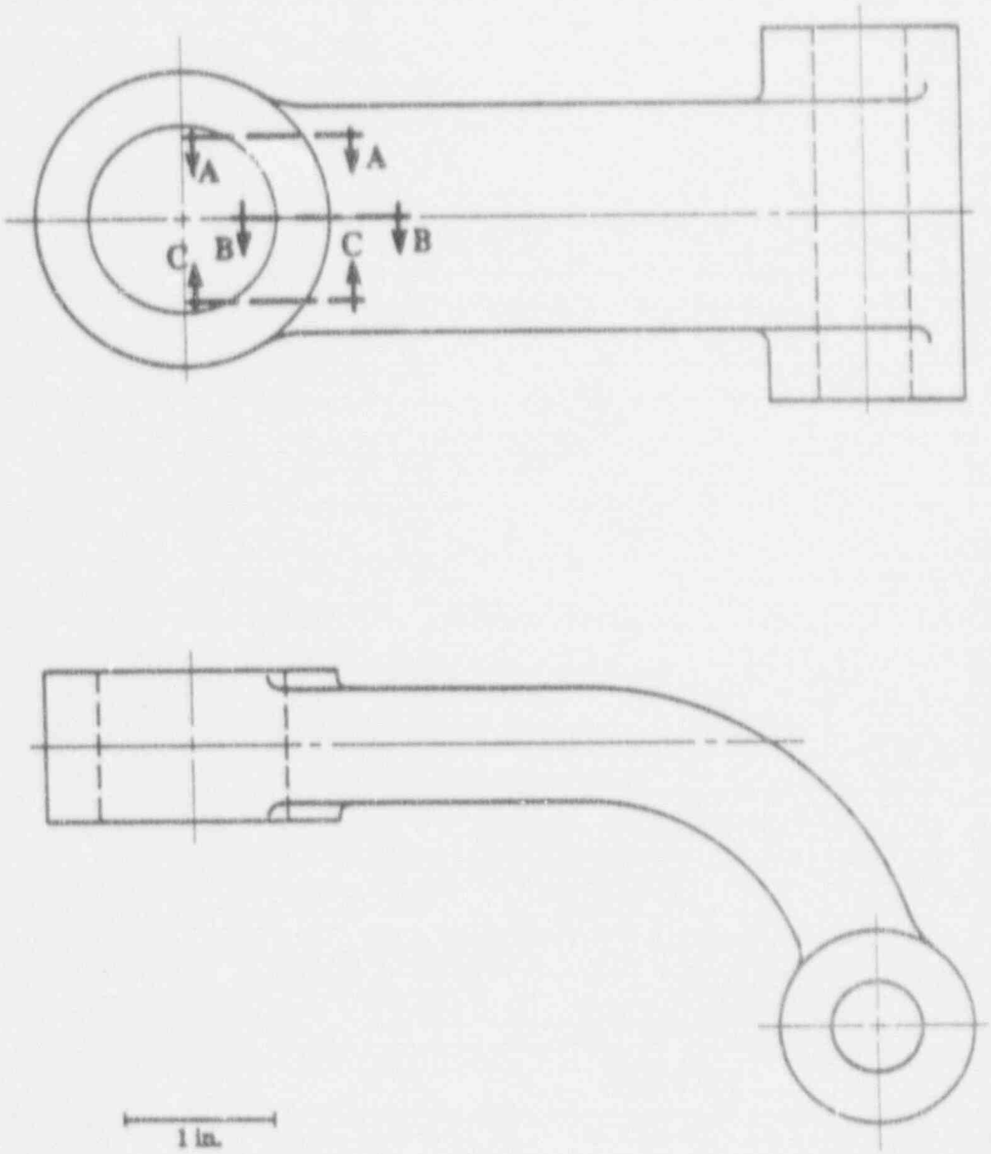

FIGURE 4-1. SCHEMATIC DIAGRAM OF METALLOGRAPHIC SECTION LOCATIONS

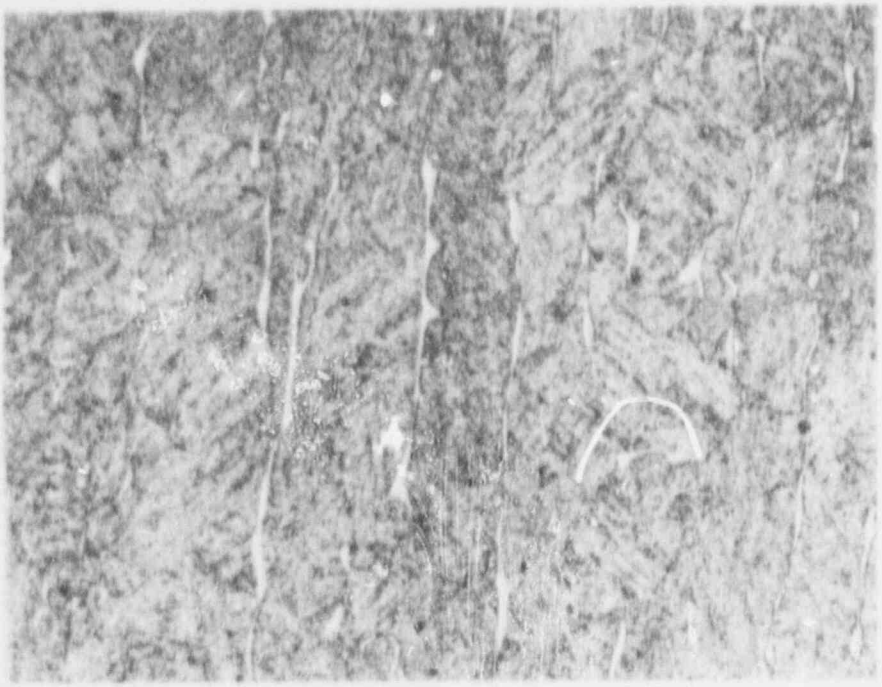

47273 200X

(a) Section A-A, Sample No. 244 (6-in.).

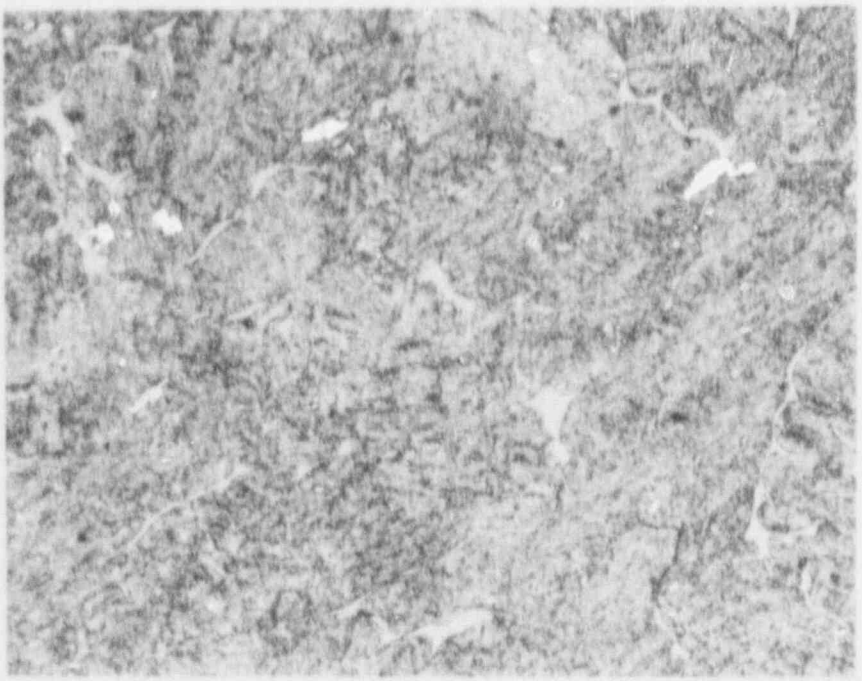

47275 200X

(b) Same section as (a).

FIGURE 4-2. MICROSTRUCTURAL FEATURES OF CAST 17-4PH SWING ARMS. Etchant: Vilella's reagent

47390 200X

(a) Section A-A, Sample No. 259 (4-in.).

47387 200X

(b) Same section as (a).

FIGURE 4-3. MICROSTRUCTURAL FEATURES OF CAST 17-4PH SWING ARMS. Etchant: Vilella's reagent

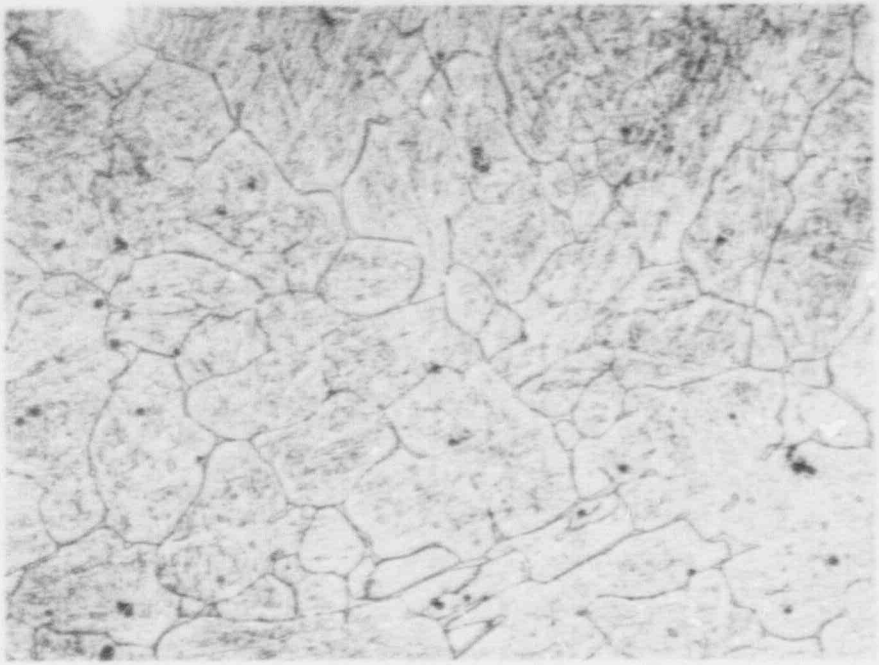

47195 (a) Section A-A, Sample No. 243 (8-in). 200X

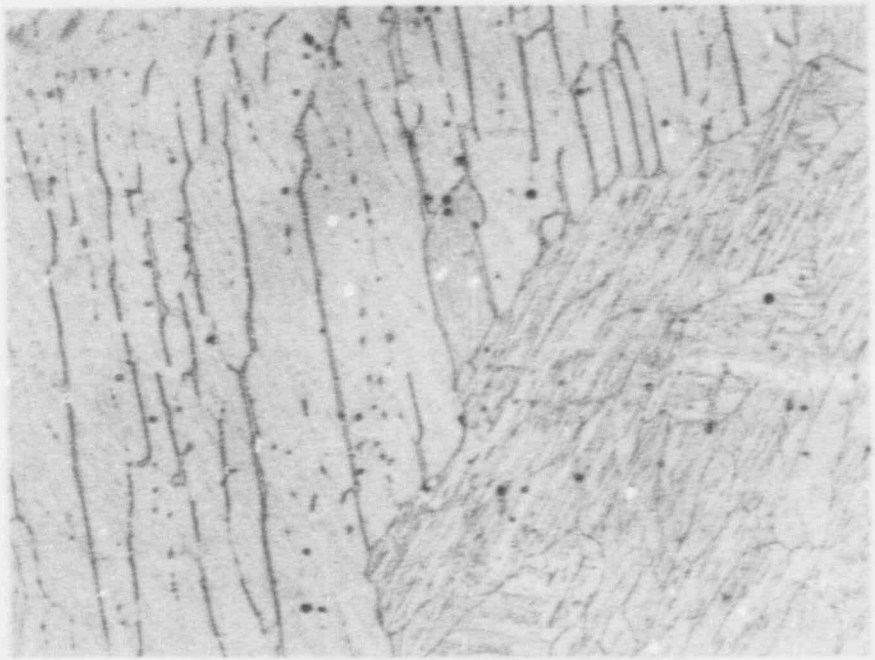

47189 (b) Section B-B, Sample No. 242 (8-in.) 200X

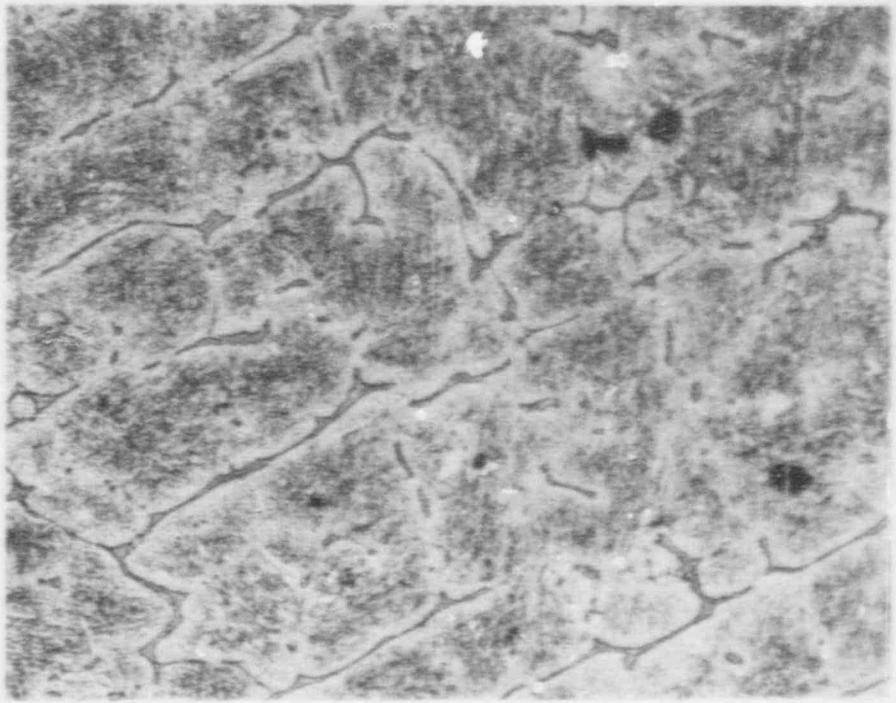

47229 (c) Section C-C, Sample No. 255 (10-in.) 200X

FIGURE 4-4. MICROSTRUCTURAL FEATURES OF CAST 17-4PH SWING ARMS. Etchant: Vilella's reagent

47486 200X

(a) Section A-A, Sample No. 261 (3-in.).

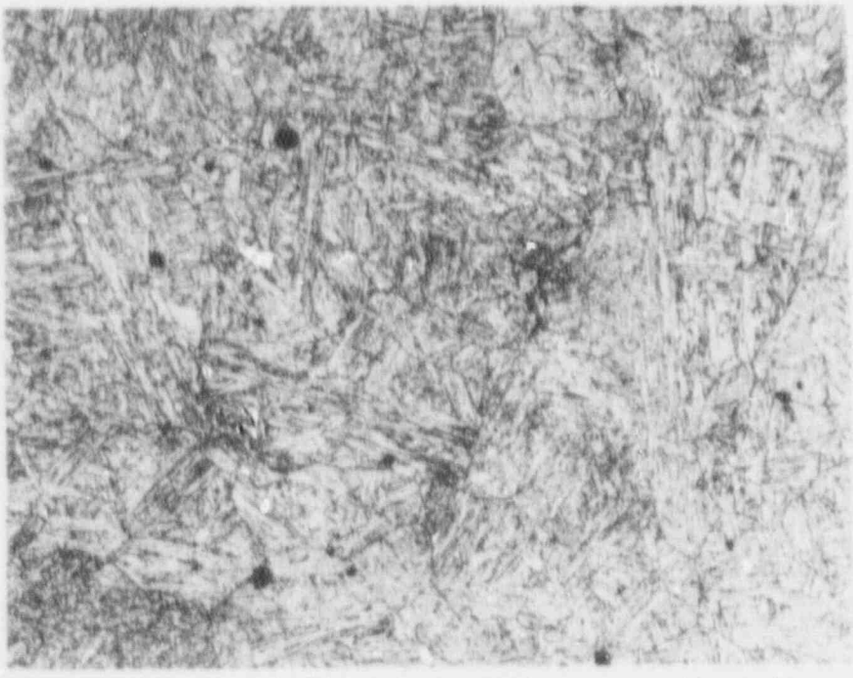

47479 200X

(b) Section C-C, Sample No. 263 (3-in.).

FIGURE 4-5. MICROSTRUCTURAL FEATURES OF CAST 17-4PH SWING ARMS. Etchant: Vilella's reagent

47187 (a) Section B-B, Sample No. 242 (8-in). 200X

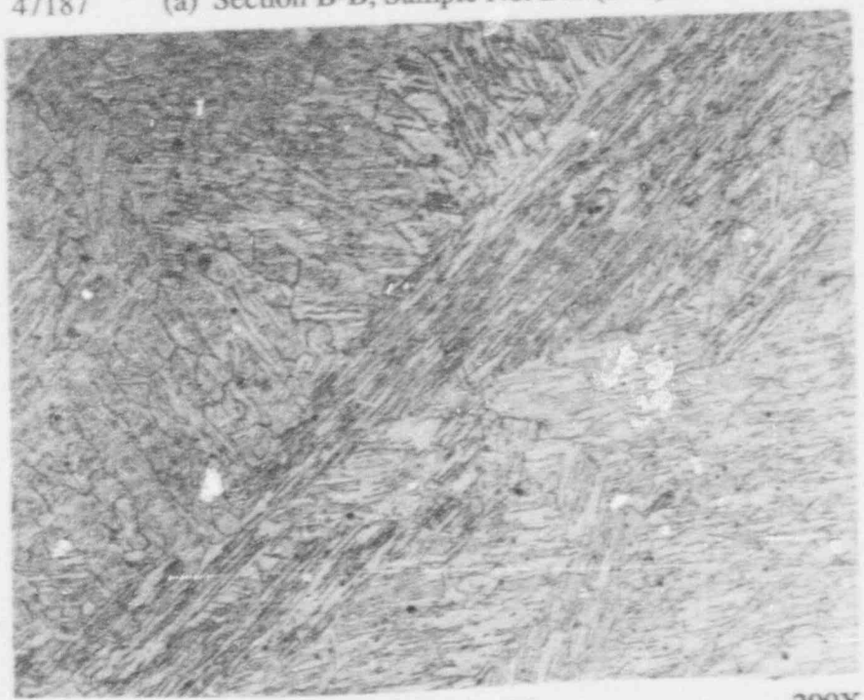

47192 (b) Same section as (a). 200X

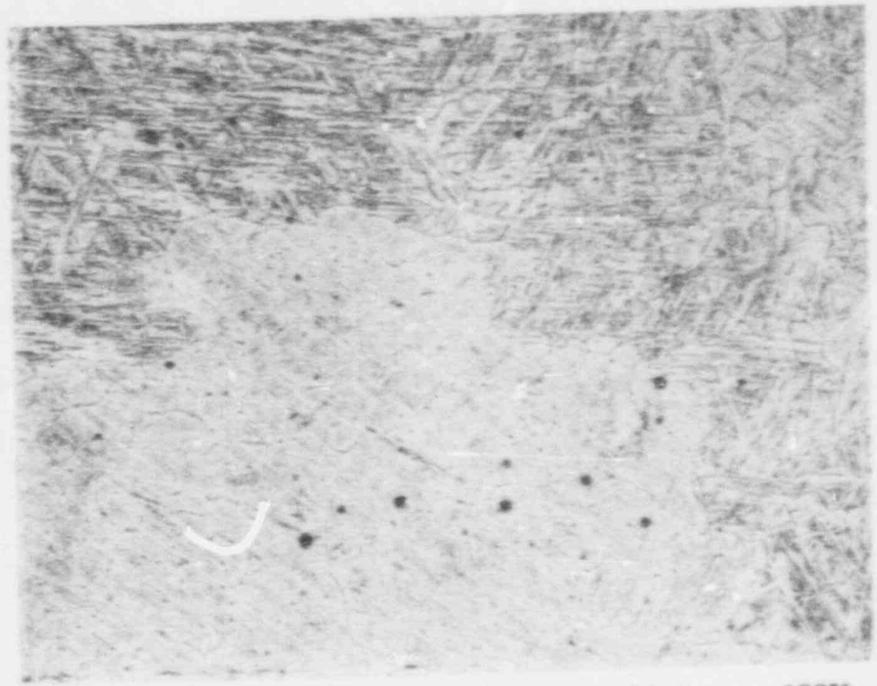

47817 (c) Section A-A, Sample No. 240 (16-in.) 100X

FIGURE 4-6. MICROSTRUCTURAL FEATURES OF CAST 17-4PH SWING ARMS. Etchant: Vilella's reagent

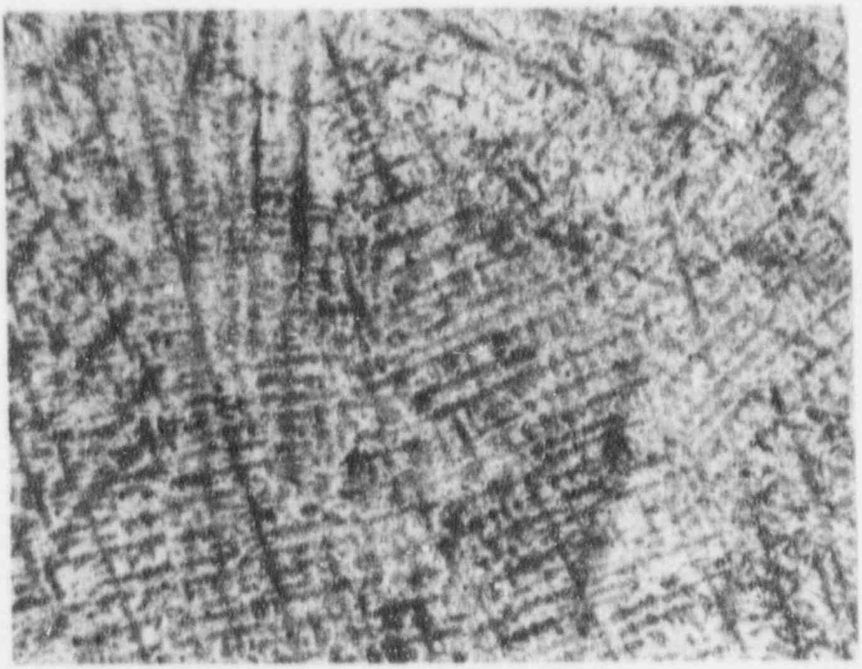

47369 16X

FIGURE 4-7. MICROSTRUCTURE OF SAMPLE NO. 260 (4-in.)
Etchant: Vilella's reagent

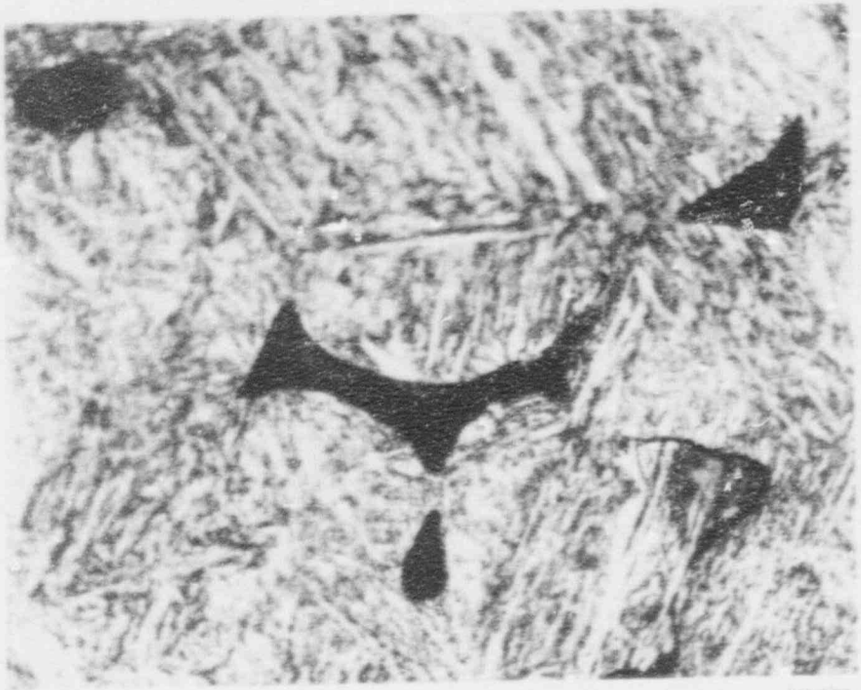

46310 500X

(a) Sample No. 239 (16-in.)

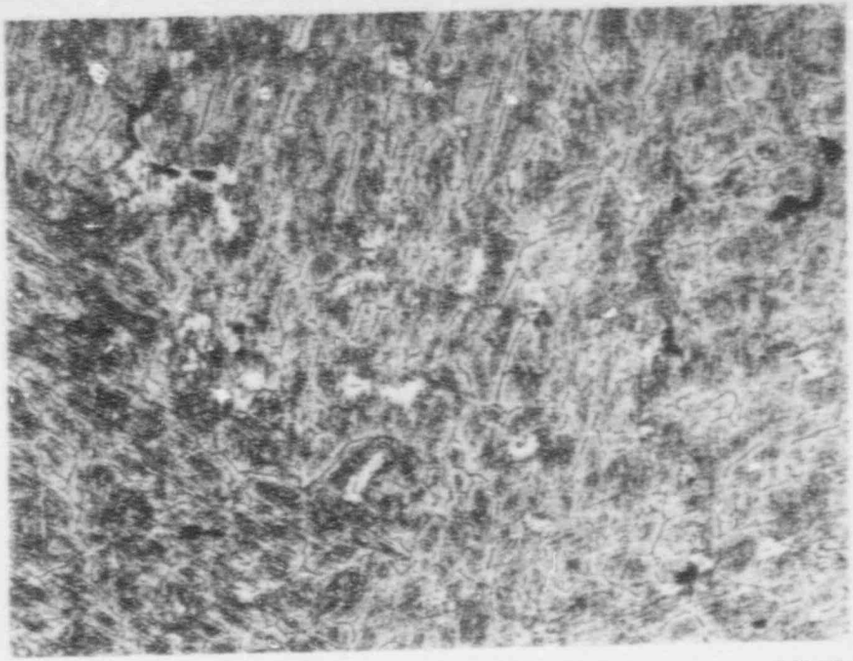

47306 (b) Sample No. 255 (10-in.) 100X

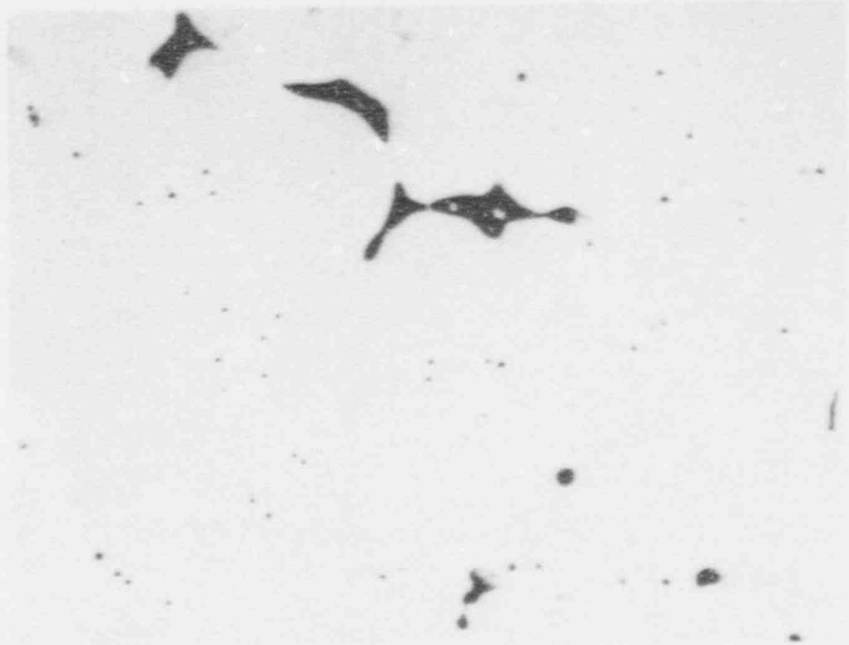

47115 (c) Sample No. 242 (8-in.) 200X
As polished.

FIGURE 4-4. MICROVOIDS IN CAST 17-4PH SWING ARMS. Etchant: Vilella's reagent. Note different magnifications.

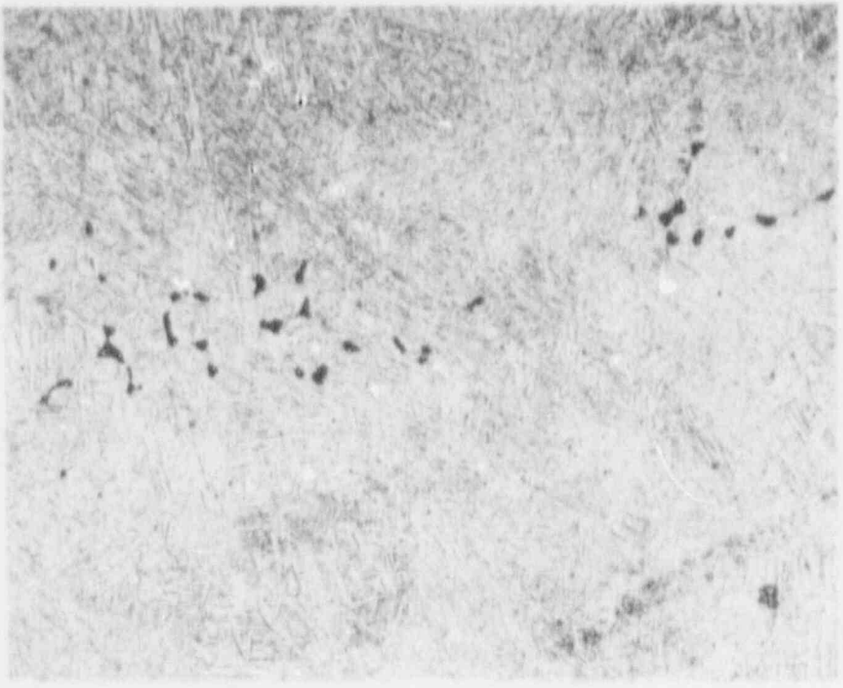

47383 200X

(a) Sample No. 245 (4-in.)

47477 100X

(b) Sample No. 263 (3-in.)

FIGURE 4-9. MICROVOIDS IN CAST 17-4PH SWING ARMS. Etchant: Vilella's reagent. Note different magnification.

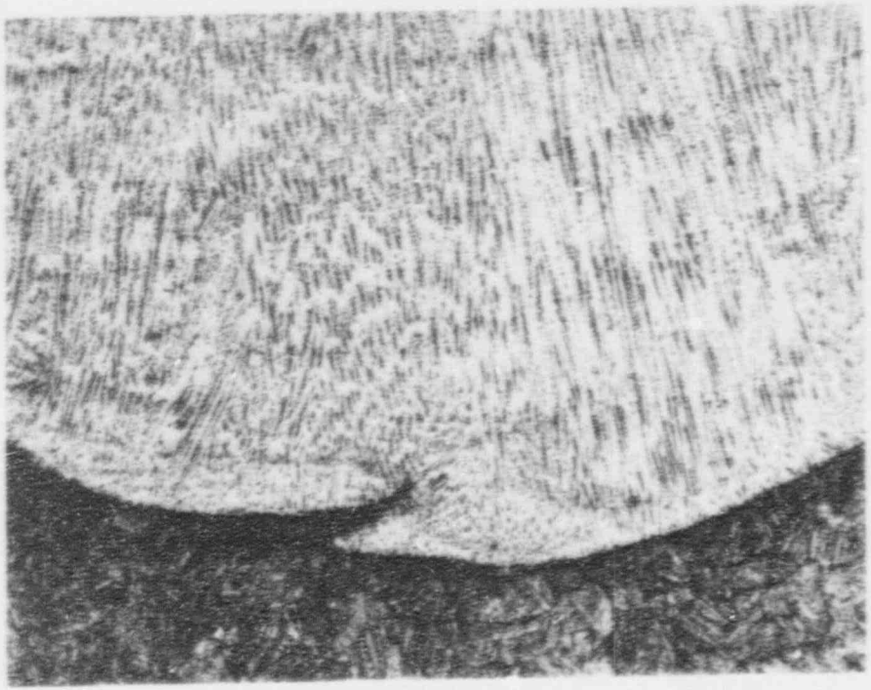

46303 50X

(a) Weld and fusion line.

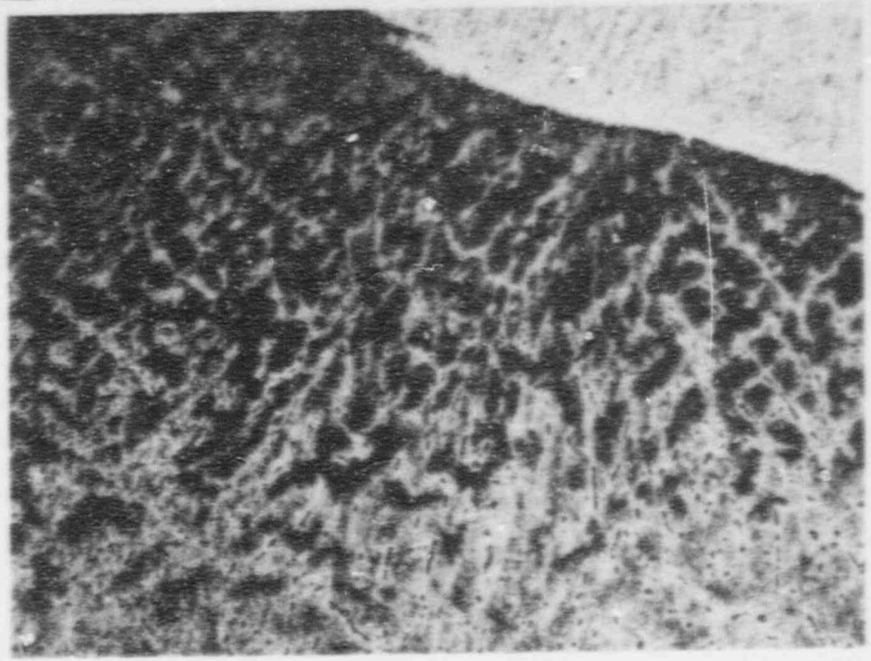

46591 50X

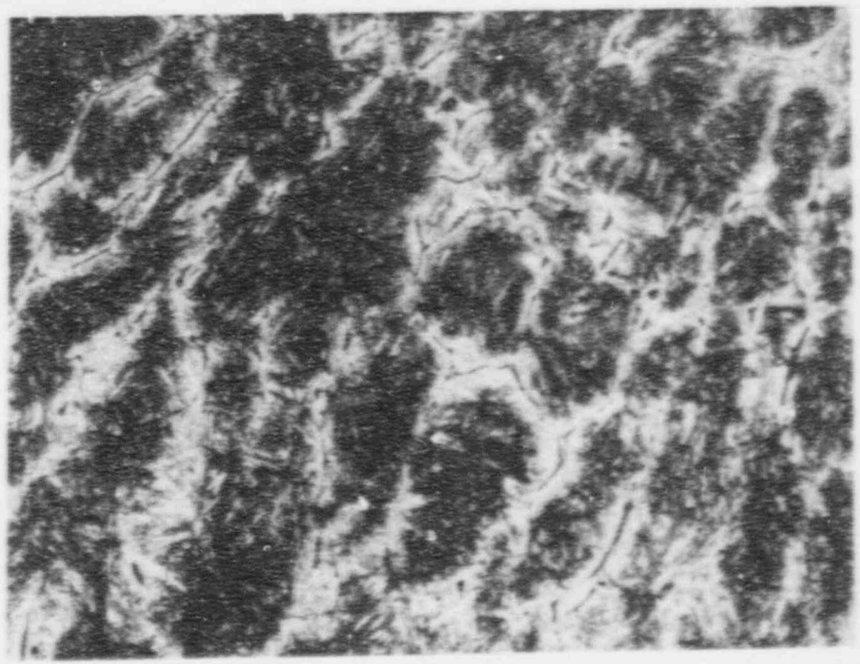

46637 (b) HAZ 200X

FIGURE 4-10. MICROSTRUCTURE OF WELD REPAIR - SAMPLE NO. 239 (16-in.)

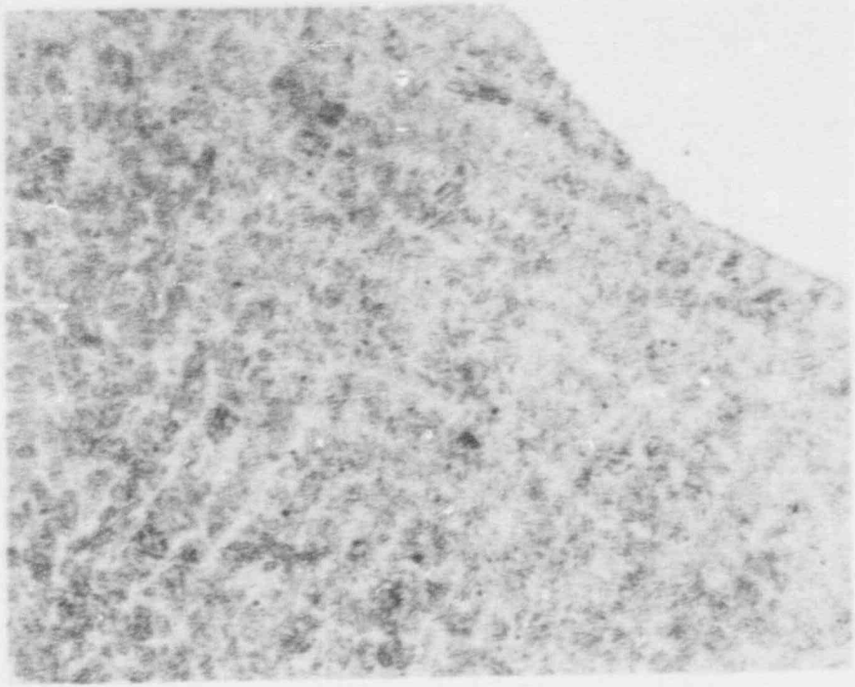

47823 50X

(a)

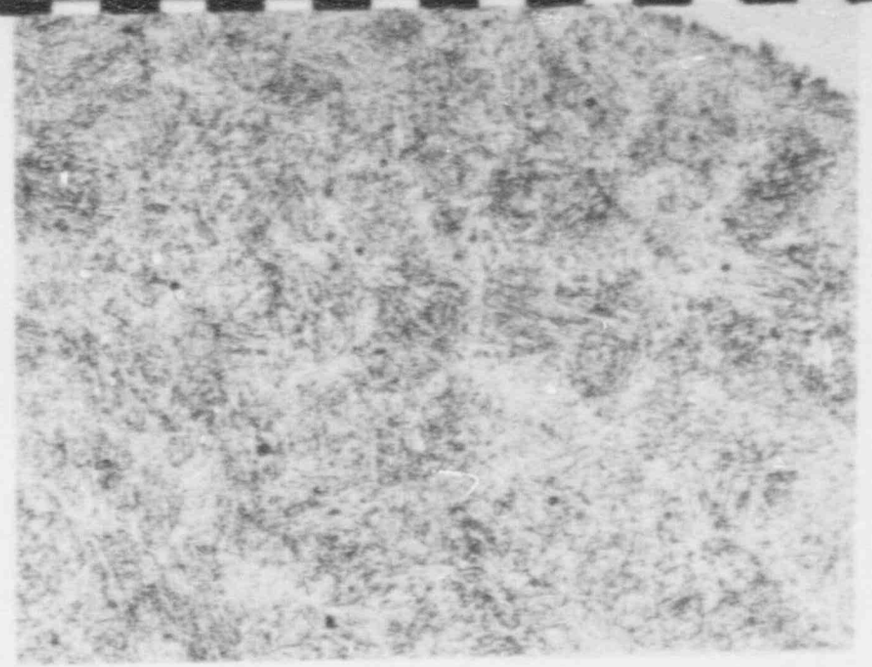

47822 (b) Adjacent to fusion line. 200X

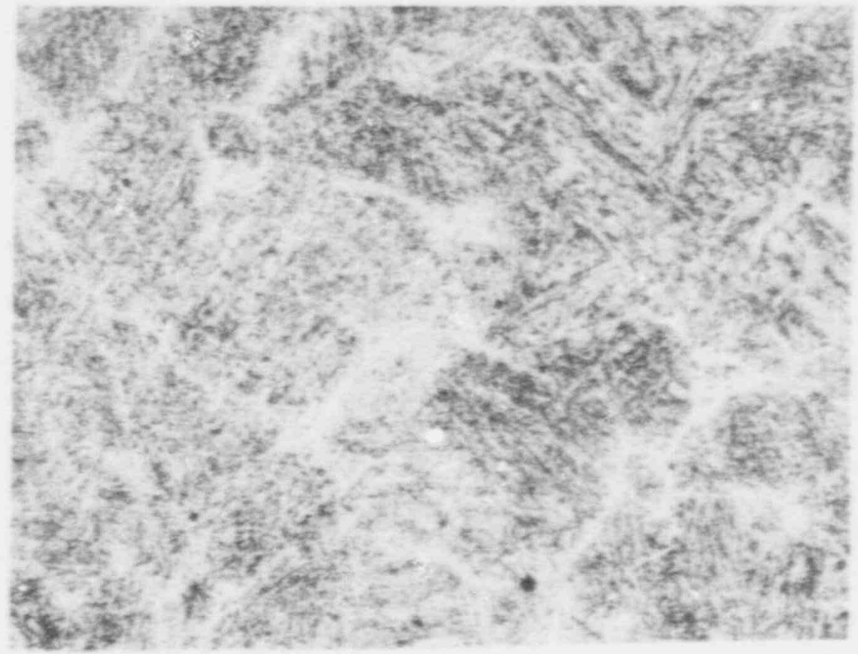

47820 (c) Remote from fusion line. 200X

FIGURE 4-11. HAZ OF WELD REPAIR IN SAMPLE NO. 240 (16-in.). Section through disk attachment boss in plane normal to boss centerline. Etchant: Vilella's reagent

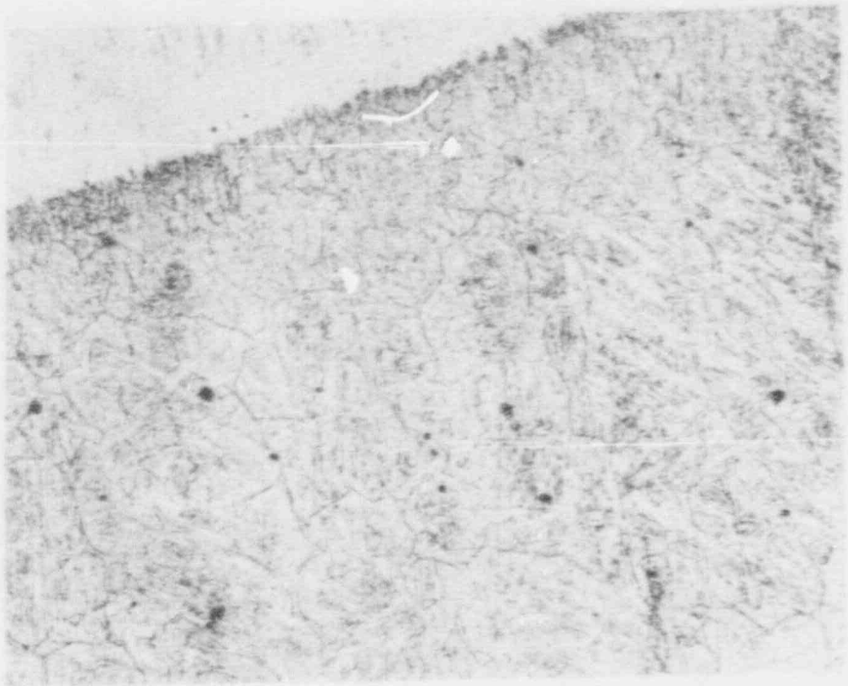

47197 200X

(a) Sample No. 243 (8-in.)

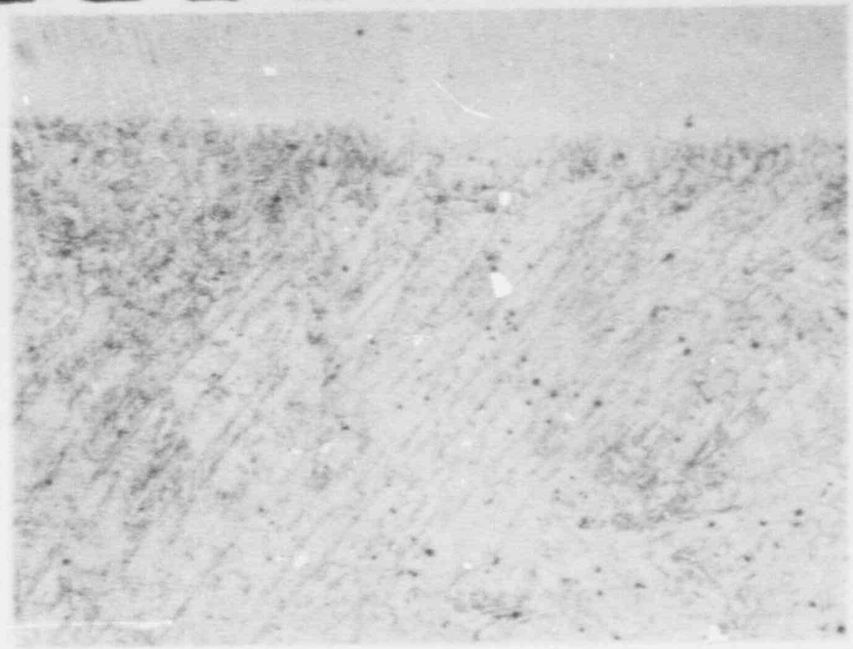

47281 100X

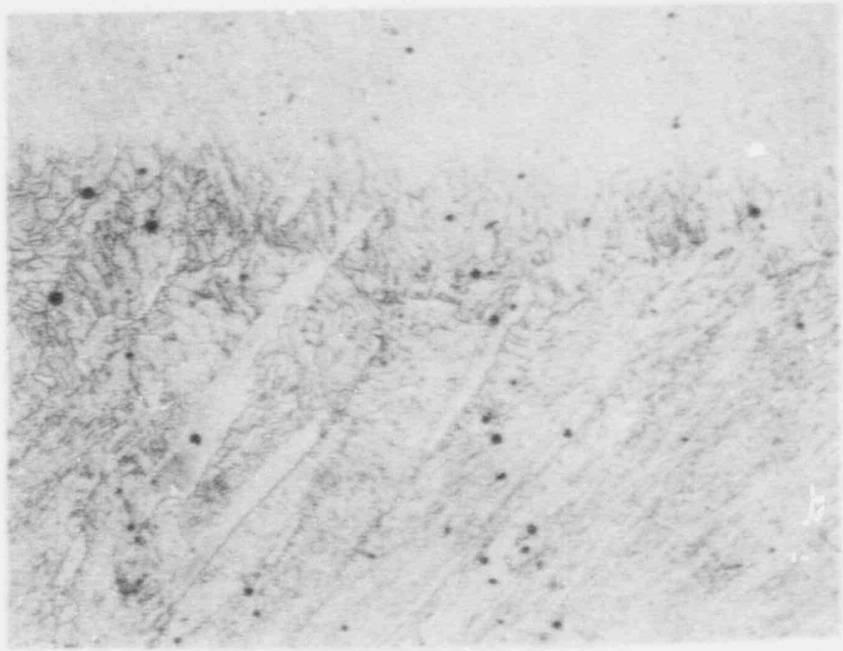

47282 (b) Sample No. 256 (6-in.) 200X

FIGURE 4-12. MICROSTRUCTURES OF WELD REPAIRS IN SAMPLES NO. 243 (8-in.) AND 256 (6-in.).
Etchant: Vilella's reagent

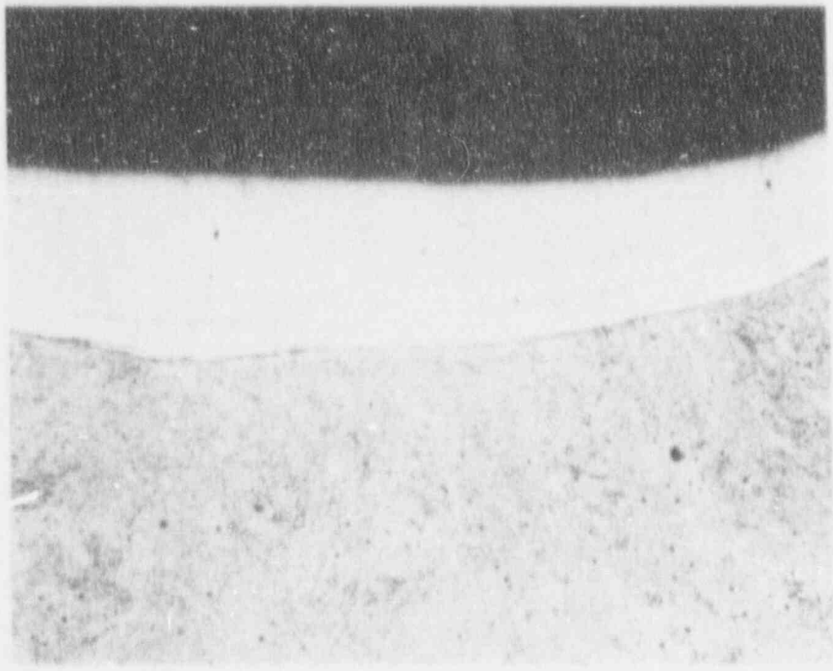

47382 16X

(a)

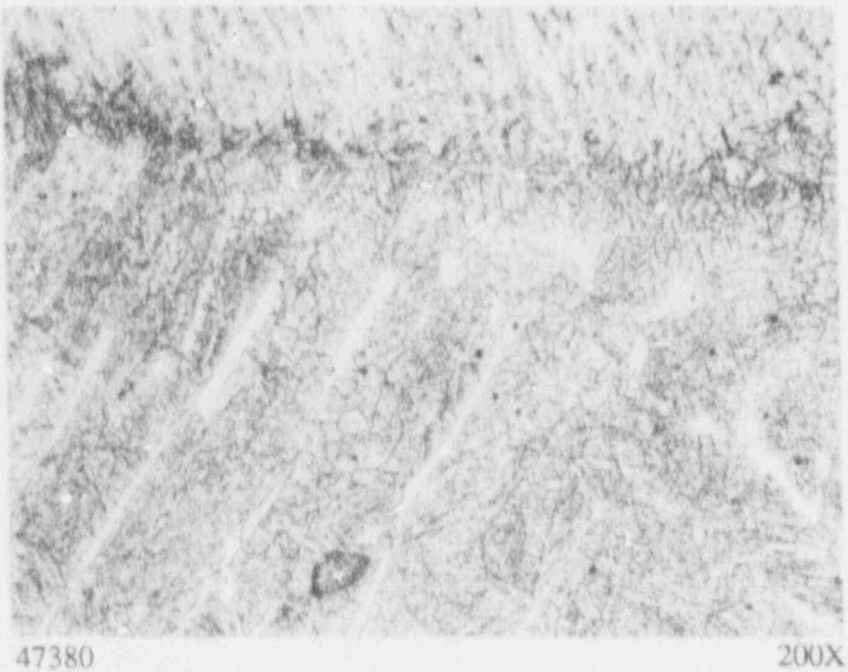

47380 200X

(b)

FIGURE 4-13. MICROSTRUCTURE OF WELD REPAIR - SAMPLE NO. 245 (4-in.). Section B-B.
Etchant: Vilella's reagent

5.0 FLAW CHARACTERIZATION

5.1 Radiographic Flaw Indications

Six of the sample swing arms exhibited radiographic indications which were classified as Level 2 or higher shrinkage and voids, see Section 2.2 and Table 2-2. Three indications rated as Level 2 and Level 3 (Samples No. 240 and No. 242) and the one case with the large, Level 6 indication (Sample No. 255), were selected for metallographic examination. In each case, specimens containing the flaw indication were cut from the swing arms and sequential metallographic sections were prepared and examined to characterize the flaw. The observations made in these multiple section examinations are described in the following subsections.

5.1.1 *Sample No. 240 (16-in.)*

Sample No. 240 exhibited two radiographic flaw indications classified as Level 3 shrinkage. The locations of these two indications are shown in Figure 5-1.

Section A_o-A_o was cut transverse to the long axis of the arm at the approximate position of the flaw near the end of the straight portion. Examination of both sides of this initial cut did not reveal any microstructural flaw. However, a small subsurface shrinkage crack (hot crack) was present after removal of an additional 0.10 inch beyond Section A_o-A_o. A photomicrograph of this feature is shown in Figure 5-2. The crack was segmented in this plane and the cumulative length of the several segments was 0.14 inch. Other than the shrinkage crack, there were no microstructural abnormalities at this location.

The character of the flaw changed dramatically after removal of an additional 0.006 inch. In this new section, the flaw appeared as a very tight, segmented, intergranular microcrack with a cumulative length of 0.07 inch, see Figure 5-3. The feature was not detectable at magnifications below 200X. Apparently, this metallographic section intersected the extreme outer fringes of the flaw. Further grinding in increments of approximately 0.05 inch did not reveal any other microstructural flaws. Based on the measurement of the material removed between each section, the maximum dimension of this flaw in a direction parallel to the long axis of the swing

arm is 0.16-inch. The features observed in the sequential sections show that, as the worst case, this flaw may be considered as a small, internal, planar crack located near the center of the cross section of the arm. A diagram of the orientation and maximum size of the flaw is shown in Figure 5-4.

The second radiographic indication in Sample No. 240 was located within the curved portion of the arm near the hinge boss, see Figure 5-1. Section B_o-B_o was cut to intersect the flaw indication. A cluster of voids was clearly evident on each side of this initial cut and sequential sections were examined in both directions from Section B_o-B_o. Photomacrographs from these sections are shown in Figures 5-5 and 5-6. In each of the three sections closest to the center of the indication, the void cluster consisted of one or more relatively large voids (largest dimension on the order of 0.05-inch) with several much smaller voids in the immediate vicinity [see Figures 5-5(b) and (c) and 5-6(a)]. Of the two outer sections, one exhibited a cluster of very small voids [Figure 5-6(b)] and the other contained a small fissure [Figure 5-5(a)]. These features indicate that the outermost sections were located at or near the extremities of the flaw and serve to establish the maximum dimension of the flawed zone. A diagram showing the extent of the flawed zone is shown in Figure 5-7. Since the metallographic sections identified the flaw as a cluster of voids rather than a single large void or a discrete crack-type feature, the flaw zone in Figure 5-7 is dimensioned to represent a volume which completely contains the void cluster. Note that the outlined areas in Figure 5-7 represent the projections of the volume on the top and side of the arm. The cross sections shown in Figures 5-5 and 5-6 must be considered to view the actual shape of the flawed zone. In this case, the flaw may be considered as a thin, irregular volume lying on a warped surface and containing a concentration of small voids. Considering the volume as a single, open void, the maximum cross-sectional void area would be only 0.01-in.^{2} or less.

5.1.2 *Sample No. 255 (10-in.)*

The radiographic inspection of Sample No. 255 revealed Level 6 voids or inclusions within the straight portion of the arm approximately 3 inches from the centerline of the valve disk boss. Multiple longitudinal and transverse sections were taken through the zone of radiographic indications to size the flaws.

The longitudinal sections revealed a large, elongated void oriented essentially normal to the long axis of the arm. Photomacrographs from selected longitudinal sections are shown in Figure 5-8. In these sections, the void is roughly circular in cross section with a maximum dimension on the order of 0.16-inch. Near the centerline of the arm, the character of the flaw changed from a single large void to clusters of very small voids as shown in Figure 5-9. Further grinding eliminated the flaw.

Transverse sections in the flaw zone revealed a second, large, irregularly shaped void on the opposite side of the arm. Photomacrographs showing the cross section of that void in transverse sections are shown in Figure 5-10.

A diagram of the flawed zone showing the locations of the metallographic sections and the extent and shape of the voids derived from the sequential sections is shown in Figure 5-11. The overall shape and locations of the two voids show that certain transverse sections would intersect both voids. Thus, this flaw may be considered as an internal, rounded shrinkage cavity with a maximum cross-sectional area of 0.23 in^2.

5.1.3 *Sample No. 242 (8-in.)*

Sample No. 242, one of the two 8-in. swing arms, exhibited a single, Level 2 radiographic indication similar to those recorded for Samples 239 and 240. This indication was located in the straight portion of the arm approximately 2 inches from the centerline of the valve disk boss. Multiple transverse sections through the zone of the indications were examined and representative photomacrographs are shown in Figures 5-12 through 5-15. In each cross section, the flaw appeared as a cluster of small voids with the most severe condition shown in Figure 5-15. It should be noted that in Figures 5-14 and 5-15 some of the voids are aligned in the vertical direction, an orientation that would contribute to a strong radiographic indication in a through-thickness radiograph.

The location, extent and orientation of the flawed zone in Sample No. 242 are illustrated in Figure 5-16. The dimensioned zone in that diagram represents the volume containing the void clusters in the same manner as for Sample No. 240 in Figure 5-7. If the flaw

zone is considered to be a single void with dimensions as shown in Figure 5-16 and cross sections compatible with the void clusters seen in transverse sections, maximum cross sectional area would be determined by the section shown in Figure 5-15. That area was determined to be 0.02 in^2.

5.2 Other Flaws

Other small flaws were encountered in the course of the routine metallographic examinations. These were observed in the longitudinal sections taken through the boss-to-arm transition at the valve disk end of certain swing arms (see Figure 4-1) and had not been detected in the nondestructive inspections.

A distinct, surface connected shrinkage crack (hot crack) was present at the valve disk boss of Sample No. 255 (10-in.), see Figure 5-17. The crack was located in the radius at the boss and was oriented transverse to the long axis of the arm. In this case, a light etching zone was present around the crack indicating a localized variation in composition. The light etching zone extended beyond the crack tip along an intergranular path. Sequential sectioning established that the crack extended almost half-way across the arm with a maximum length on the top surface of 0.93-inch. The maximum depth measured in the several sections was 0.07-inch [Figure 5-17(a)].

As a worst case, this flaw may be considered as a tight, surface connected crack oriented normal to the axis of the swing arm. This case is diagramed in Figure 5-18. The dimensions of the flaw are such that it may be conservatively represented as a semi-elliptical crack, 0.93-inch long and 0.09-inch deep.

A small, internal fissure was present near the top surface of the boss in one of the 4-inch swing arms, see Figure 5-19(a). This microfissure was less than 0.02-in. across in that section and sequential grinding established that its maximum length in a direction transverse to the long axis of the arm was 0.10-inch. This flaw was considerably smaller than the fissure-type flaws observed in other samples.

Figure 5-19(b) shows a small, unique flaw which was found in one of the 3-in. swing arms. In this case, the flaw consisted of a highly irregular fissure which formed a nearly closed

path. It was located at an outer corner of the valve disk boss and the maximum dimension across the path was 0.025 inch. Considering the small size of this feature and its non-critical location, no further metallographic sectioning was performed.

As noted in Section 2.1, relatively deep surface pits were noted in certain of the swing arm samples during the visual and LP inspections. In the course of the routine metallographic examinations, certain of the longitudinal sections were located to pass through such pits so that the depths and profiles could be established.

A photomacrograph of a typical group of surface pits is shown in Figure 5-20 together with a photomicrograph from the section through the pits. In this particular case, the maximum depth was only 0.01-inch and the pit profile was relatively blunt. Also, there was no evidence of cracking from the pits. These features were generally representative of those in other sections of other arms. In view of the small size and blunt character, these flaws are not considered to be detrimental.

5.3 Flaw Summary

The flaws identified by the metallographic examinations were of two distinct types, namely; 1) small fissures or cracks, and 2) shrinkage cavities or clusters of small shrinkage voids. The significance of the two fissure-type flaws [Samples No. 240 (16-inch) and 255 (10-inch)] may be directly evaluated by linear elastic fracture mechanics (LEFM) since they both represent sharp cracks of known dimensions. In this regard, a surface-connected crack represents a more severe condition than an internal crack of equivalent dimensions.* As a result, evaluation of both fissure-type flaws as surface-connected cracks is a conservative approach.

LEFM techniques are not directly applicable to the open, rounded features of the cavity in Sample No. 255 or the void clusters in Samples No. 240 and 242. However, as an initial, conservative approach, LEFM may be applied to these flaws by considering each flaw as a tight,

---

* The stress intensity factor for a surface-connected semi-elliptical crack exceeds that of an internal elliptical crack of the same dimensions by a factor of 1.12.

elliptical crack of a size equivalent to the length and breadth of the void or void cluster. An additional degree of conservatism is introduced by treating the flaw as a semi-elliptical surface-connected crack.

Following these concepts, calculations were made to determine the stress intensity factor (K_I) associated with each of the flaws described in Figures 5-4, 5-7, 5-11 and 5-16. Each flaw was treated as a semi-elliptical, surface-connected crack oriented transverse to the swing arm and the calculations were made for the case of a pure bending load with the flaw on the tension side. The expression used for the determination of the stress intensity factor for such a case is.

$$K_I = H\sigma_B\sqrt{\pi\frac{a}{Q}}F\left(\frac{a}{t},\frac{a}{c},\frac{c}{b}\right)$$

where:

σ_B = bending stress
t = section thickness
b = section width
a = crack depth
2c = crack length
Q = crack geometry factor
and F and H = boundary correction functions

The basis for development of this expression is described by Newman and Raju [1] and the individual equations for Q, and the functions F and H are presented in Appendix C.

This expression takes the geometry of the swing arm into consideration as well as the crack geometry. The results of these calculations, using a value of $\sigma = 60$ ksi for the maximum bending stress, are presented in Table 5-1.* The stress intensity factors determined by these calculations ranged from 18.6 to 31.1 ksi$\sqrt{in}$.

The fracture mechanics evaluation of the flaws in the swing arms is presented graphically in Figures 5-21 and 5-22. Figure 5-21 illustrates the critical stress for fracture (σ_c) for

---

* The value of 60 ksi for the tensile stress at the outer fiber due to bending was selected as representative of the surface impact stresses based on earlier investigations at CPSES.

each crack geometry as a function of crack size. Figure 5-22 demonstrates the interdependency of the critical stress (σ_c), crack size (a) and fracture toughness (K_{IC}) for a common flaw shape in Table 5-1.

TABLE 5-1

FRACTURE MECHANICS PARAMETERS FOR LARGEST OBSERVED FLAWS

Valve Size	Sample No.	W in.	t in.	2c in.	a in.	Figure No.	a/t	a/2c	K_I† ksi$\sqrt{in.}$
16-in.	240	2.15	1.30	0.16	0.07*	5-4	0.05	0.44	18.6
				0.70	0.10**	5-7	0.08	0.14	31.1
10-in.	255	1.78	1.00	0.93	0.09*	5-18	0.09	0.10	30.5
				0.94	0.08‡	5-11	0.08	0.08	29.5
8-in.	242	1.50	1.00	0.67	0.12**	5-16	0.12	0.18	30.9

† For bending stress σ_B = 60 ksi selected as representative of expected surface impact stress.
* Actual crack.
** Crack equivalent to void cluster.
‡ Crack equivalent to open cavity.

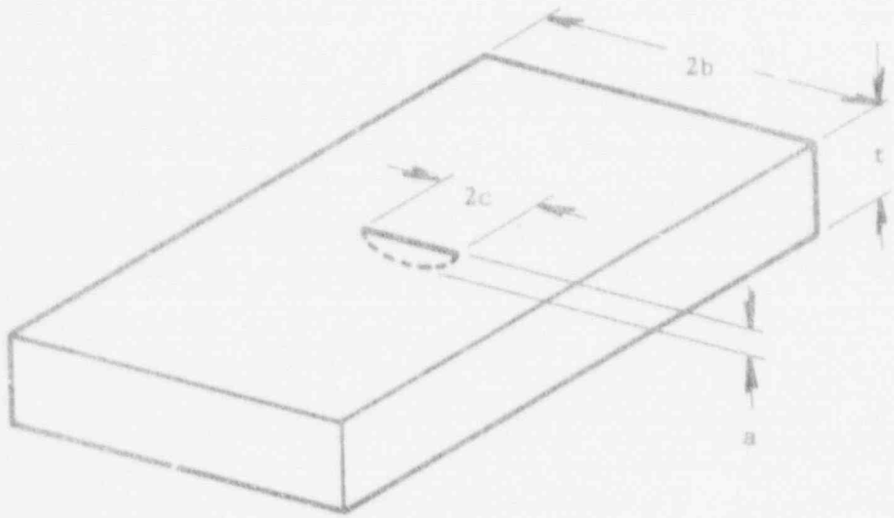

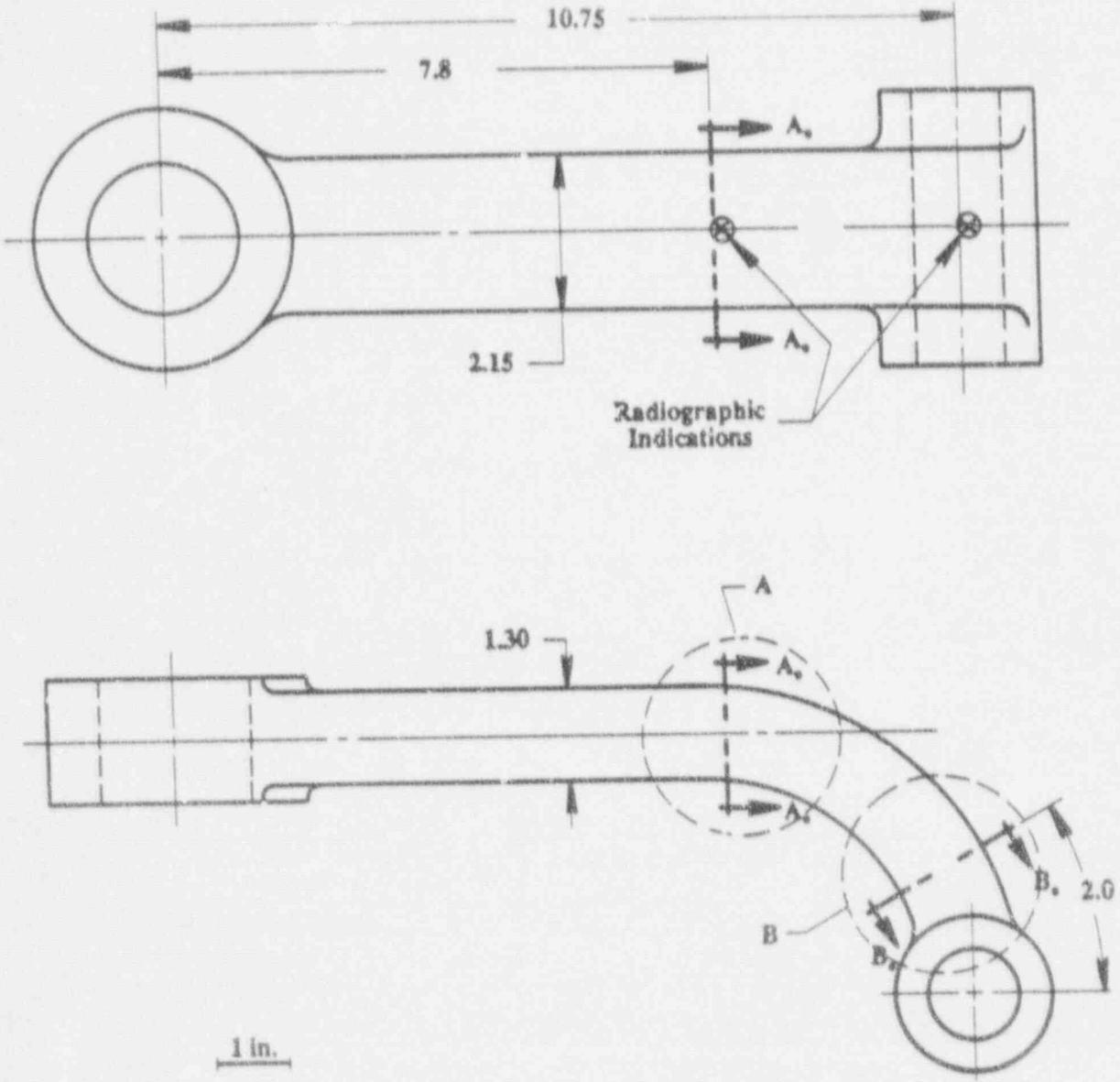

FIGURE 5-1. LOCATIONS OF RADIOGRAPHIC INDICATIONS IN SAMPLE NO. 2 10 (16-in.). Scale is approximate.

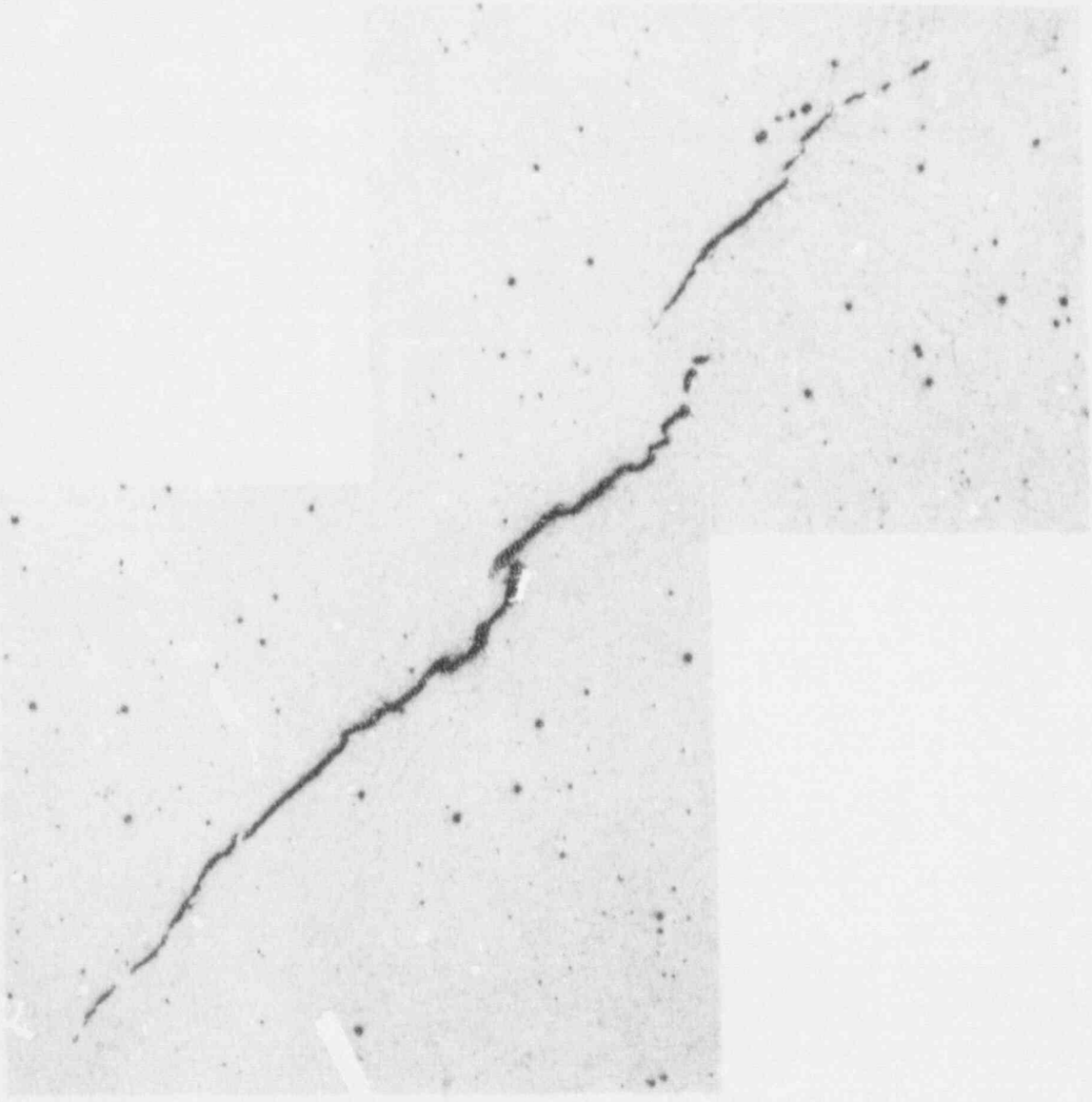

46520-521 50X

FIGURE 5-2. INTERNAL FISSURE IN SAMPLE NO. 240. Transverse section of arm at location of radiographic flaw indication. Section A_o-A_o + 0.10-in., see Figure 5-1. Etchant: Vilella's reagent

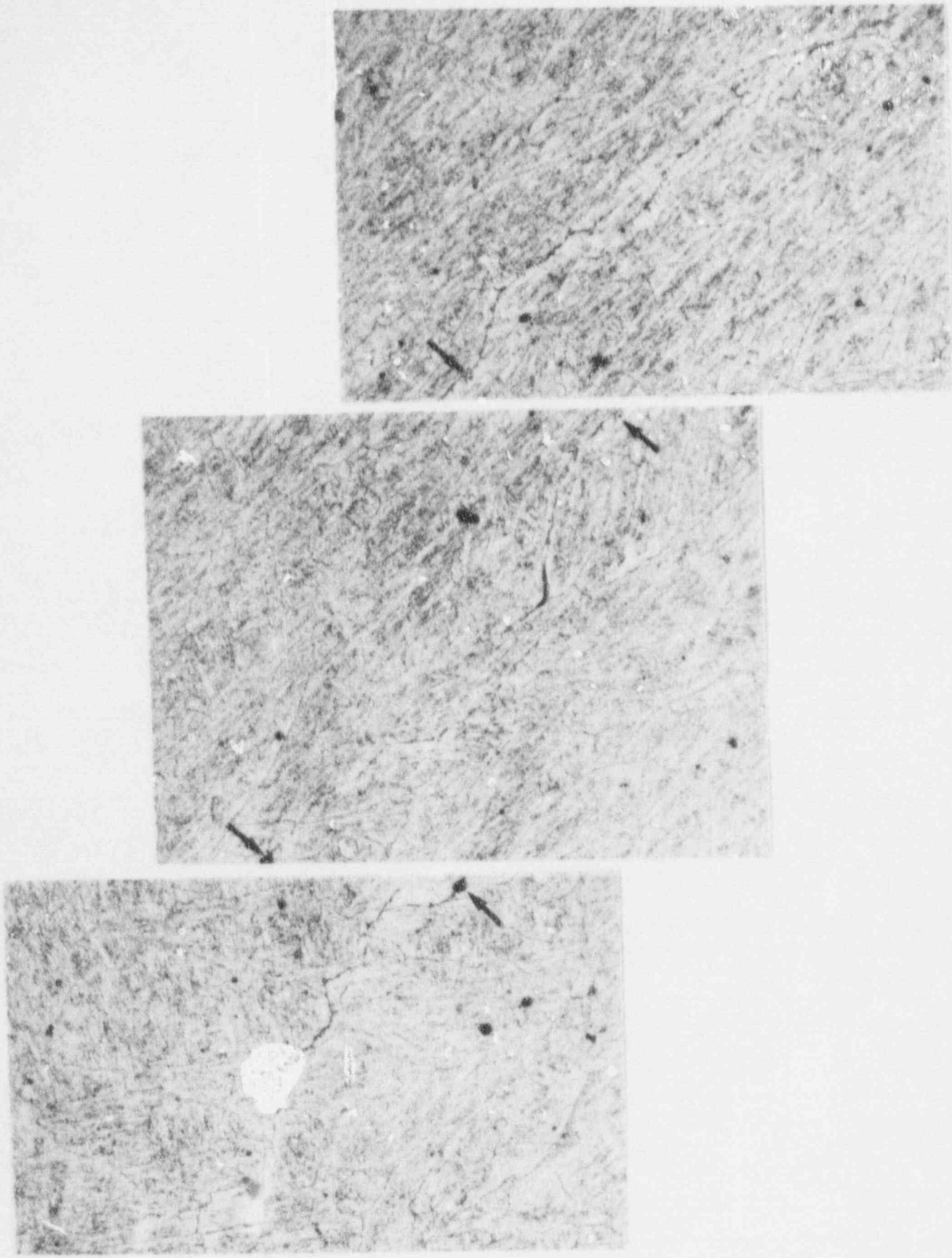

46662-64 200X

FIGURE 5-3. MICROFISSURE IN SAMPLE NO. 240 (16-in.). Transverse section 0.006 inch beyond section of Figure 5-2. Three matching photomicrographs. The upper two are displaced to the left to fit the single page format. Arrows mark matchpoints in each photomicrograph. Etchant: Vilella's reagent

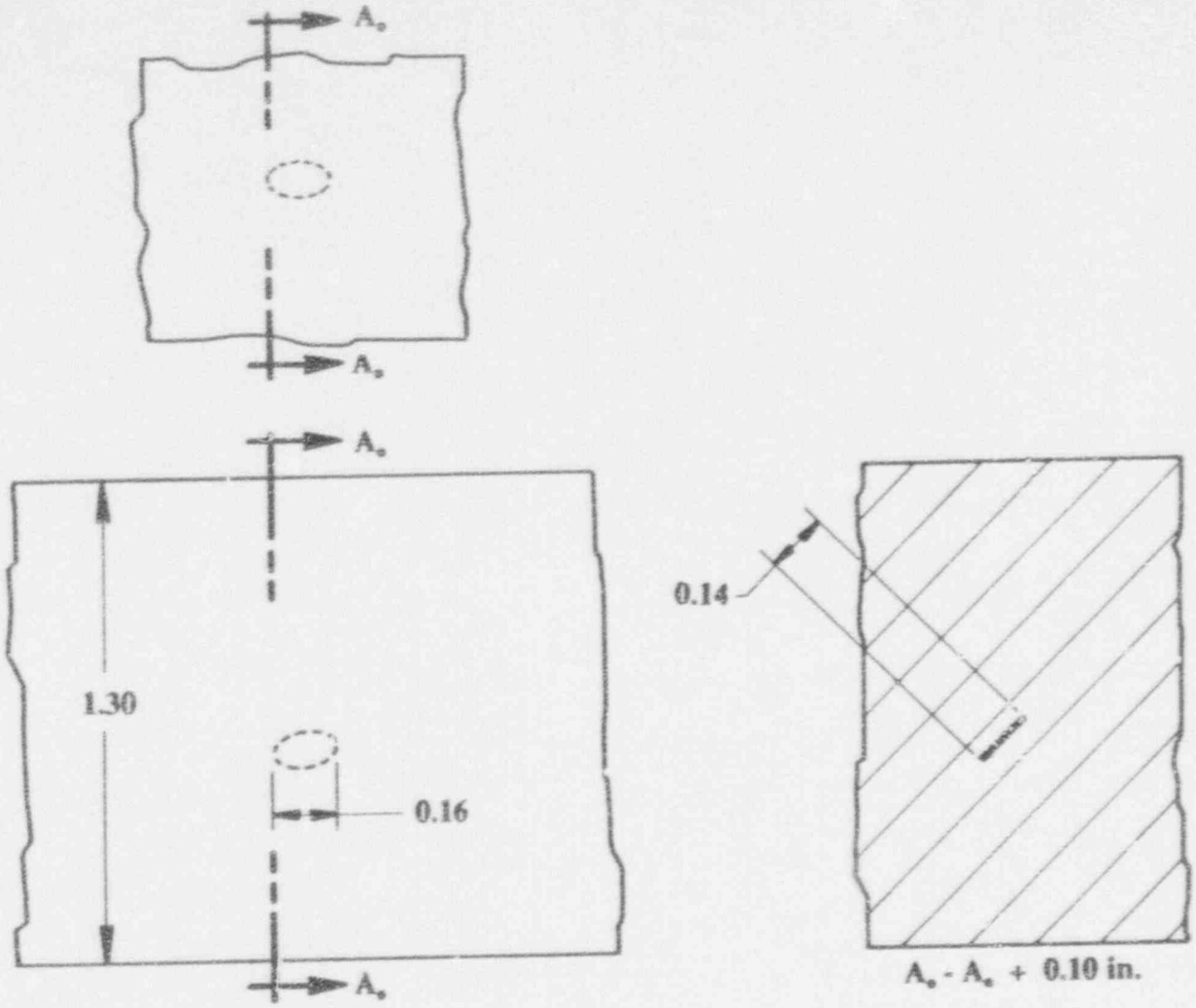

View A in Figure 5-1

FIGURE 5-4. **DIAGRAM OF INTERNAL FISSURE IN SAMPLE NO. 240 (16-in.).** See Figure 5-1 for location. Twice size. Dimensions in inches.

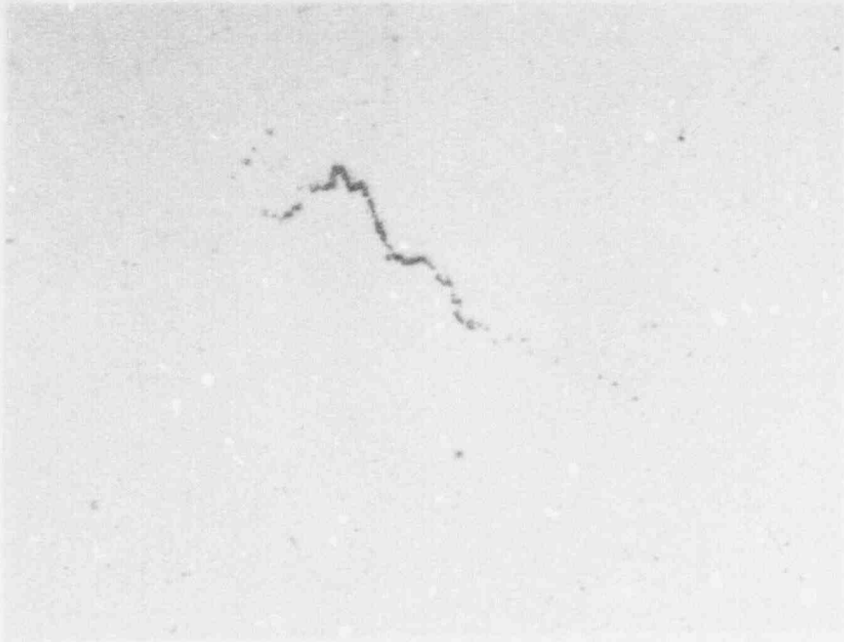

47963 (a) Section B_o-B_o - 0.34-in. As polished. 16X

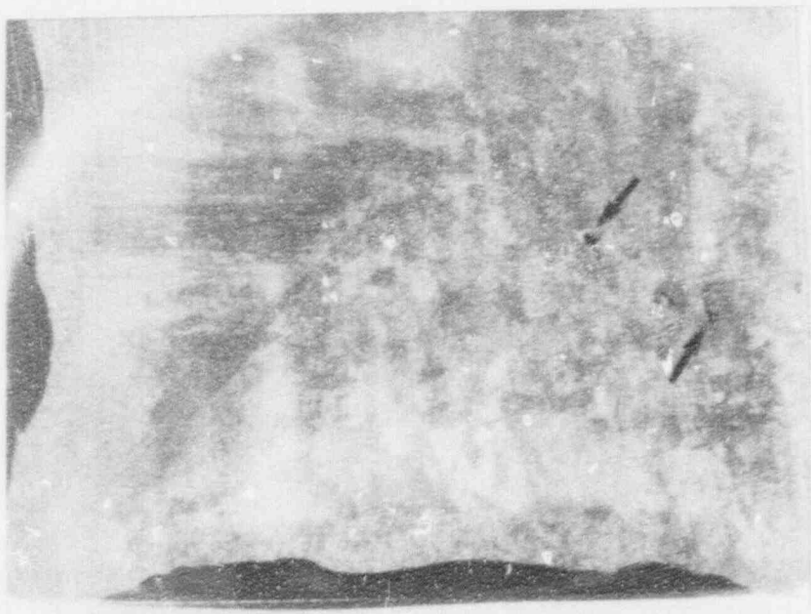

47959 (b) Section B_o-B_o - 0.06-in. Etched 4X

47960 4X

(c) Section B_o-B_o. Etched

FIGURE 5-5. TRANSVERSE SECTIONS FROM SAMPLE NO. 240. See Figure 5-1 for locations. Arrows mark larger voids in (b) and (c).

47961 4X

(a) Section B_o-B_o + 0.30-in. Etched. Arrows mark larger voids.

47962 16X

(b) Section B_o-B_o + 0.36-in. As polished.

FIGURE 5-6. TRANSVERSE SECTIONS FROM SAMPLE NO. 240.
See Figures 5-1 and 5-7 for locations.

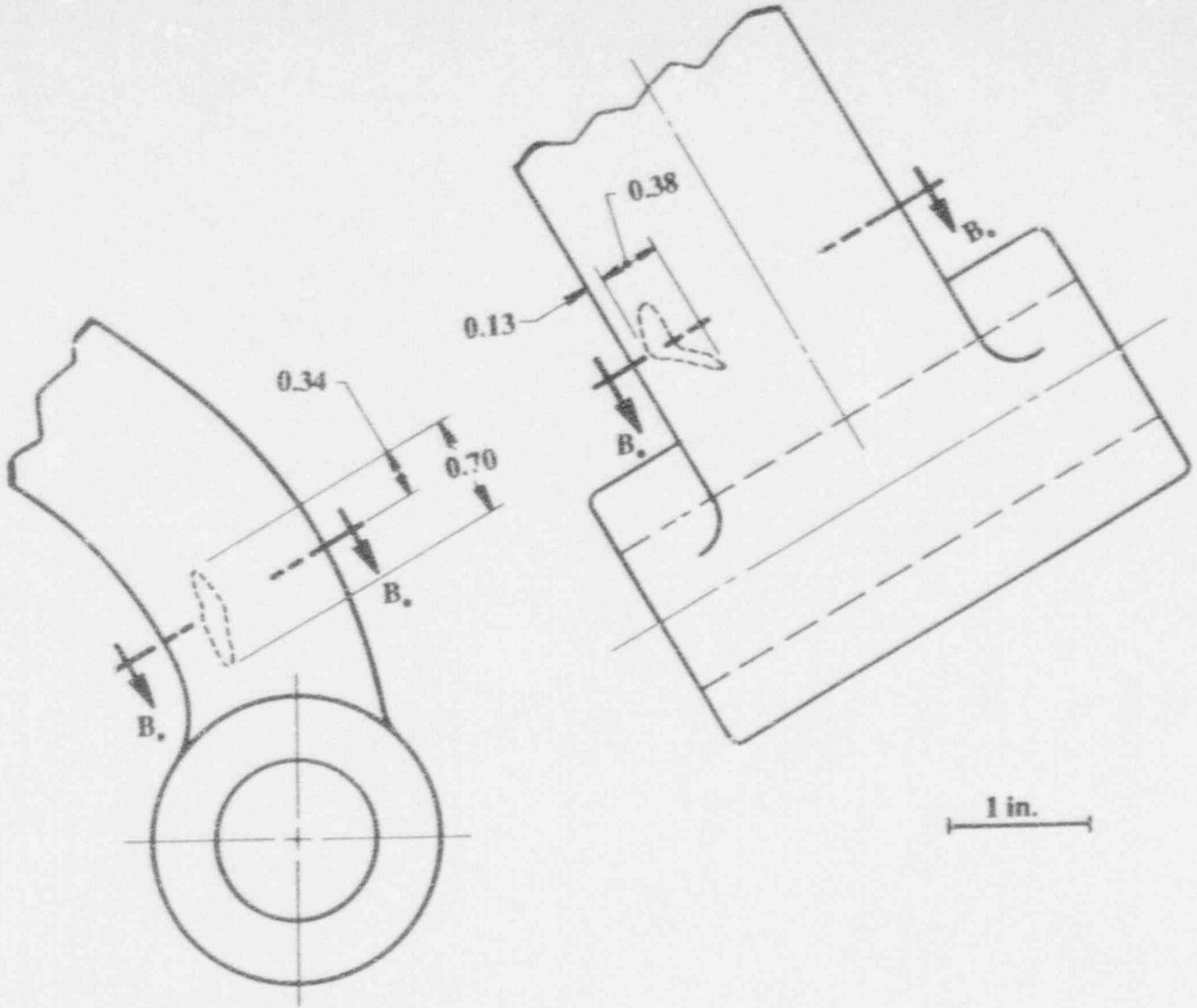

View B in Figure 5-1

FIGURE 5-7. **DIAGRAM OF INTERNAL FLAW IN SAMPLE NO. 240 (16-in.).** Outlined areas represent volume containing concentration of small voids. See Figures 5-5 and 5-6. Scale is approximate.

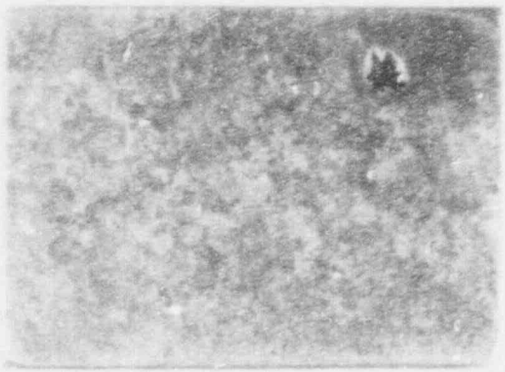

47790 (a) Section A_1-A_1. 2X

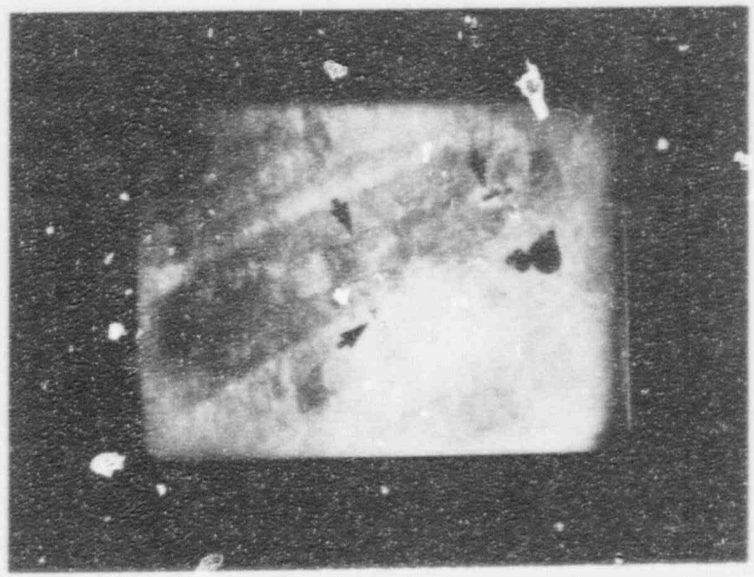

47830 2X

(c) Section A_1-A_1 + 0.68-in. Note small voids at arrows.

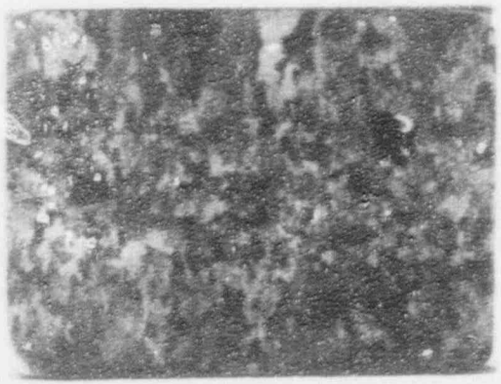

47792 (b) Section A_1-A_1 + 0.46 in. 2X

FIGURE 5-8. LONGITUDINAL SECTIONS FROM SAMPLE NO. 255. See Figure 5-11.

47832 16X

(a)

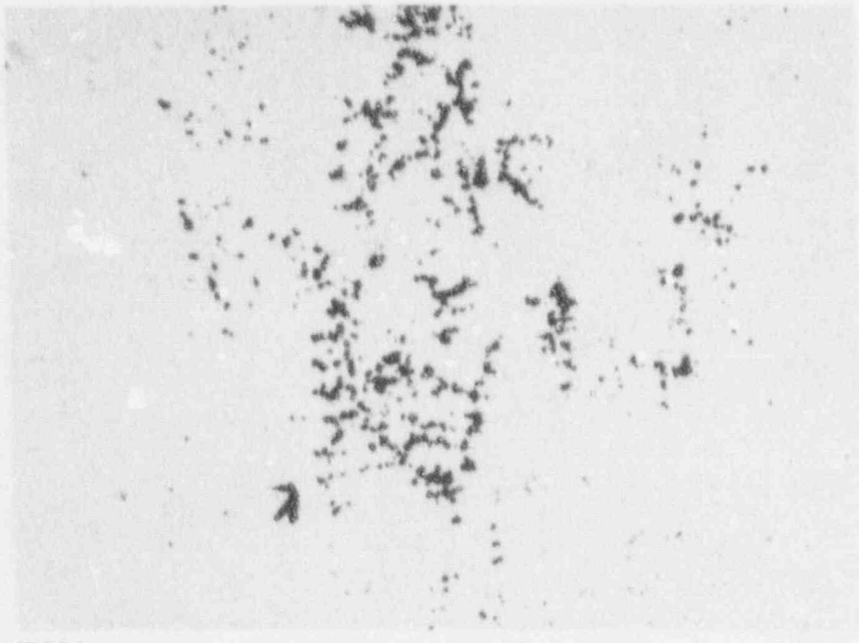

47831 16X

(b)

FIGURE 5-9. LONGITUDINAL SECTION FROM SAMPLE NO. 255 (10-in). See Figure 5-11. Section A_1-A_1 + 0.88-in. As polished.

47900 2X

(a) Section B_o-B_o-

47813 2X

(b) Section B_o-B_o + 0.19-in.

47814 2X

(c) Section B_o-B_o + 0.29-in.

Note: Grinding to B_o-B_o + 0.40-in. removed flaw.

FIGURE 5-10. TRANSVERSE SECTION FROM SAMPLE NO. 255 (10-in.) See Figure 5-11. Etchant: Vilella's reagent

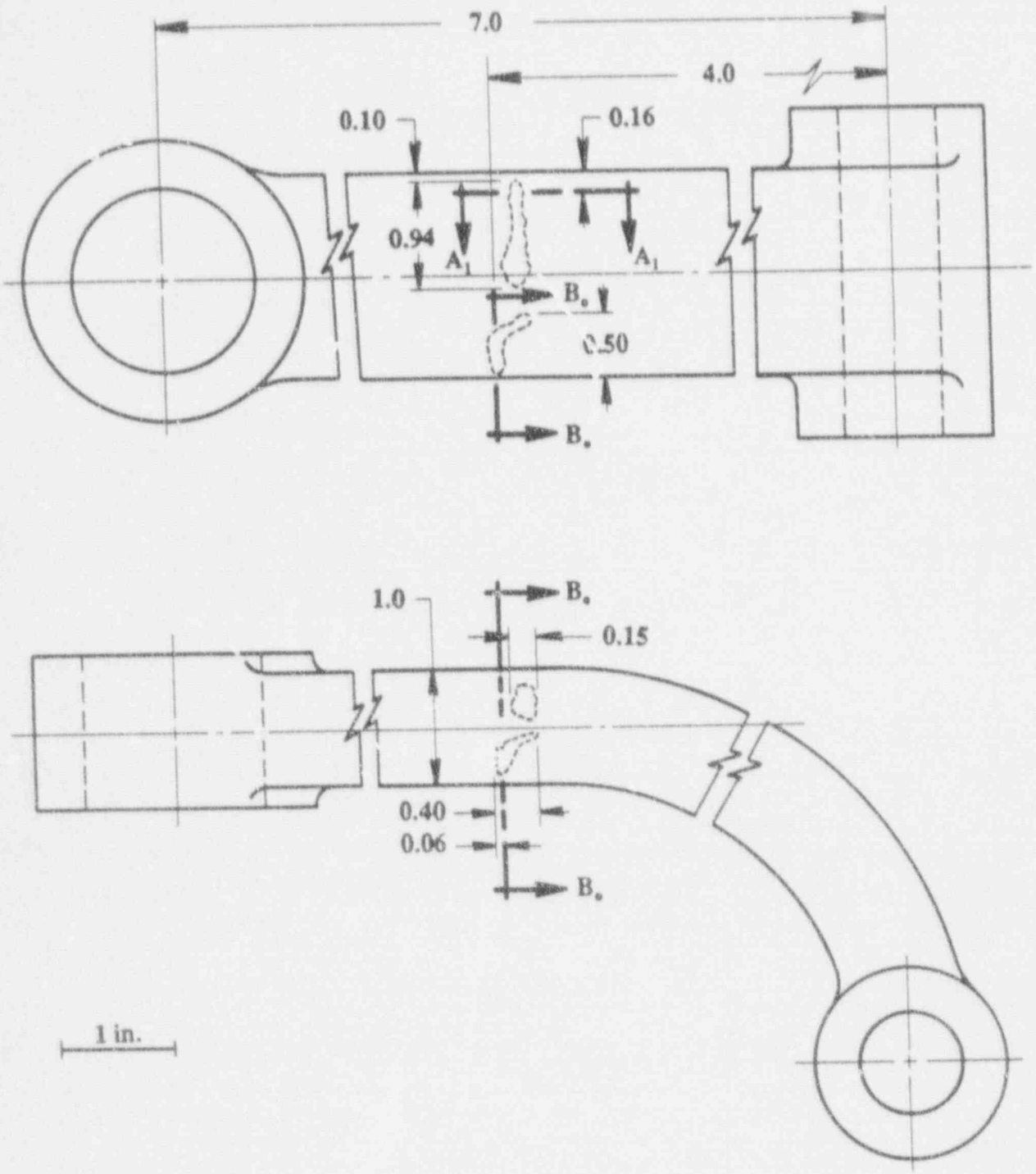

FIGURE 5-11. DIAGRAM OF INTERNAL VOIDS IN SAMPLE NO. 255 (10-in.). See Figures 5-8, 5-9 and 5-10.

47929 16X

(a) Section A_o-A_o + 0.54-in.

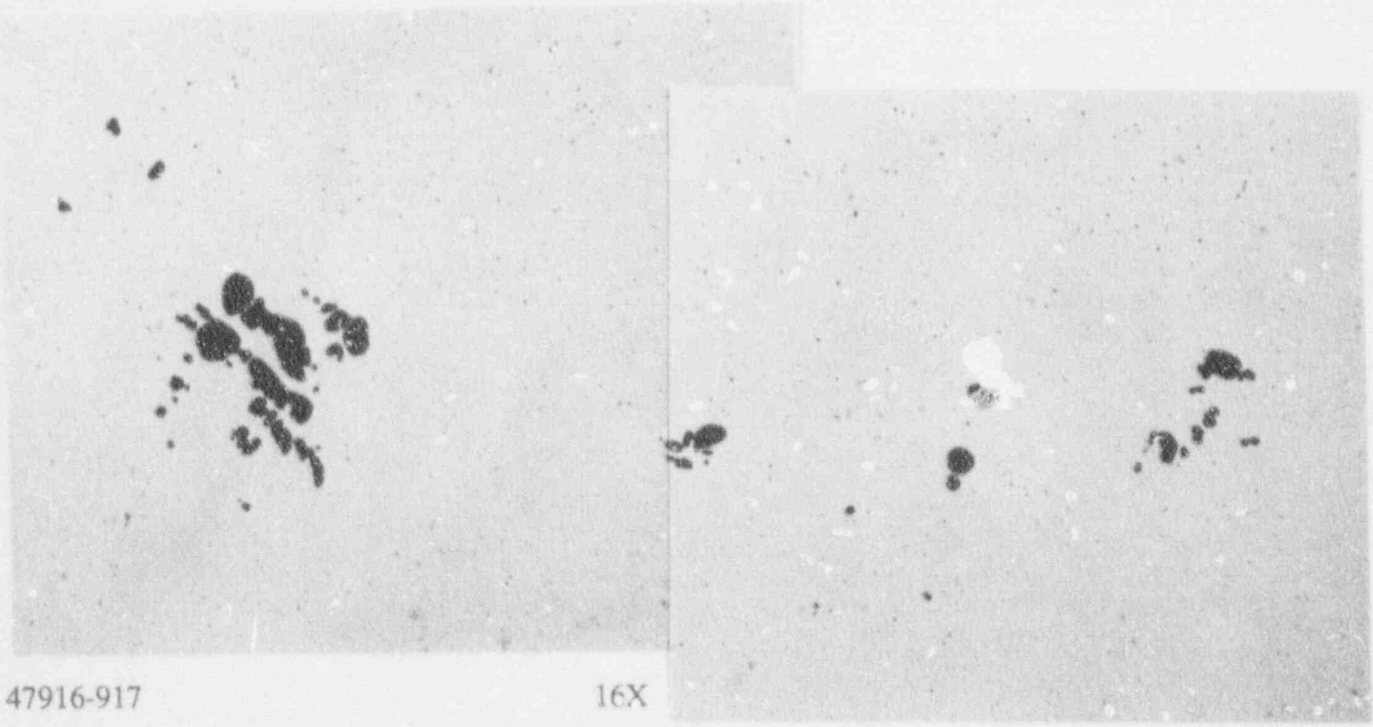

47916-917 16X

(b) Section A_o-A_o + 0.58-in.

FIGURE 5-12. TRANSVERSE SECTIONS FROM SAMPLE NO. 242 (8-in.).
See Figure 5-16 for locations. As polished.

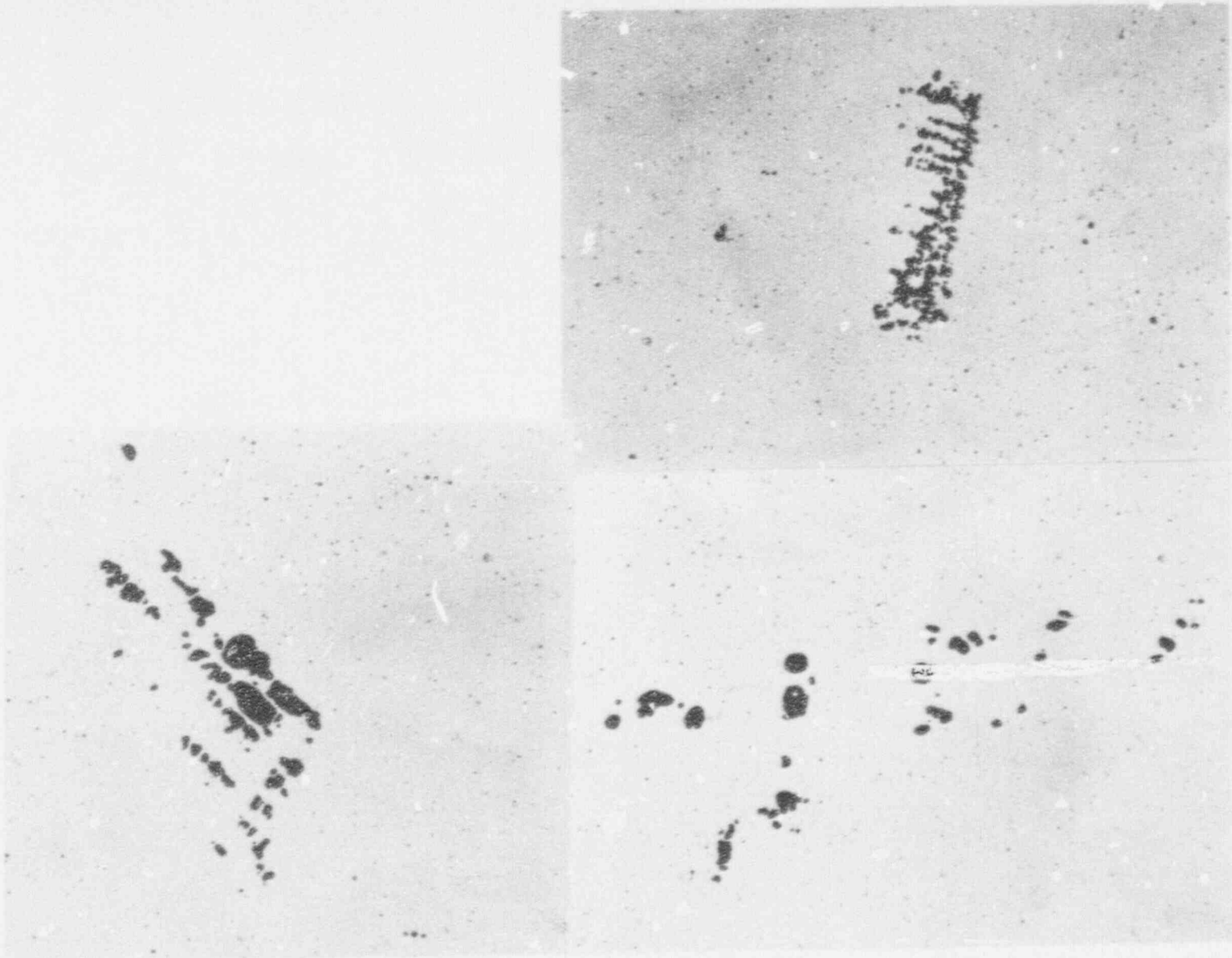

47913-915

16X

Section A_o-A_o + 0.64-in.

FIGURE 5-13. TRANSVERSE SECTION FROM SAMPLE NO. 242 (8-in.). See Figure 5-16 for location. As polished.

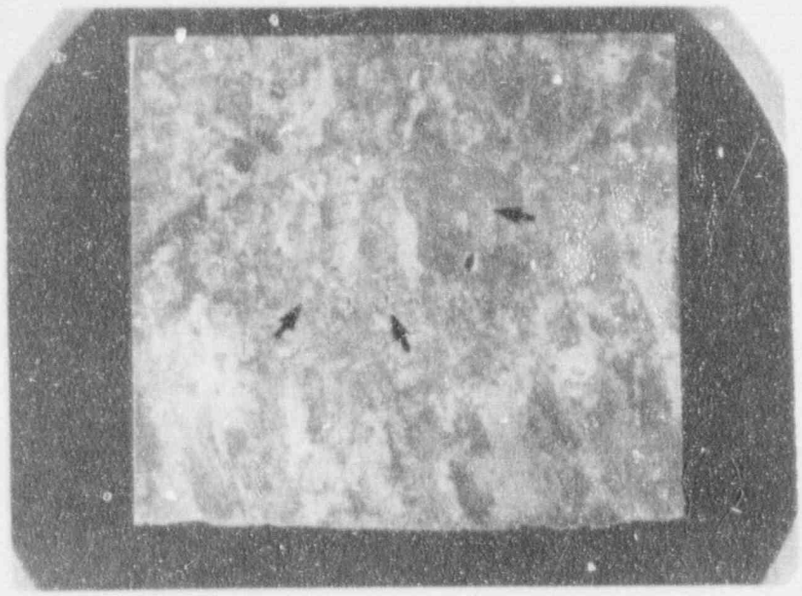

47944 4X

(a) Etched. Arrows mark smaller voids.

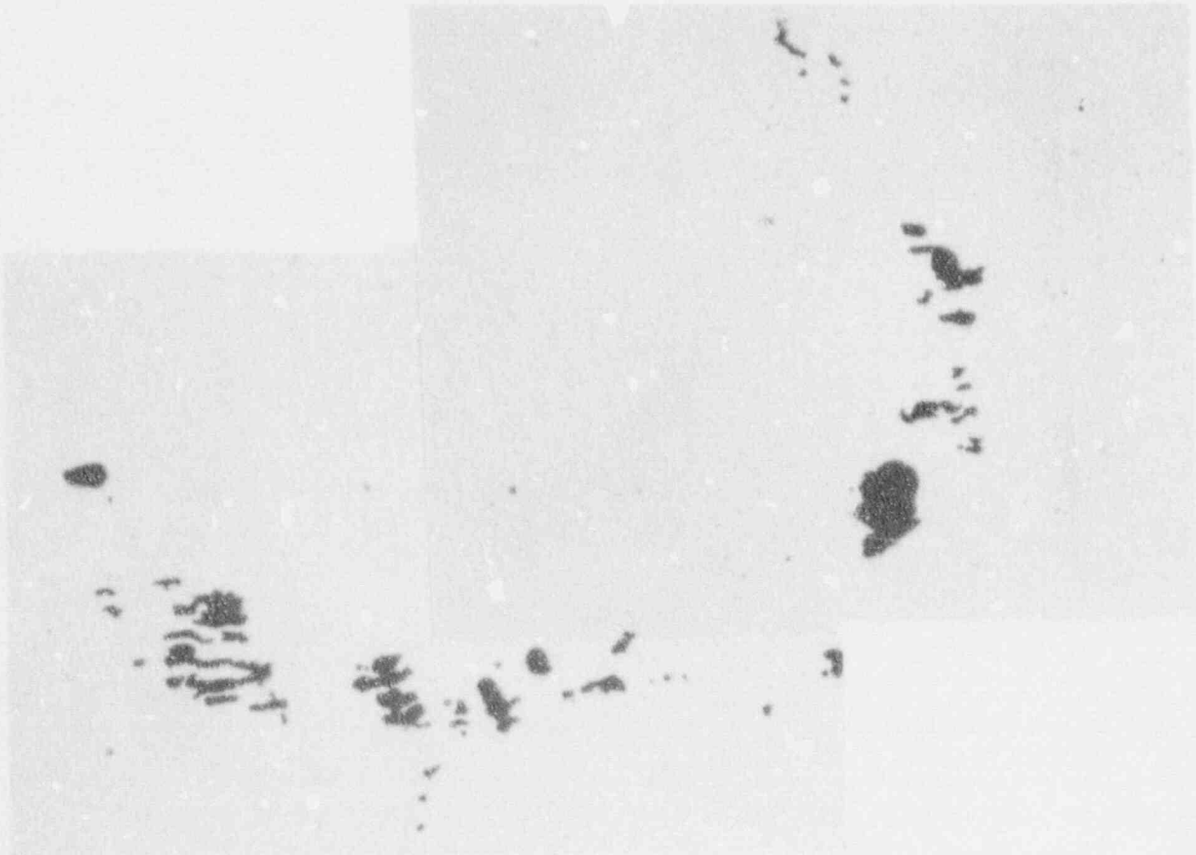

47935-936 16X

(b) As polished

FIGURE 5-14. TRANSVERSE SECTION FROM SAMPLE NO. 242 (8-in).
Section A_o-A_o + 0.78. See Figure 5-16 for location.

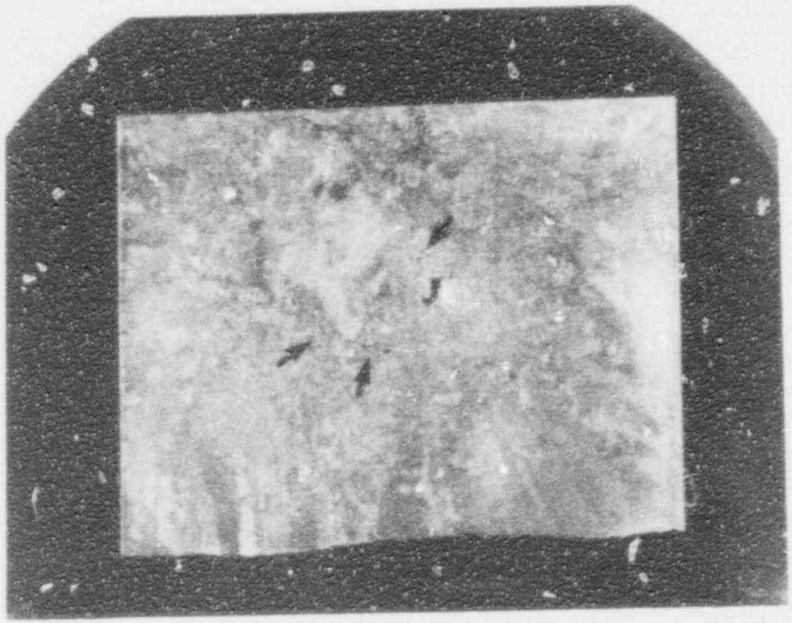

47955 4X

(a) Etched. Arrows mark smaller voids.

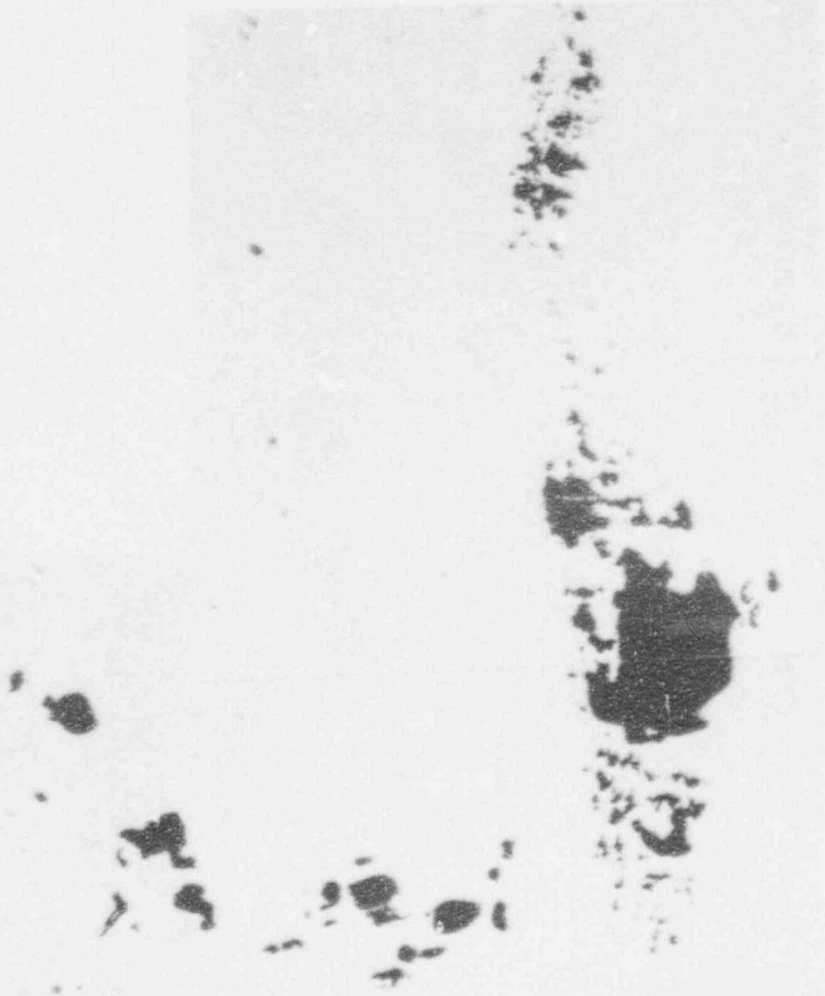

47952-953

(b) As polished

FIGURE 5-15. TRANSVERSE SECTION FROM SAMPLE NO. 242 (8-in.).
Section A_o-A_o + 0.84-in.

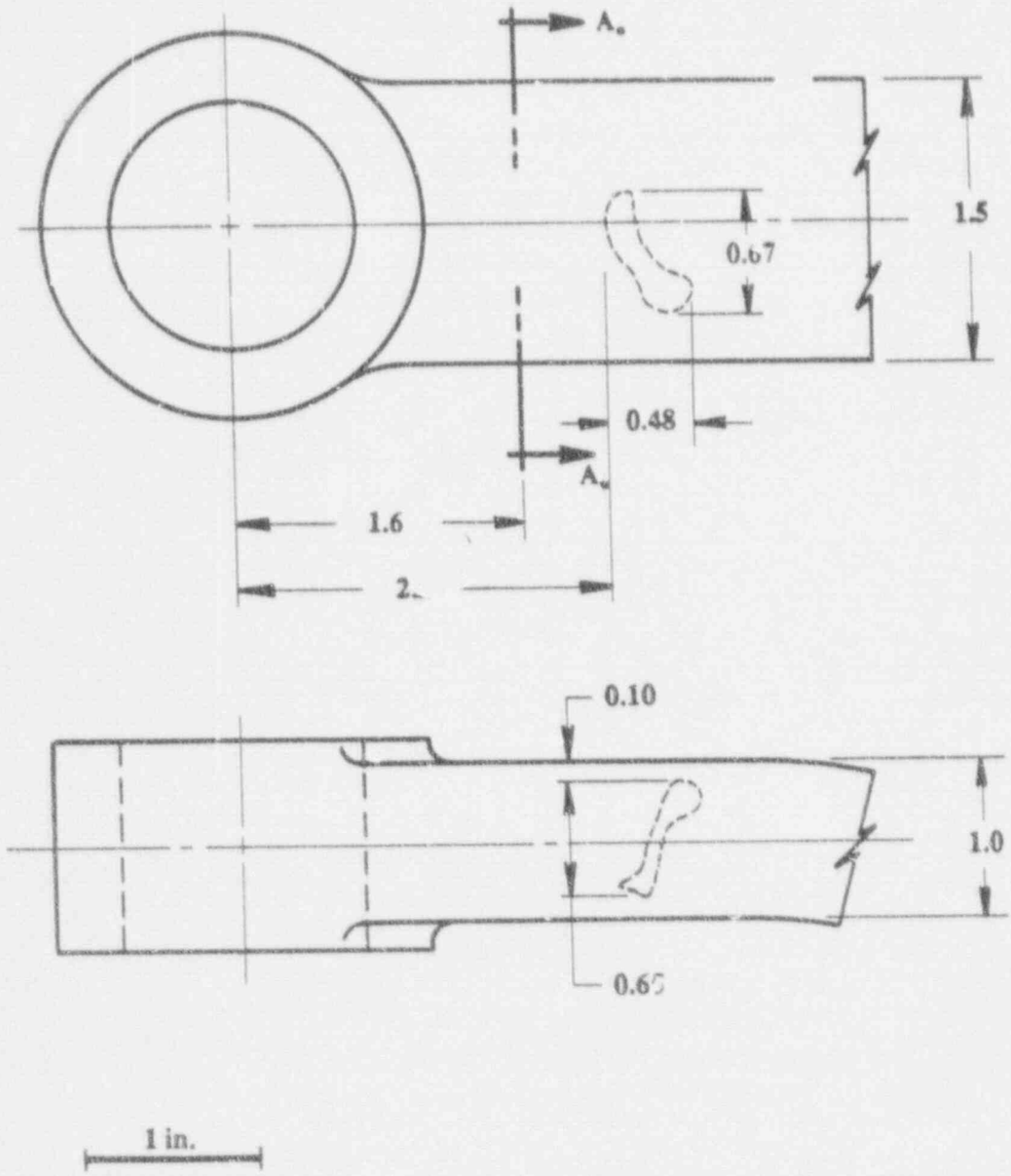

FIGURE 5-16. DIAGRAM OF INTERNAL FLAW IN SAMPLE NO. 242 (8-in.)
Outlined areas represent volume containing concentration of small voids. See Figures 5-12 through 5-15. Scale is approximate.

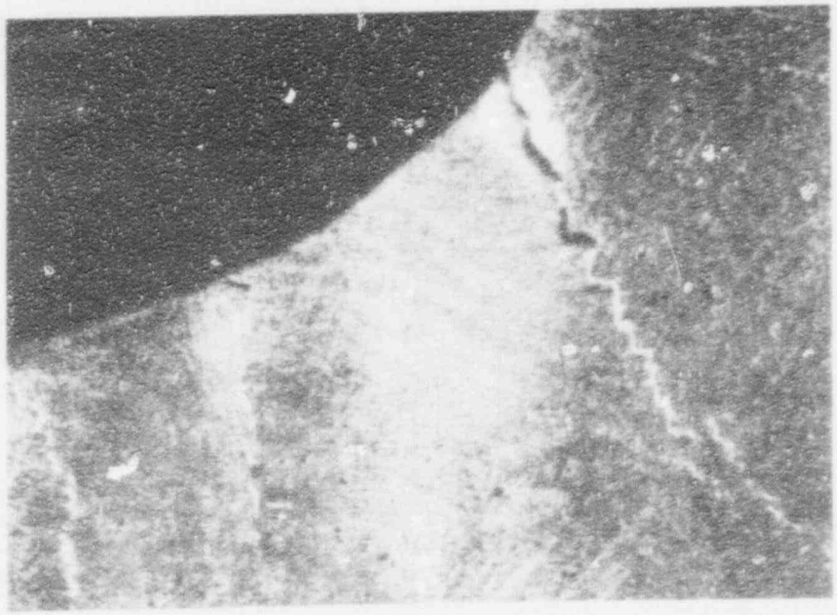

47234 (a) Section A-A. 16X

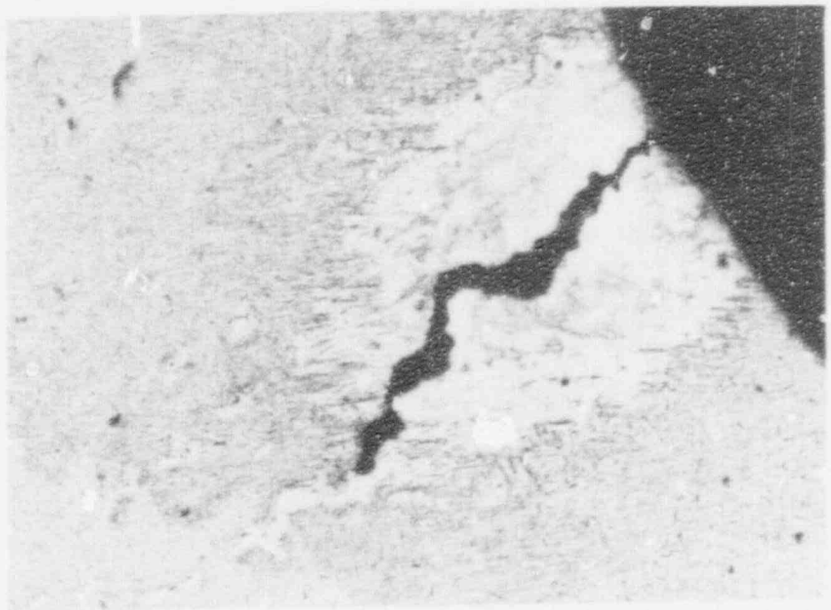

47311 (b) Section B-B. 50X

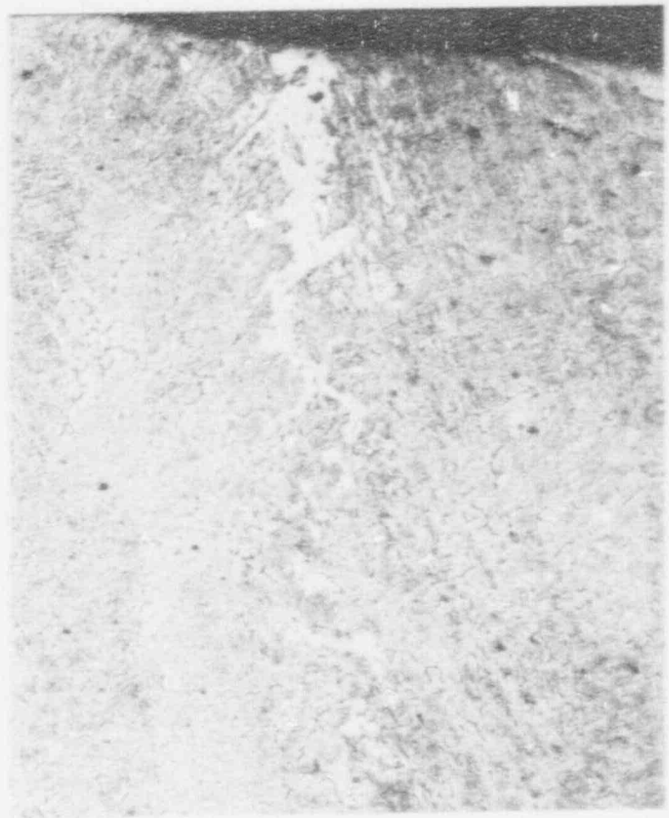

47231 50X

(c) Section C-C.

FIGURE 5-17. SURFACE CONNECTED FLAW IN SAMPLE NO. 255 (10-in.). Note different magnifications. Section designations correspond to Figure 4-1. Etchant: Vilella's reagent

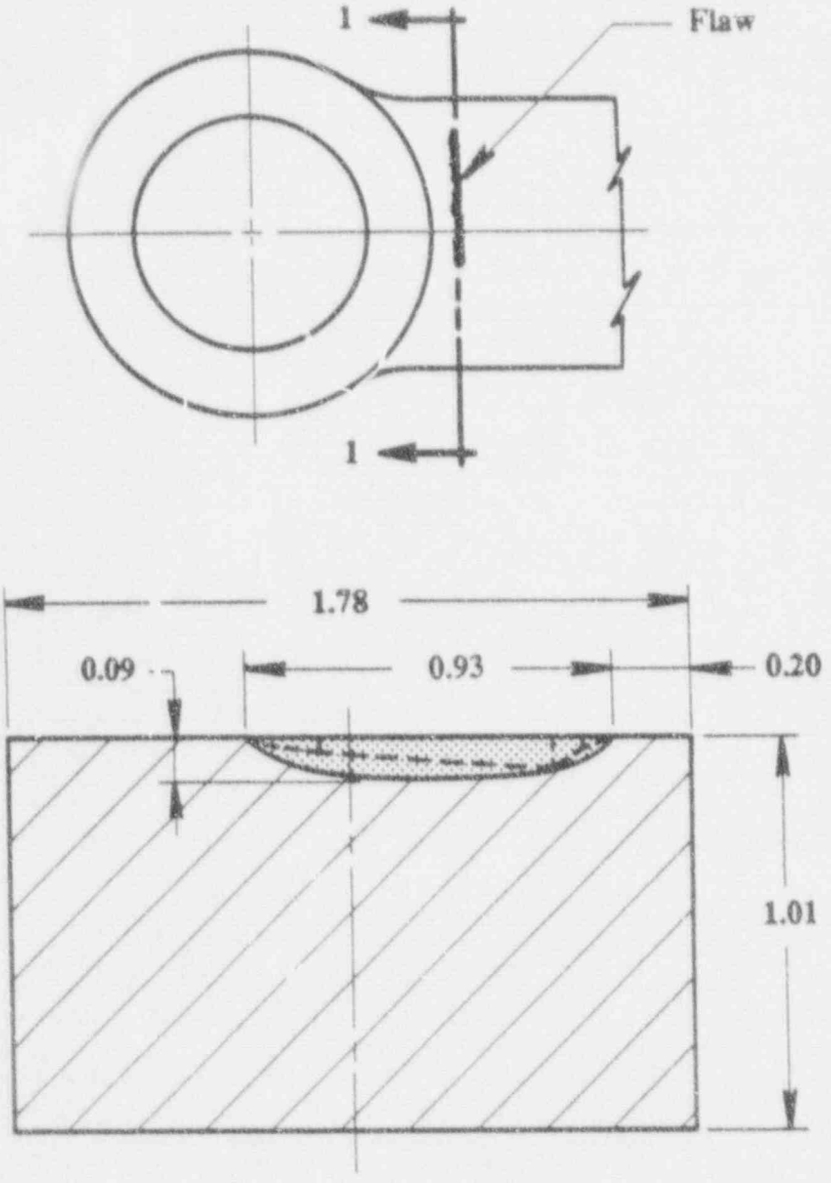

Section 1-1. Twice size.

FIGURE 5-18. DIAGRAM OF SURFACE-CONNECTED FLAW IN SAMPLE NO. 255 (16-in.). Transverse section of swing arm. Dotted line connects points of measured depths in metallographic sections. Shaded area represents flaw as a semi-elliptical shape.

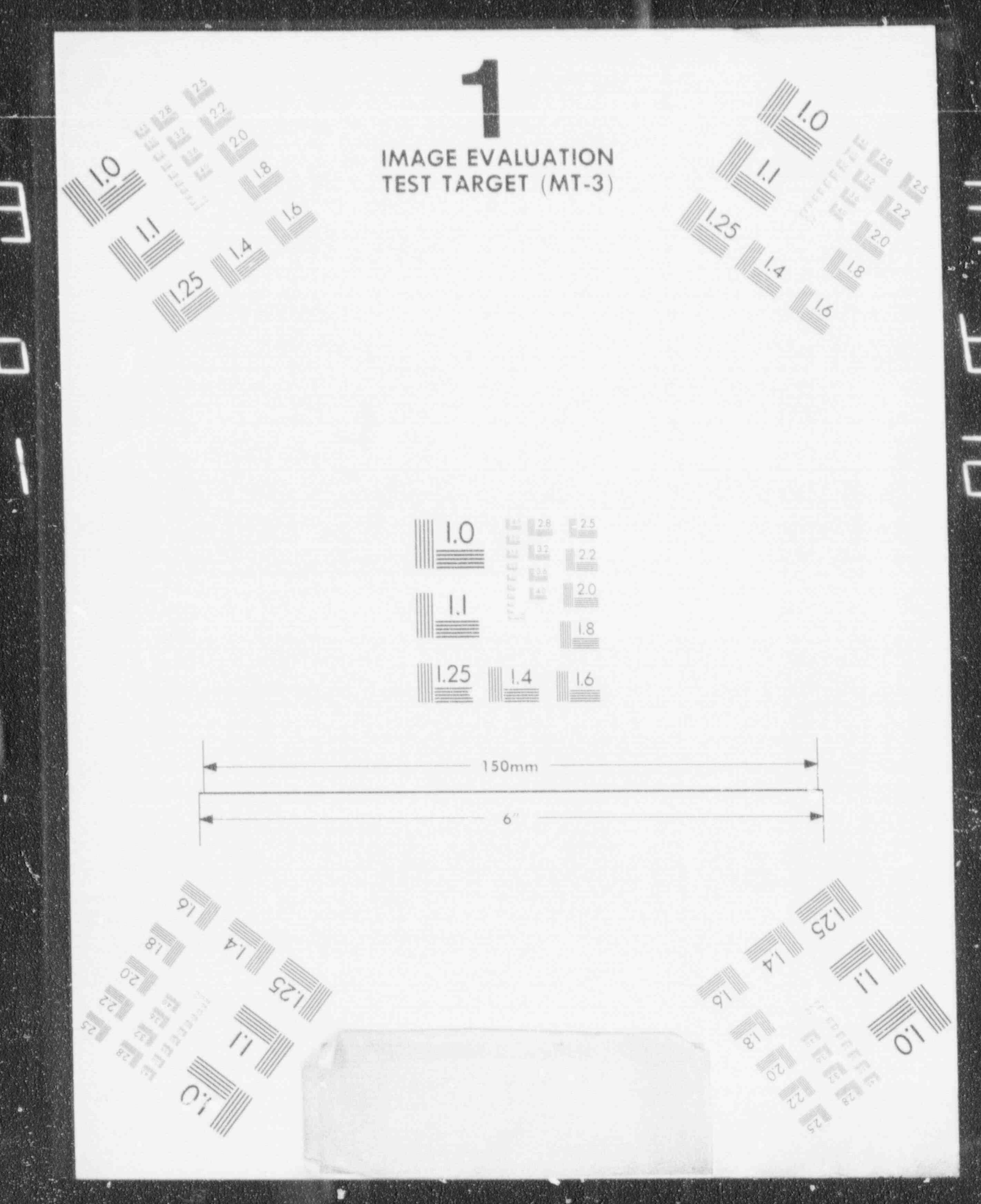
1
IMAGE EVALUATION
TEST TARGET (MT-3)
1.0
1.1
1.25
1.4
1.6
1.8
2.0
2.2
2.5
2.8
3.2
3.6
4.0
150mm
6"

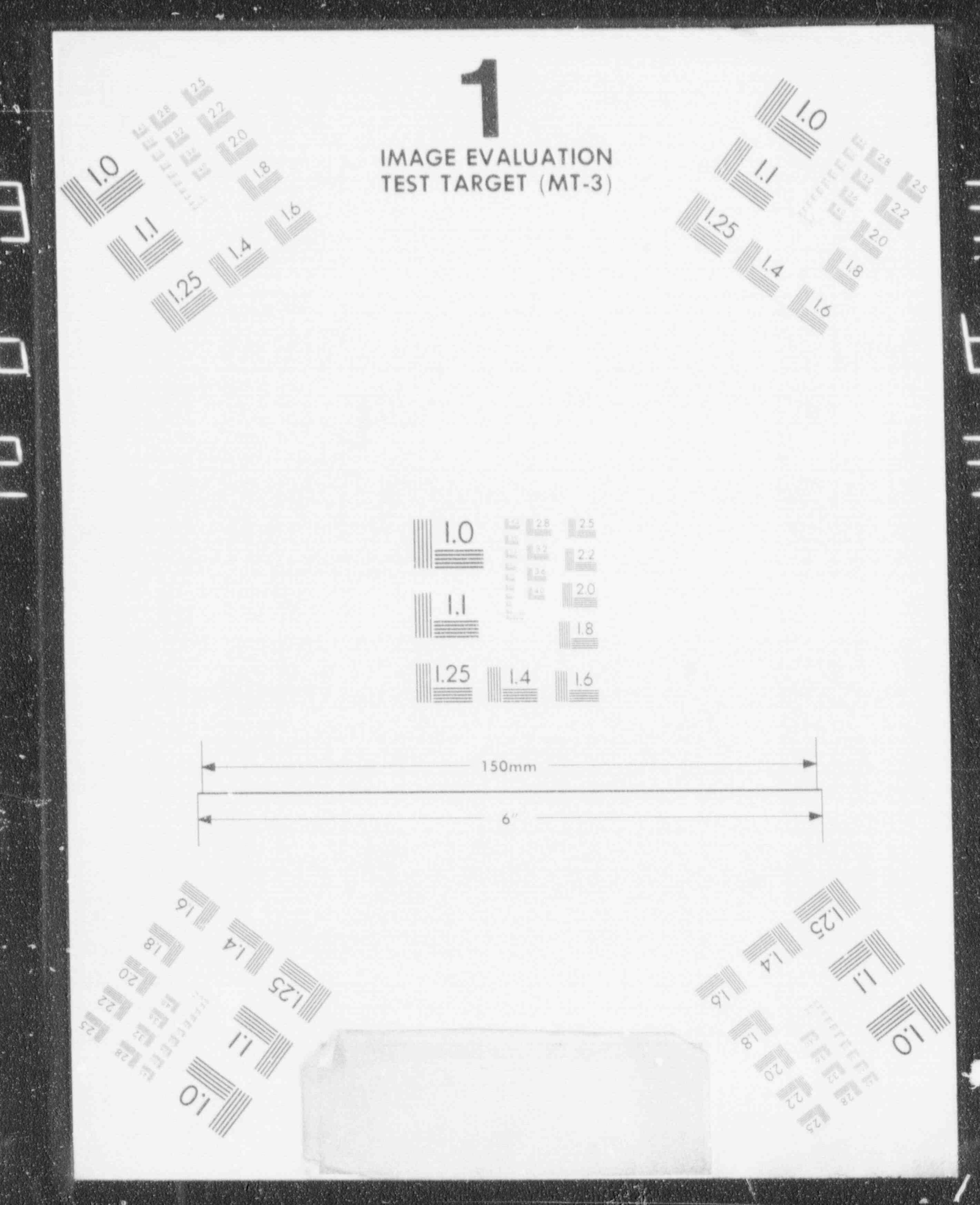
1
IMAGE EVALUATION
TEST TARGET (MT-3)
1.0
1.1
1.25
1.4
1.6
1.8
2.0
2.2
2.5
2.8
3.2
3.6
4.0
150mm
6"

1

IMAGE EVALUATION
TEST TARGET (MT-3)

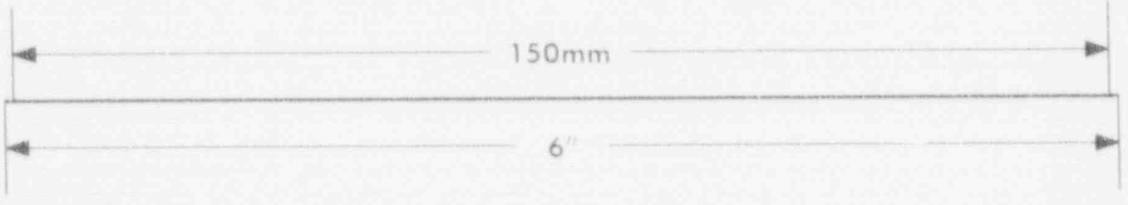

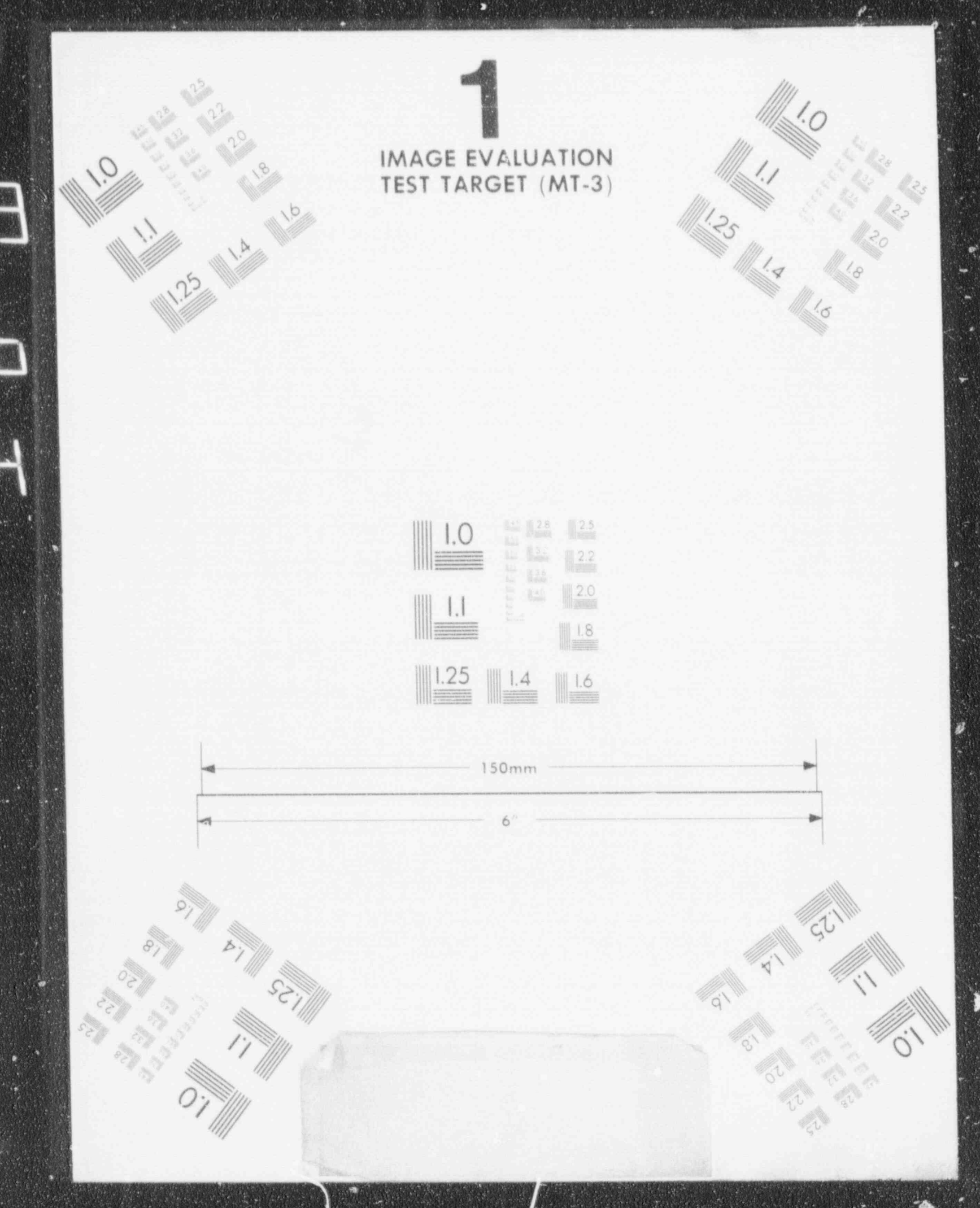
1
IMAGE EVALUATION
TEST TARGET (MT-3)
1.0
1.1
1.25
1.4
1.6
1.8
2.0
2.2
2.5
2.8
3.2
3.6
4.0
150mm
6"

47381 100X

(a) Sample No. 245 (4-in.). Section B-B, Figure 4-1. Right-hand edge is bore of valve disk boss. Repair weld is at top of boss.

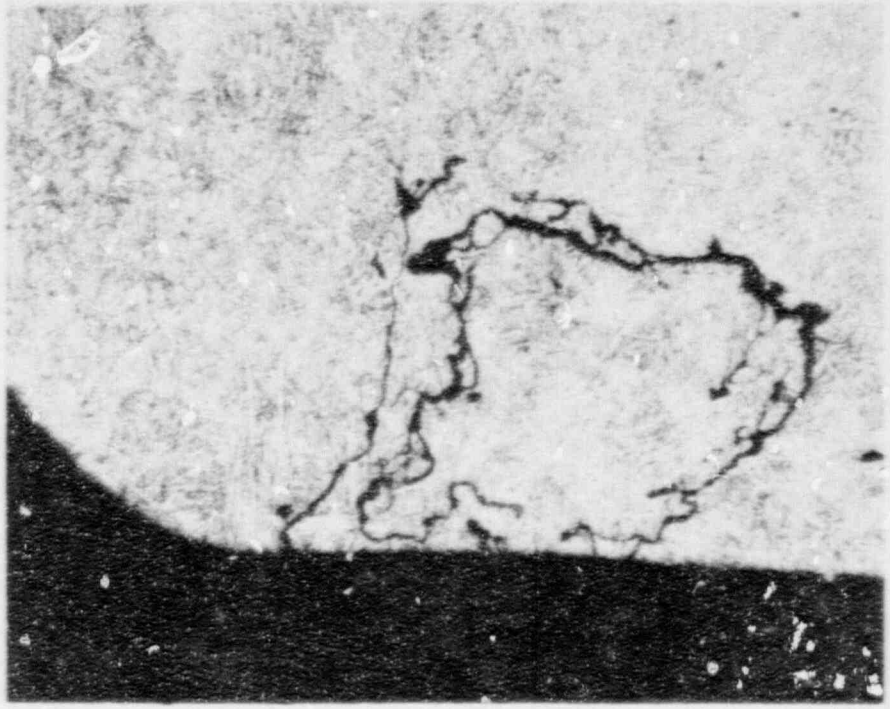

47476 106X

(b) Sample No. 263 (3-in.). Section C-C, Figure 4-1.

FIGURE 5-19. MICROFISSURES IN 4-in. AND 3-in. SWING ARMS. Etchant: Vilella's reagent

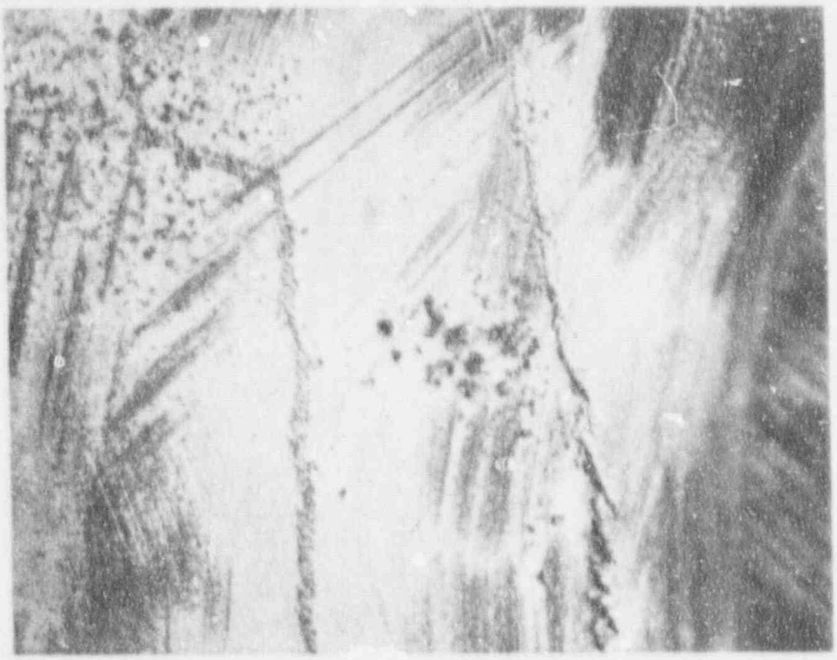

47079 5X

(a) Voids in original surface.

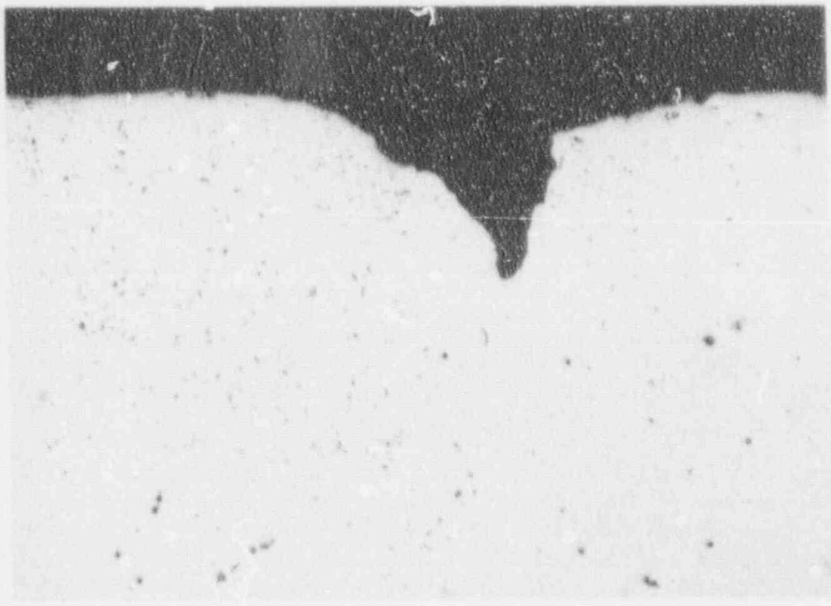

47082 100X

(b) Metallographic section through voids in (a). (As polished)

FIGURE 5-20. SURFACE CONNECTED VOIDS IN SAMPLE NO. 243 (8-in.). Location in arm-to-disk boss transition.

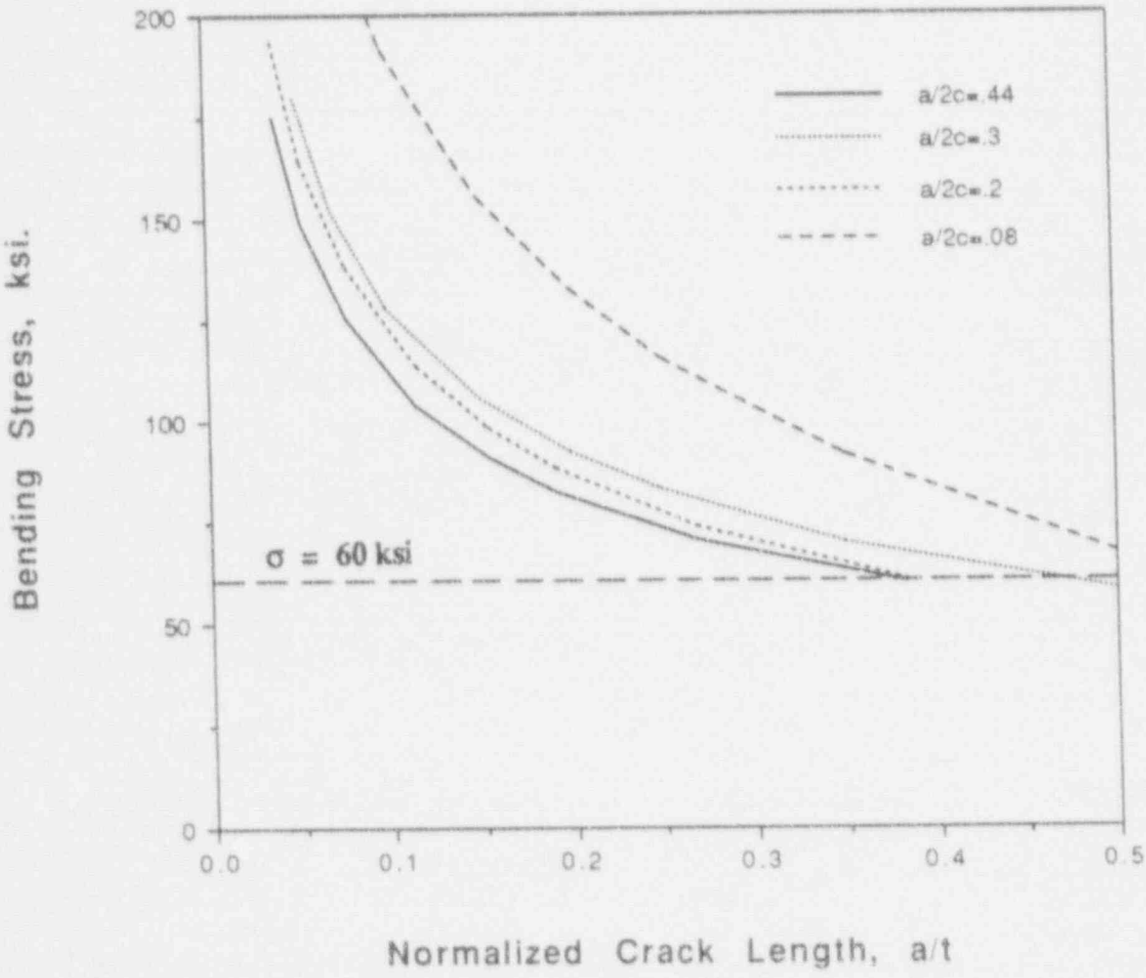

FIGURE 5-21. FRACTURE STRESS VS. CRACK DEPTH FOR K_{IC} = 50 ksi$\sqrt{in}$. Semi-elliptical, surface-connected crack.

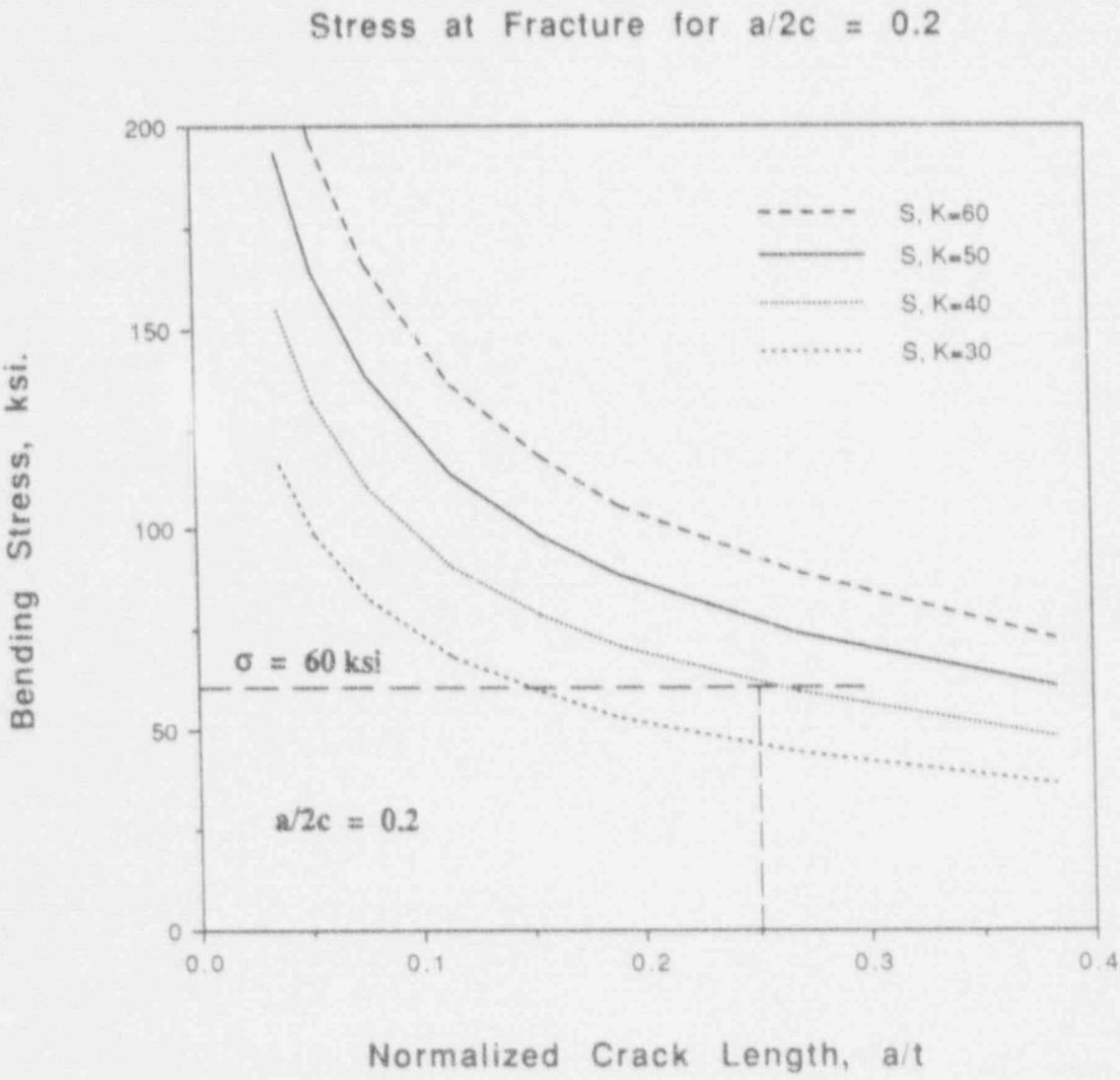

FIGURE 5-22. **FRACTURE STRESS VS. CRACK DEPTH FOR TYPICAL CRACK GEOMETRY**. Semi-elliptical, surface-connected crack.

6.0 FRACTURE TOUGHNESS

Fracture toughness testing provides a measure of the resistance to fracture for a given material. Fracture toughness tests can be broken into two categories, i.e., plane-strain fracture toughness tests (K_{IC}), determinations of fracture toughness by means of the parameter J_{IC} in cases where stable crack extension occurs prior to fracture.

The property K_{IC} characterizes the resistance of a material to fracture in the presence of a sharp crack in a neutral environment under conditions of a state of stress approaching tri-axial plane strain near the crack front, and a small crack-tip plastic region compared with the crack size and specimen dimensions [5]. K_{IC} represents a lower limiting value of fracture toughness and is determined directly in tests where plane strain conditions prevail at fracture. If, however, the specimen exhibits stable crack growth during the test, a plane-strain analysis is not appropriate. Instead, a J_{IC} analysis is required, where J_{IC} is the critical value of the J-integral near the onset of stable crack extension [6]. Subject to certain limitations, the parameter J_{IC} may be converted to an equivalent value for plane-strain fracture toughness, K_{IC}.

6.1 Test Procedures

Both K_{IC} and J_{IC} testing procedures are similar and employ compact tension specimens of the type shown in Figure 6-1. In both types of test, the specimens are loaded in the manner shown and the crack opening displacement (COD) is measured as a function of load. Prior to testing, the specimens are fatigue precracked to initiate a sharp crack at the root of the deep notch. The specimens are machined to provide specific B/W and a/w ratios. In this investigation, compact tension specimens of the designs shown in Figures 6-2, 6-3, and 6-4 were used to determine fracture toughness values. Three different specimen sizes were required because of the variation in swing arm dimensions among the 16 specimens. The distance (W) from the centerline of the pins to the back edge is 1.5 in., 1.0 in., and 0.76 in. for Type A, Type B, and Type C, respectively. Type A and B specimens are of the sizes commonly used for fracture toughness testing. While Type C is of the same geometry as Type A and B specimens, the size is slightly less than accepted standards. The adequacy of these smaller specimens was investigated during the course of the program.

The location selected for removal of the specimen coupon from each swing arm was based primarily on the individual sample size and defect locations. Specimen locations were chosen to avoid radiographic indications and areas of weld repair. The orientation of the crack path for each specimen was consistently chosen such that crack propagation would be across the width of the arm. Figure 6-5 shows the typical location and orientation of a fracture toughness specimen in a swing arm.

Prior to testing, each specimen was polished on both sides to facilitate crack length measurements and then fatigue precracked. The fatigue crack was allowed to grow until the ratio of crack size to specimen width (a/W) was between 0.45 and 0.55. While the cyclic load necessary to initiate a crack may be reasonably high, the load was decreased as the precracking progresses, such that the final precrack load is well below the anticipated test condition.

All tests were computer controlled and were analyzed by standard analysis software packages. A displacement gage was clipped onto the front face of the specimen to monitor crack opening displacement. This displacement was then converted to a change in crack size by the compliance method.* The major difference between the K_{IC} and J_{IC} test procedures is that in the K_{IC} test the specimen fails with no significant slow crack growth prior to catastrophic fracture, while the J_{IC} test exhibits significant stable crack growth. Each test was conducted under the assumption that it would behave like a J_{IC} test. If instead the specimen failed without any crack extension, a K_{IC} analysis was performed. The only data required for a K_{IC} analysis are the crack size and the load at which the specimen failed.

In a J_{IC} type fracture toughness test, periodic unloads are employed to generate periods of stable crack growth. The compliance of each unload is then used to calculate changes in crack length throughout the test. By monitoring the load and changes in compliance, a plot of J versus crack extension (Δa) can be generated. An example of the raw data and the final analysis to obtain a J_{IC} value are graphically shown in Figures 6-6 and 6-7, respectively.

---

* Compliance is defined as the slope of the load versus crack opening displacement curve and is obtained by a clip gage mounted on the load line of the specimen [7].

Figure 6-6 presents the data obtained during a J_{IC} test as load versus crack opening displacement. During the periodic unloads, the load is dropped 40%, to ensure that a good slope of the compliance can be obtained. In Figure 6-7 the calculated value of J is plotted against crack growth for each point. Both a linear regression and a power law fit to the data are shown. Line A is the blunting line, which is a function of yield strength and crack growth. Lines B and D are exclusion lines, outside of which data are discarded. Line C is a 0.02 inch offset from the blunting line. The value of J_{IC} is defined as the intersection of the power law fit to the data with Line C. A J_{IC} value can then be converted to an equivalent K_{IC} by the formula $K_{IC} = \sqrt{J_{IC}E/(1-\nu^2)}$, where E=Youngs Modulus and ν=Poisson's ratio. For more specific details on fracture toughness testing, refer to the applicable test standards used for this program (ASTM E 399 for K_{IC} and ASTM E 813 for J_{IC}, see Refs. 5 and 6).

6.2 Test Results

Specimen coupons were sectioned from all 16 swing arms and machined into fracture toughness specimens. The test results for these swing arms are shown in Table 6-1. Two Type A specimens were machined from each of the 16-inch valve swing arms. For each of these two arms, one of the specimens was tested at room temperature and one was tested at 40°F. Since the operating temperatures for the swing arms range as low as 40°F, these tests were necessary to investigate the temperature dependence of fracture toughness down to that lower temperature.

As can be seen from Table 6-1, no appreciable difference was found between the room temperature tests (239-2 and 240-2) and the 40°F tests (239-3 and 240-3). For each pair of tests, the K_{IC} values were within the scatter band for the complete series of tests and the 40°F values were, in fact, slightly higher than the corresponding room temperature values. These results indicate that the fracture toughness of the cast 17-4PH material does not exhibit a strong temperature dependence for the range of temperatures of interest. The remainder of the fracture toughness tests were conducted at room temperature, with confidence that the results are applicable to actual swing arm operating conditions.

Since some of the swing arms were too small to provide standard size specimens, a non-conventional specimen geometry (Type C) was necessary for some of the tests. Although all of the relative dimensions correspond to ASTM specifications, there was some concern as to whether the small specimens would provide reliable fracture toughness values. In order to evaluate the reliability of these subsize specimens, Type C specimens were machined from broken halves of two Type A specimens (239-2 and 240-2). Table 6-1 shows that no appreciable differences exist between the results obtained with standard and subsize compact tension specimens for this material.

Table 6-1 provides a population of data for the 16 swing arms investigated. The K_{IC} values range from 53.5 to 115.3 ksi$\sqrt{in}$ with a median value of 74.2 ksi$\sqrt{in}$ and a mean value of 78.4 ksi$\sqrt{in}$. There are no apparent correlations between K_{IC} values and either valve size or specimen geometry. Thus, the data are treated as a single population. A histogram of the data is plotted in Figure 6-8 and shows a general grouping in K_{IC} values between 60 and 80 ksi$\sqrt{in}$. For this matrix of tests, scatter in the data does not come from specimen size or valve size, but can instead be attributed to the inherent variation in material properties for cast steel.

Specimen No. 260-2 failed during the precracking process. However, since the precrack load and final crack length before failure were known, a good estimate of K_{IC} was obtained for this swing arm. It is of interest to note that Sample No. 260 was the one sample which did not conform to the compositional and hardness requirements.

Certain requirements are specified by the ASTM specifications to have a truly valid K_{IC} or J_{IC} test. A few of these requirements were not met by this material. Crack length measurements were made at nine positions across the fractured specimen surfaces to obtain an average value for the initial crack size. According to specification (ASTM E 399 and E 813), these nine measurements should not vary from the mean value by more than 10%. None of the specimens met this criterion. Another validity check is in regard to the number of valid data points during the J_{IC} tests. For strict conformance to ASTM E 813, four data points during the test must have changes in crack length in the range from 0.006 to 0.06 inches. Six of the specimens (Nos. 239-2, 239-3, 239-2A, 244-2,

245-2, and 259-2) did not meet this requirement. However, the primary purpose of these two requirements is to eliminate scatter in the results.

The most important validity check is a restriction on the minimum thickness required. For a K_{IC} test to be in strict conformance with ASTM E 399, the thickness must exceed 2.5 $(K_{IC}/\sigma_{ys})^2$ where σ_{ys} is the yield strength. For a J_{IC} test (E 813), the thickness must exceed 25 (J_{IC}/σ_{ys}). All J_{IC} tests met the thickness requirement, but 6 out of the 8 K_{IC} tests did not meet this requirement. The last column in Table 6-1 tabulates the ratio of the specimen thickness to the thickness required to meet the validity requirement for the appropriate ASTM standard (E 399 or E 813). Thickness ratios greater than 1 indicate conformance to the specified thickness limitation and values less than 1 indicate non-conformance. Large values for this ratio are common for J_{IC} tests, since the thickness requirements for the J_{IC} tests are much less stringent than the K_{IC} thickness requirements. In Table 6-1 note that, for all cases where a J_{IC} analysis was required, the thickness ratios are much greater than 1.

The six tests for which the thickness ratios are less than 1.00 do not meet the strict E 399 thickness requirement for K_{IC} tests (240-2A, 240-3, 255-2, 242-2, 257-2, and 260-2). However, five of these ratios are greater than 0.60 and are considered reasonably close to the strict validity requirement. Situations such as these, where the specimen thicknesses are not far out of bounds, usually provide adequate constraint at the crack tip so that reliable fracture toughness data is obtained. The one case where the thickness ratio was only 0.51 (260-2) was the one swing arm which exhibited an abnormal microstructure and where the test specimen failed during precracking. Even there, the K_{IC} value determined falls within the scatter band of the data set. Adequate constraint for reliable test results was demonstrated by the fact that none of the fractured test specimens exhibited significant through-thickness plastic deformation, see Figures 6-9 through 6-12. The fact that adequate constraint did prevail is also evident in the lower values of K_{IC} seen for those specimens with thickness ratios less than 1.0. If inadequate specimen thickness led to inaccurate K_{IC} results, it would be expected that elevated values of K_{IC} would be obtained due to the loss of constraint.

Thus, the lower K_{IC} values associated with the low thickness ratios show that the specimen thicknesses did not adversely affect the results.

ASTM validity checks and requirements are designed to be guidelines in determining whether or not tests are yielding accurate results. Even if these validity requirements are not met, tests can still produce reliable results. Engineering judgement must be used to determine if those tests failing specific validity requirements yield results any different from these tests which meet the ASTM requirements.

6.3 Data Statistics

In order to evaluate the statistical characteristics of the test results, the set of 16 K_{IC} values was compared to four standard distributions to determine a goodness of fit. The distributions evaluated were normal, lognormal, Weibull, and EVD (extreme value distribution). Of the four, the EVD provided the best fit to the data. The details of the statistical evaluation are given in Appendix D.

Utilizing the EVD, the tolerance limits on the lower bound of the data set were determined. The results are that, for 95% of the similar swing arms still in service, there is a 95% confidence interval that the lower limit of fracture toughness is as follows. (See Appendix D.)

EVD distribution: $K_{IC} \geq 44 \text{ ksi}\sqrt{\text{in}}$

This lower limit value exceeds the maximum K_I values which are expected to be encountered in service (see Section 5.0). Lower bounds of fracture toughness for other levels of population and other confidence intervals are given in Appendix D, Table D-2.

TABLE 6-1

FRACTURE TOUGHNESS TEST RESULTS

Valve Size	Specimen No.	Specimen Geometry	J_{IC} Value (in-lb/in^2)	K_{IC} Value (ksi $\sqrt{in}$)	Thickness Ratio‡
16 in.	239-2	Type A	255	88.2	14.42
	239-2A	Type C	225	82.9*	8.26
	239-3	Type A	280	92.4**	13.16
	239 Avg.	--	--	87.8†	--
	240-2	Type A	--	61.3	1.22
	240-2A	Type C	--	58.7*	0.67
	240-3	Type A	--	71.4**	0.90
	240 Avg.	--	--	63.8†	--
10 in.	255-2	Type B	--	57.1	0.94
8 in.	242-2	Type B	--	70.1	0.62
	243-2	Type B	--	53.5	1.07
6 in.	244-2	Type B	430	109.7	5.75
	256-2	Type C	140	65.4	13.57
	257-2	Type B	--	65.6	0.71
4 in.	245-2	Type C	215	81.1	8.64
	258-2	Type C	180	74.2	10.56
	259-2	Type C	200	78.2	9.50
	260-2	Type C	--	67.4***	0.51
3 in.	246-2	Type C	180	74.2	10.56
	261-2	Type C	330	100.4	5.67
	262-2	Type C	435	115.3	4.32
	263-2	Type C	335	101.2	5.59

* Specimen machined from broken half of larger corresponding test specimen.

** Test conducted at 40°F.

*** Specimen failed during precrack.

† Average of three tests from a single swing arm.

‡ Ratio of actual specimen thickness to required thickness.

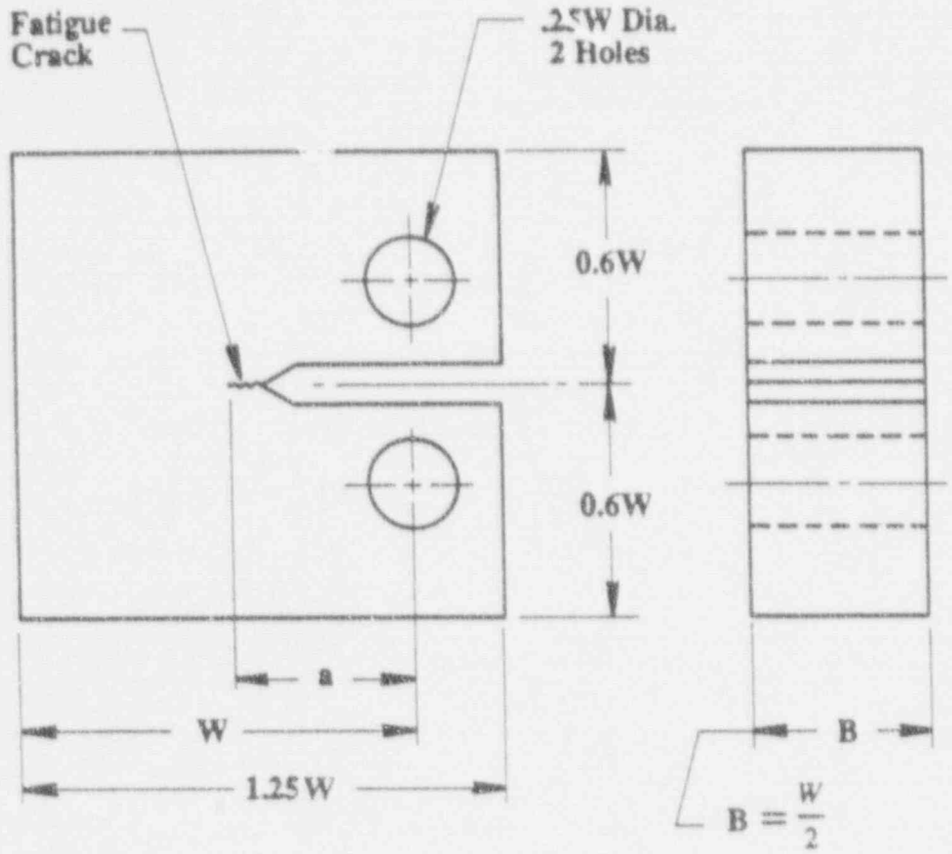

FIGURE 6-1. PROPORTIONS FOR COMPACT TENSION SPECIMENS EMPLOYED IN K_{IC} AND J_{IC} TESTS

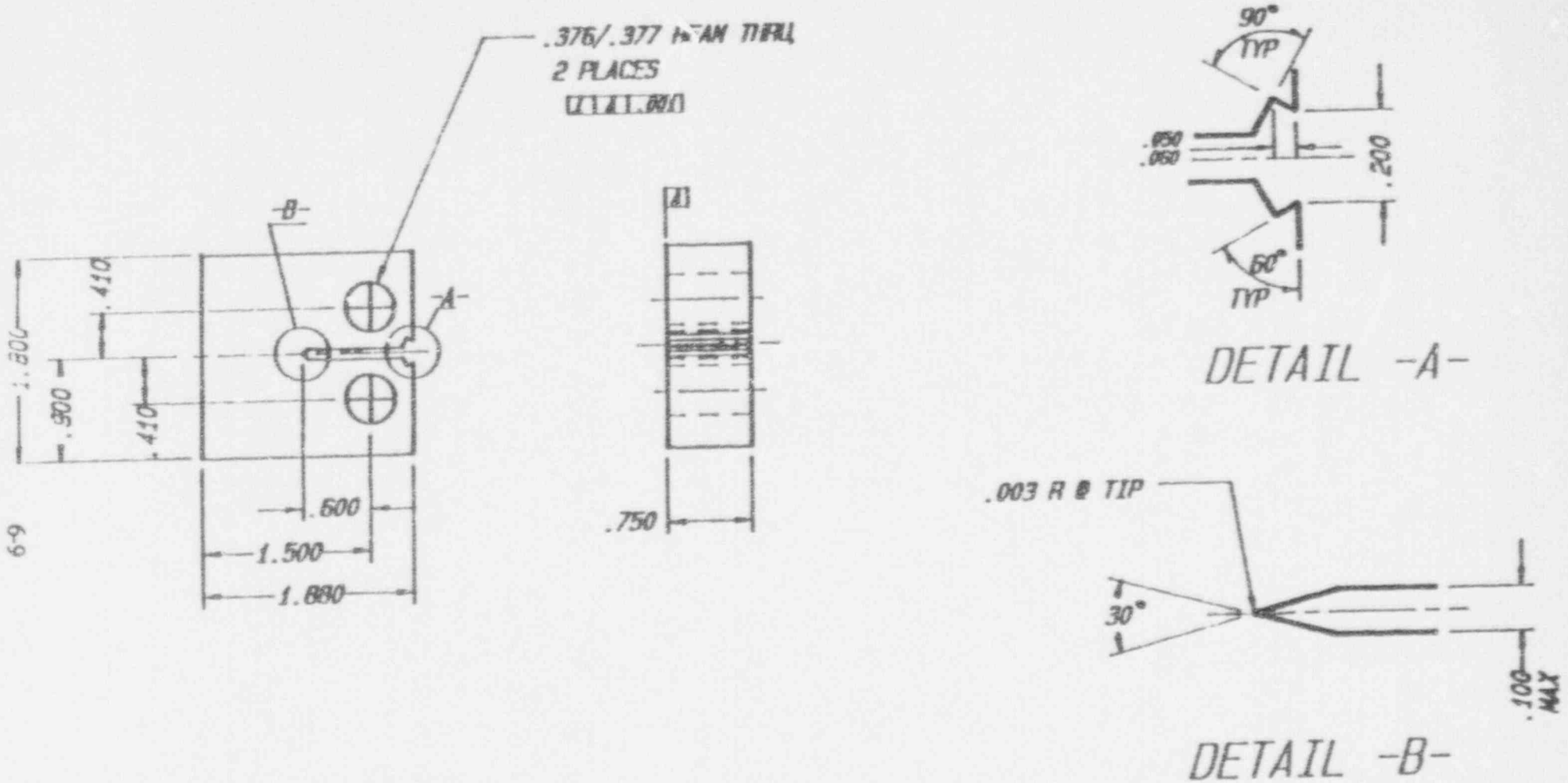

FIGURE 6-2. Type A Fracture Toughness Specimen (1.5W).

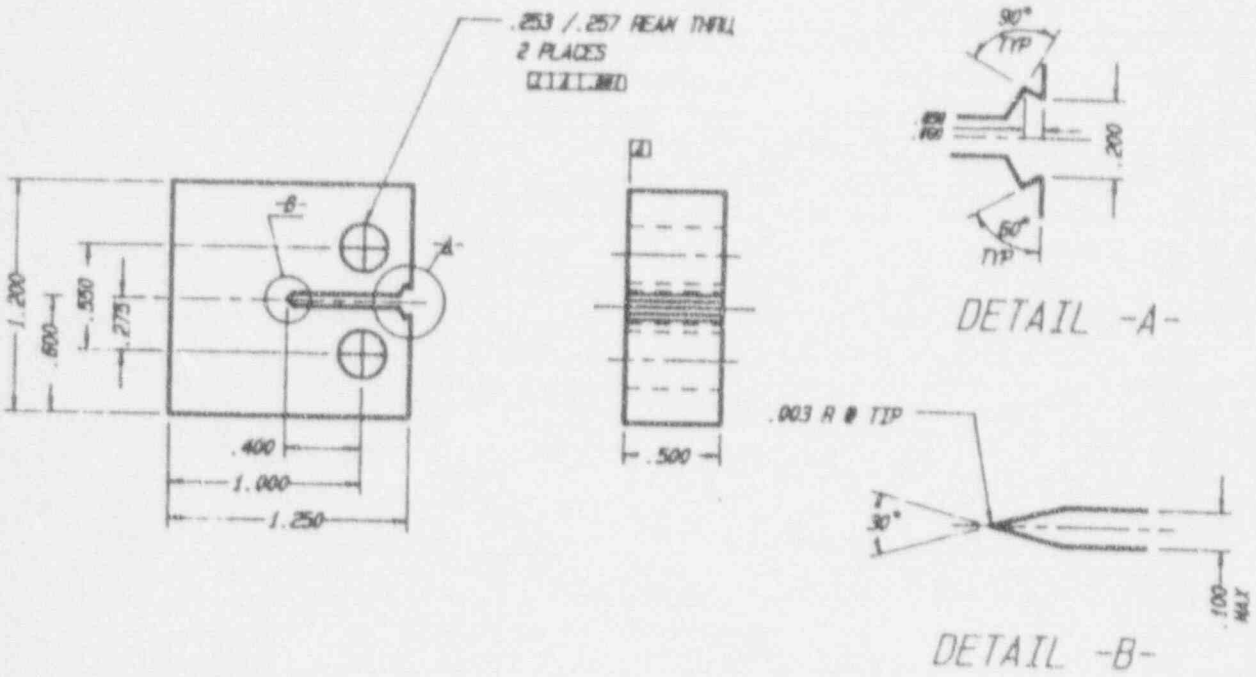

FIGURE 6-3. Type B Fracture Toughness Specimen (1W).

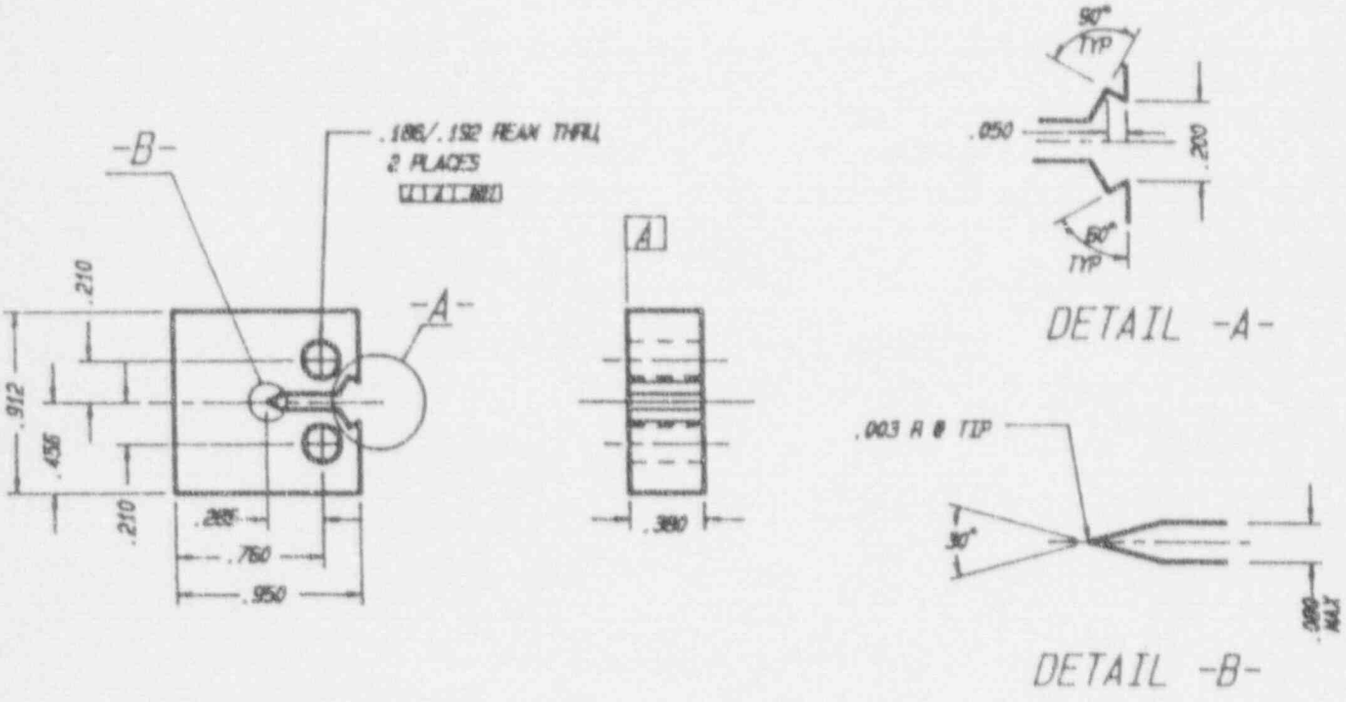

FIGURE 6-4. Type C Fracture Toughness Specimen (0.76W).

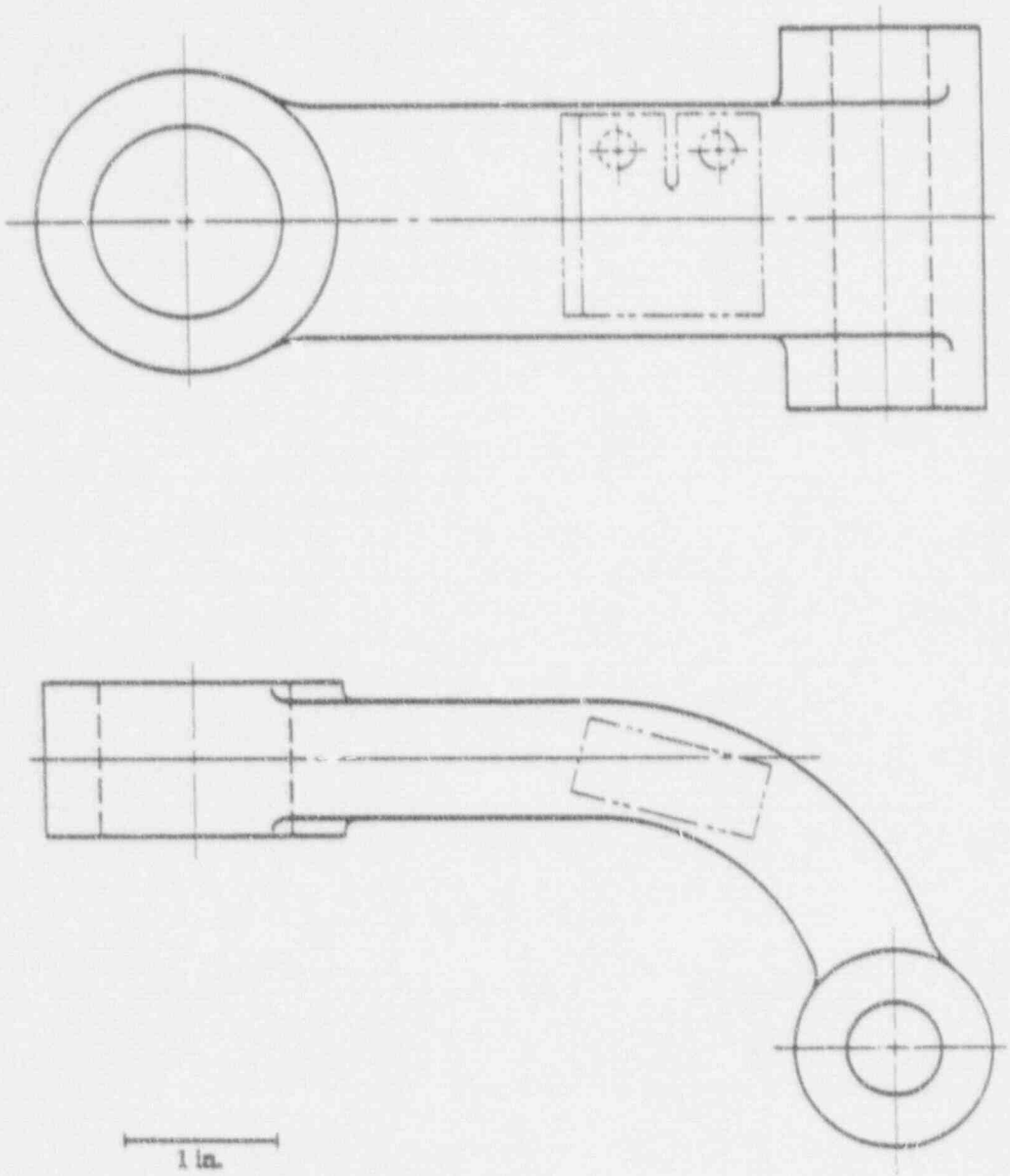

FIGURE 6-5. TYPICAL LOCATION AND ORIENTATION OF FRACTURE TOUGHNESS SPECIMEN IN SWING ARMS

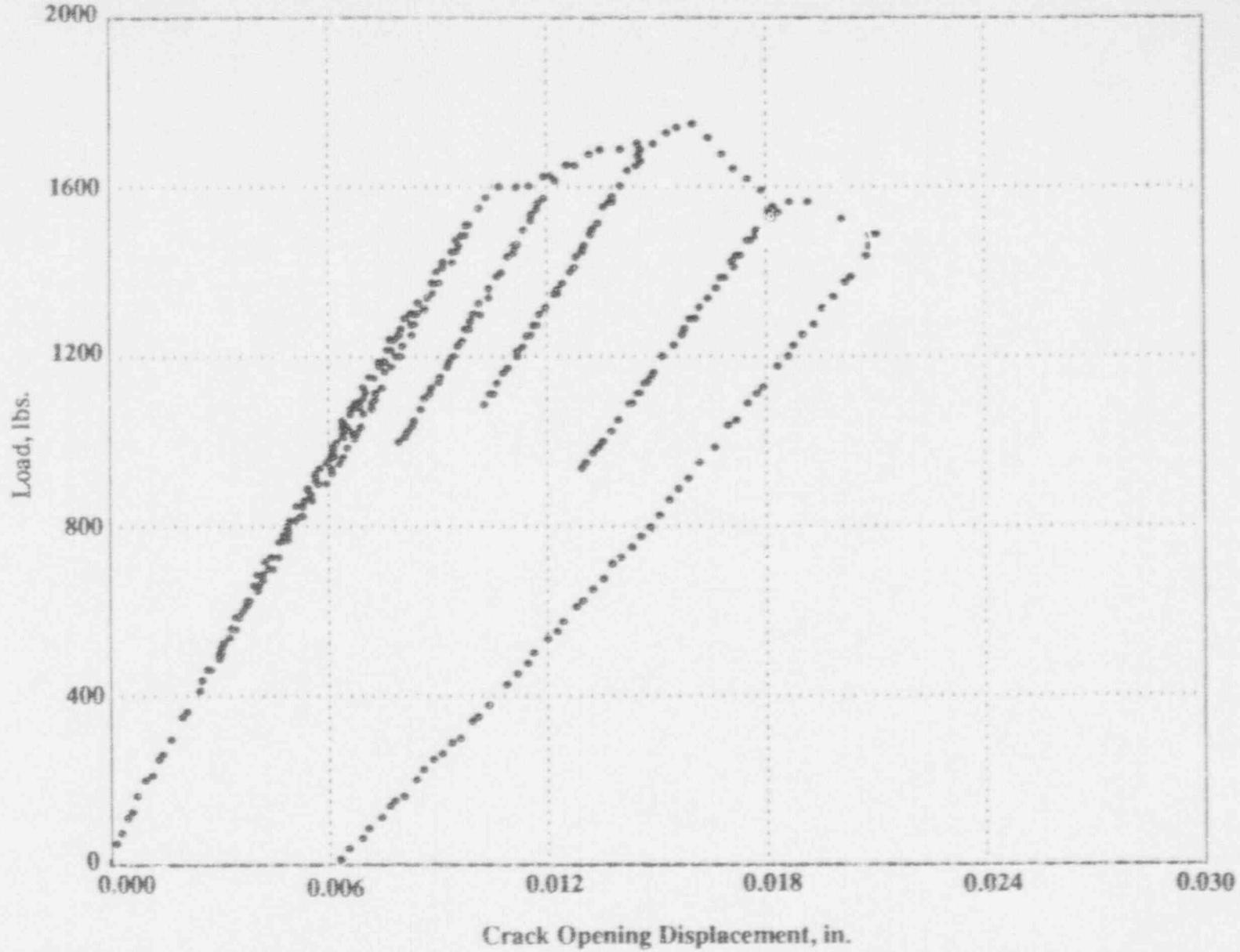

FIGURE 6-6. PERIODIC LOAD VS. DISPLACEMENT UNLOADS FOR A J_{IC} FRACTURE TOUGHNESS TEST

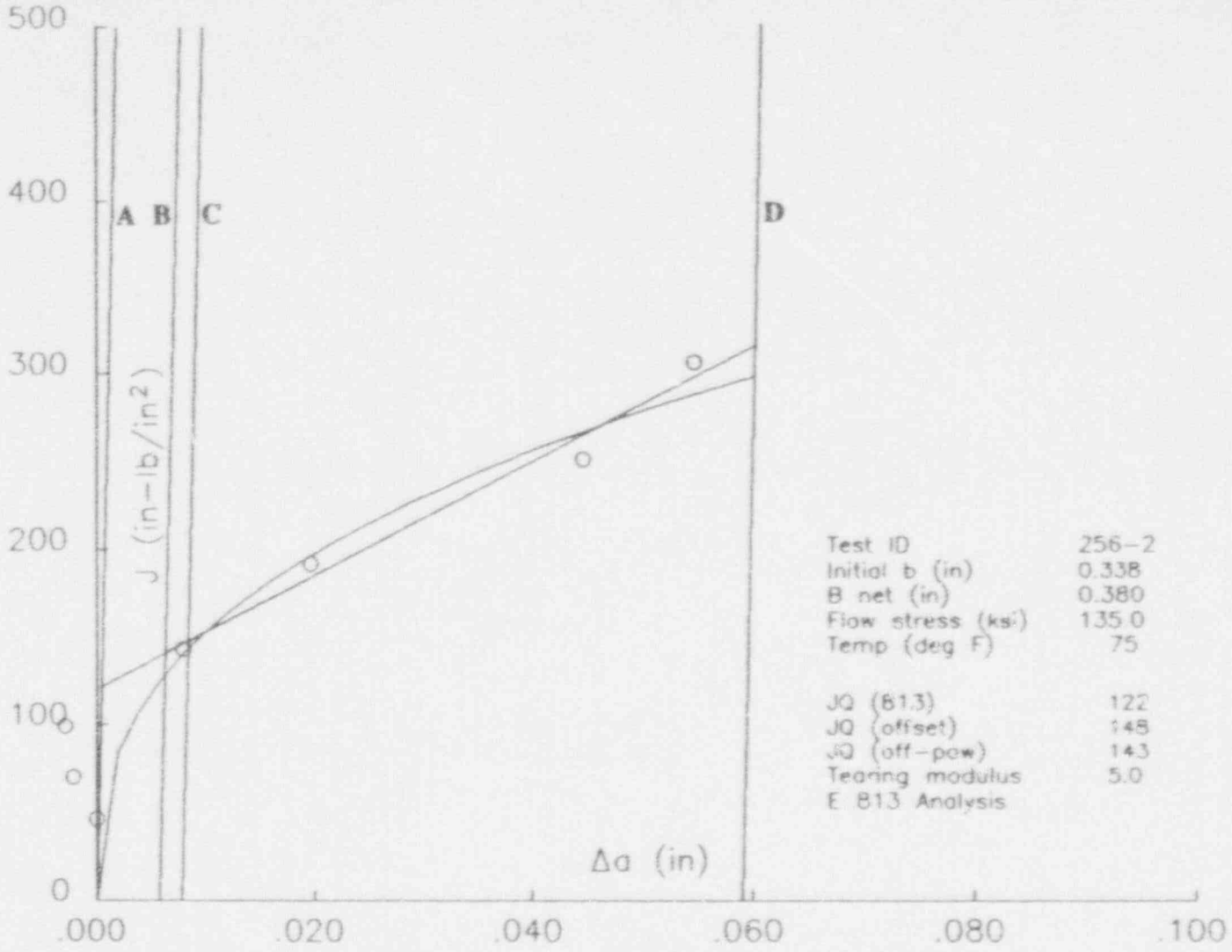

FIGURE 6-7. J-INTEGRAL AS A FUNCTION OF CRACK GROWTH FOR ANALYSIS OF A J_{IC} TEST

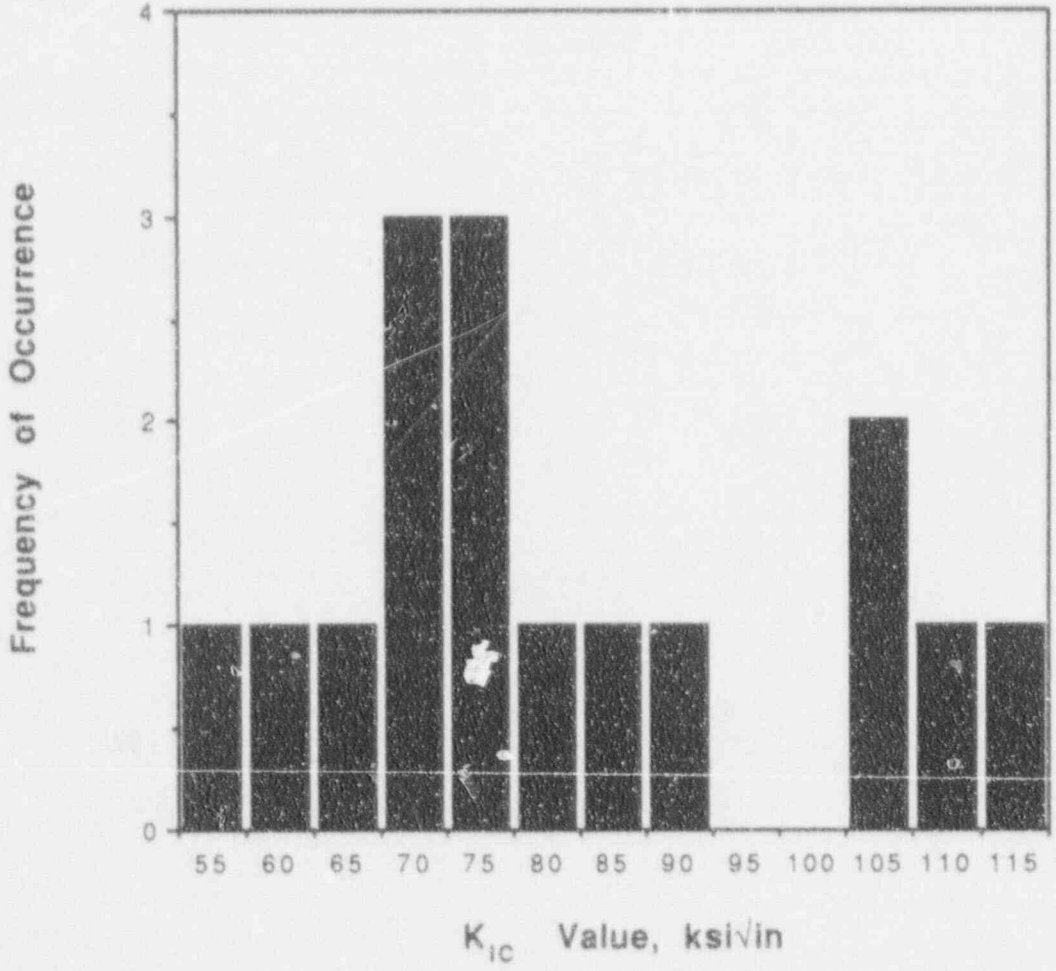

FIGURE 6-8. HISTOGRAM OF K_{IC} DATA FOR CAST 17-4PH SWING ARMS

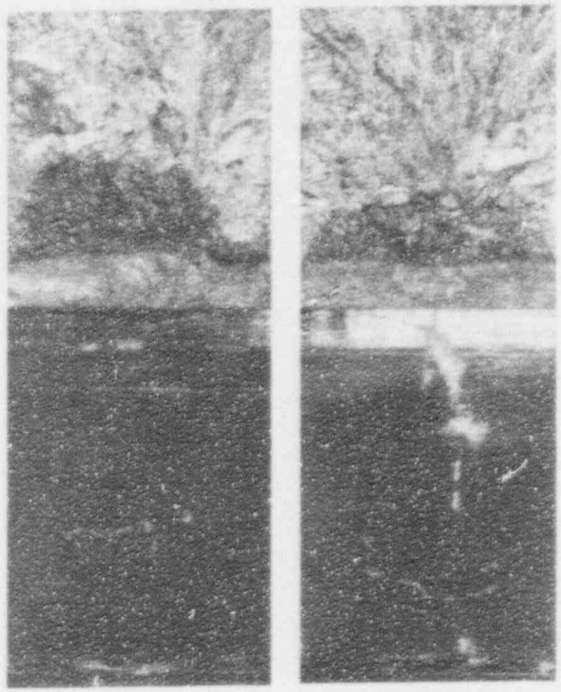

239-2 239-3

47902 2X

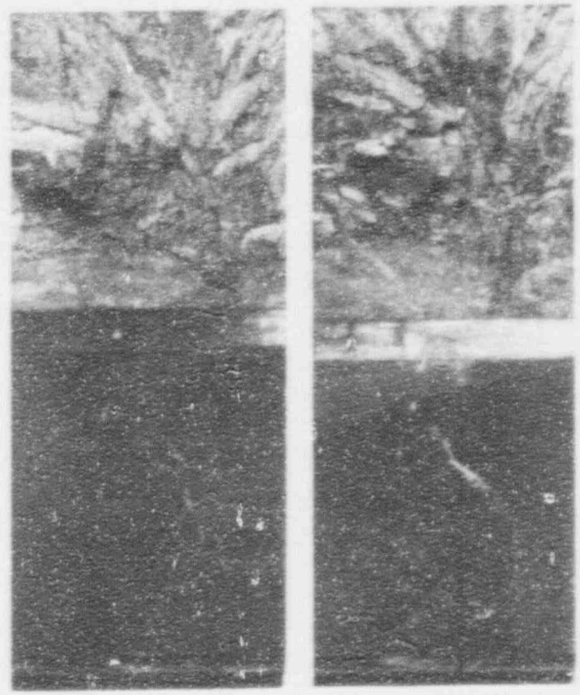

240-2 240-3

47901 2X

FIGURE 6-9. FRACTURE SURFACES OF J_{IC} SPECIMENS FROM 16-in. SWING ARMS

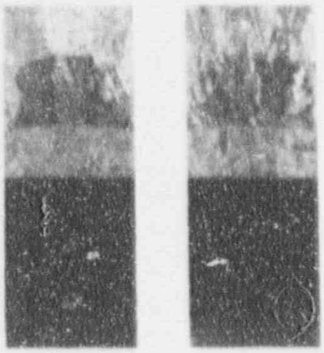

47907 2X

FIGURE 6-10. FRACTURE SURFACES OF SUB-SIZE J_{IC} SPECIMENS FROM 16-in. SWING ARMS

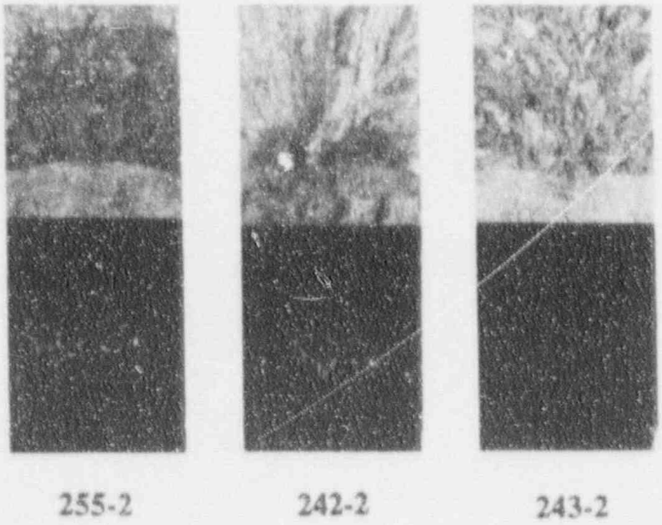

47903 2X

FIGURE 6-11. FRACTURE SURFACES OF J_{IC} SPECIMENS FROM 10-in. AND 8-in. SWING ARMS

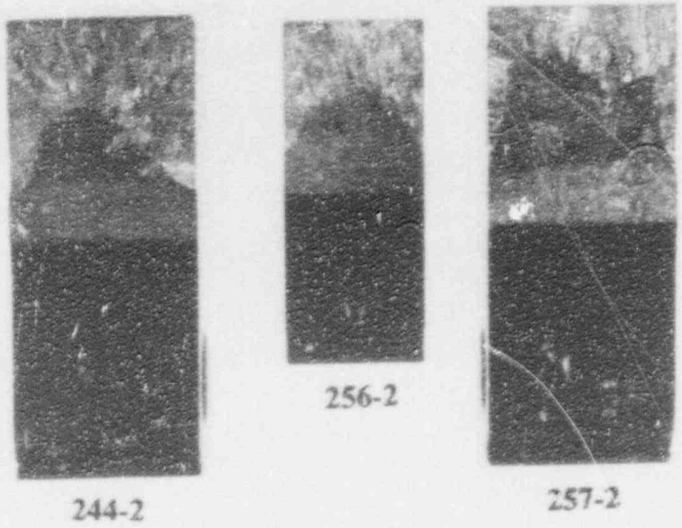

47904

2X

(a) 6-in. Swing Arms

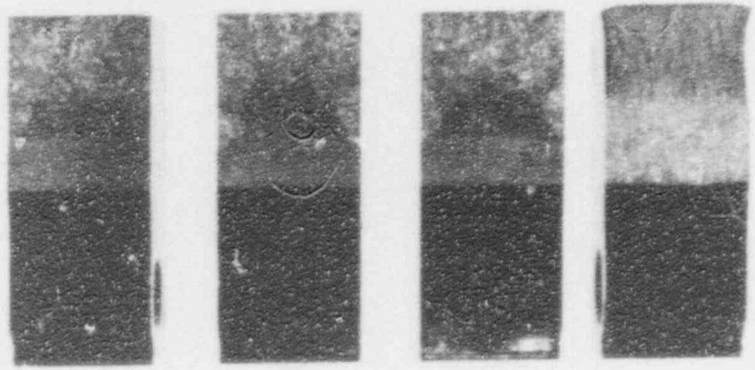

47905

2X

(b) 4-in. Swing Arms

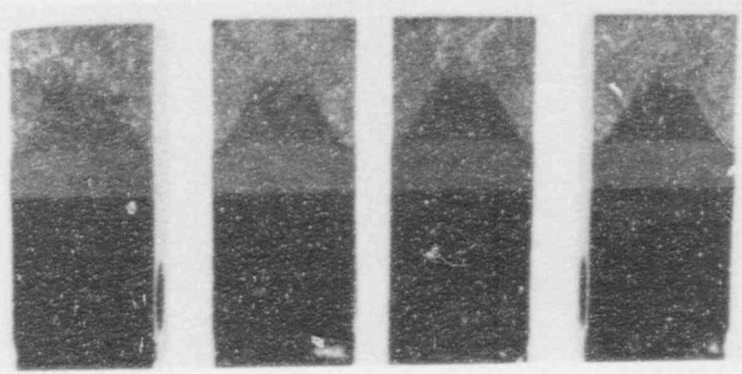

47906

2X

(c) 3-in. Swing Arms

FIGURE 6-12. FRACTURE SURFACES OF J_{IC} SPECIMENS

7.0 SUMMARY AND DISCUSSION

The observations made and the data obtained in this investigation are summarized as follows:

1) Visual and liquid penetrant inspections did not detect any significant external flaws.

2) Radiographic inspections revealed Level 6 indications of voids or inclusions at one location in the swing arm from a 10-in. valve (Sample No. 255). Isolated Level 3 indications were noted for the two arms from 16-in. valves (Nos. 239 and 240) and both of the arms from 8-in. valves (Nos. 242 and 243). The remaining twelve swing arms were either free of flaw indications or exhibited only isolated faint Level 1 and Level 2 indications.

3) Weld repairs were evident in 10 of the 16 swing arm samples. In the two 16-inch arms, weld repairs in the disk attachment boss extended through the full thickness. All others were on the order of 0.06-in. deep. Etching response of the weld deposits indicated that the repairs had been made with an austenitic stainless steel filler metal. Chemical analysis of one weld deposit identified the filler metal as Type 308 austenitic stainless steel.

4) The average hardness values for 15 of the 16 swing arms were in the range of HRC 28-40 (BHN 271-372). One sample (No. 260) exhibited an average hardness of HRC 21 (BHN 224). For comparison, ASTM A 747 specifies a minimum hardness of HRC 28 (BHN 271) for CB7Cu-1 (H1100) stainless steel (17-4PH).*

5) The properties determined in two out of four uniaxial tensile tests [No. 239 (16-in.) and No. 243 (8-in.)] met the requirements for A 747 CB7Cu-1 material (17-4PH) in the H1100 condition. In the other two tests, the yield strength for one 8-in. sample (No. 242) and the ultimate strength for one 6-in. sample (No. 244) were below the minimum of that reference specification.

6) The bulk chemical composition for 9 of the 16 arms conformed to the requirements for A 747 CBCu-1 material in every respect. Six other samples conformed to that specification except for slightly low-chromium contents (14.54-14.88% vs. 15.50% min.) or slightly high nickel contents.** The composition of one 4-in. sample (No. 260) was clearly out of range for 17-4PH stainless steel.

7) In general, the microstructural features of all but one of the swing arms were normal for cast 17-4PH stainless steel heat treated to the H1100 condition. One sample (No. 260) exhibited distinctly dendritic microstructural features indicating an inadequate solution-annealing treatment.

---

* The requirements for ASTM A 747 CB7Cu-1 (H1100) material are cited for reference only. The swing arms were not manufactured to specifically conform to that specification.

** The requirements for ASTM A 747 CB7Cu-1 (H1100) material are cited for reference only. The swing arms were not manufactured to specifically conform to that specification. AMS 5398D does not specify hardness values for the H1100 condition.

8) Multiple sectioning characterized the flaws associated with Level 2 and Level 3 radiographic indications as small shrinkage fissures (major dimension ≈ 0.2-in.) or clusters of small shrinkage voids (maximum dimensions of individual voids on the order of 0.05-in.). The flaw associated with the Level 6 radiographic indication in Sample No. 255 was found to consist of two relative large shrinkage cavities, the larger measuring 0.94-in. lg. x 0.15-in. dia.

9) Metallographic sectioning also identified a small, crack-type flaw measuring 0.93 in. lg. x 0.09-in. deep near the disk attachment boss of the swing arm from the 10-inch valve (Sample No. 255).

10) All of the flaws observed were associated with fabrication processes as opposed to being service-induced, and there was no evidence of in-service growth of any flaw.

11) The larger of the observed flaws (Level 2 and larger) were mainly confined to the 16-inch, 10-inch, and 8-inch swing arms.

12) Room temperature (≈72°F), fracture toughness tests on specimens from all 16 sample swing arms resulted in values of the critical stress intensity factor (K_{IC}) in the range of 53.7 to 115.3 ksi$\sqrt{in.}$ with a median value of 74.2 ksi$\sqrt{in.}$ and a mean value of 78.4 ksi$\sqrt{in.}$ The K_{IC} value for the one swing arm with a typical hardness, composition and microstructure (Sample No. 260) fell within the scatter band for the data from the other samples.

13) Fracture mechanics analysis was employed to evaluate the individual flaws. Based on the worst-case scenario in each instance, the calculated stress intensity values (K_I) were in the range of 18.6 to 31.1 ksi$\sqrt{in.}$

14) Statistical analysis of the fracture toughness test results indicated that for a 95% confidence interval, the lower bound of fracture toughness (K_{IC}) for 95% of the 56 swing arms remaining in service is 44 ksi$\sqrt{in.}$

15) Duplicate fracture toughness tests on the 16-in. swing arms conducted at 40°F resulted in K_{IC} values well within the scatter band of all of the room temperature K_{IC} data.

16) Duplicate fracture toughness tests on the 16-in. arms, employing both the standard size test specimens and the sub-size specimens, established that the sub-size specimens produced reliable K_{IC} values.

In general, all but one of the swing arm samples included in this investigation were free of gross defects and all but one exhibited compositions, microstructures, and hardness values comparable to the requirements of ASTM A 747, the current specification for cast 17-4PH (H1100) material [A 747 CB7Cu-1 (H1100)]. Only one sample, a 4-inch swing arm was found to deviate significantly from the typical composition and hardness of cast 17-4PH (H1100) stainless steel. In this case, the composition clearly did not meet the requirements for 17-4PH and the hardness was

significantly below that of the other 15 samples. This particular sample also exhibited an abnormal microstructure, indicating improper heat treatment. Six samples deviated slightly from the compositional requirements of the reference specifications but the hardness for each of these was above the specified minimum. All remaining samples conformed to the compositional and hardness requirements for CB7Cu-1 (H1100) material in every respect.

Weld repairs had been made to ten of the sixteen sample swing arms and, in each case, the repairs had been made with an austenitic filler metal rather than one with a composition matching that of 17-4PH stainless steel. However, most of the weld repairs were shallow and cosmetic in nature and no welding-induced flaws were noted, even for two cases with through-thickness repairs.

In the performance of the fracture toughness tests, complete conformance to all of the validity checks of the governing ASTM specifications was not accomplished. However, the validity requirements in question are strict test specifications and nonconformance does not necessarily indicate invalid data. In those cases which did not strictly conform, the character of the fracture, and the general nature of crack extension data was typical for valid fracture toughness tests. Overall, the progress of the tests and character of the fractured specimens indicate that the data obtained is reliable and adequate for use in design analyses.

Radiographic inspection and subsequent metallographic sectioning identified a few distinct flaws in the larger swing arms. In general, these were relatively small and, except for one case, were embedded within the cross section of the arm. One flaw was identified as shrinkage cavity with dimensions on the order of 0.1-in. x 0.9-in. All other cases consisted of small fissures or clusters of shrinkage voids. One case was a surface-connected fissure with dimensions on the order of 0.9-in. long x 0.09-in. deep. The remaining flaws examined were all embedded and had major dimensions on the order of 0.7-in. x 0.1-in.

The significance of the observed flaws was evaluated by linear elastic fracture mechanics (LEFM). The evaluation of each flaw was based on a worst-case scenario. For the LEFM analysis, all flaws were assumed to be tight, sharp, surface-connected cracks with dimensions to envelope each complete flaw zone. In addition, the flaws were considered to be oriented transverse to the

long axis of the swing arm and located at the point of maximum bending stress. With these very conservative assumptions, and for a bending stress of 60 ksi, the range of stress intensity factors (K_I) associated with the flaws is 18 to 31 ksi$\sqrt{in}$. These values are well below the range of K_{IC} values determined by the fracture toughness tests.

The general trends of the dependency of critical fracture stress on crack size, crack shape and inherent fracture toughness are illustrated in Figures 5-21 and 5-22. Figure 5-21 demonstrates that, for the complete range of crack geometries observed in the group of samples and for a toughness level of K_{IC} = 50 ksi$\sqrt{in}$, a transversely-oriented flaw would require a through-thickness dimension on the order of 0.4t before failure could occur at an operating stress of 60 ksi. A second view of the significance of flaw size is presented in Figure 5-22. Here, it can be seen that, for a flaw of typical geometry with a depth of 0.25t, the inherent toughness of the arm material would have to be 40 ksi$\sqrt{in}$ or less before fracture at an operating stress of 60 ksi would be likely.

In the tests and examinations performed in this program, the largest flaw depth noted was approximately 0.1t and the lower value of K_{IC} measured was 53 ksi$\sqrt{in}$. Again, it should be noted that all conditions assumed in the LEFM analyses were very conservative.

8.0 REFERENCES

1. Aerospace Material Specification 5398D, Steel Castings, Sand and Centrifugal, Corrosion Resistant, 16Cr4.1Ni0.22 (Cb+Ta) 2.8 Cu.

2. Military Specification MIL-H-6875, Process for Heat Treatment of Steel.

3. ASTM A 747, Standard Specification for Steel Castings, Stainless, Precipitation Hardening.

4. Newman, J. C., Jr., and Raju, I. S., "An Empirical Stress-Intensity Factor Equation for the Surface Crack," *Engineering Fracture Mechanics*, Vol. 15, No. 1-2, pp. 185-192 (1981).

5. ASTM Standard E 399-83. "Standard Test Method for Plane-Strain Fracture Toughness of Metallic Materials," **Annual Book of ASTM Standards**, Vol. 3.01.

6. ASTM Standard E 813-88. "Standard Test Method for J_{IC}, A Measure of Fracture Toughness," **Annual Book of ASTM Standards**, Vol. 3.01.

7. Saxena, A., and Hudak, S. J., "Review and Extension of Compliance Information for Common Crack Growth Specimens," *International Journal of Fracture*, Vol. 15, No. 5, pp. 453-468 (1978).

8. ASTM Standard E 446-81, "Reference Radiographs for Steel Castings up to 2-in. Thick," **Annual Book of ASTM Standards,** Vol. 1.02.

APPENDIX A

SWING ARM CONFIGURATIONS

16-inch, Sample Nos. 239 and 240:	Figures A-1 and A-2
10-inch, Sample No. 255:	Figure A-3
8-inch, Sample Nos. 242 and 243:	Figures A-4 and A-5
6-inch, Sample Nos. 244, 256, and 257:	Figures A-6, A-7, and A-8
4-inch, Sample Nos. 245, 258, 259, and 260:	Figures A-9, A-10, A-11, and A-12
3-inch, Sample Nos. 246, 261, 262, and 263:	Figures A-13, A-14, A-15, and A-16

45434

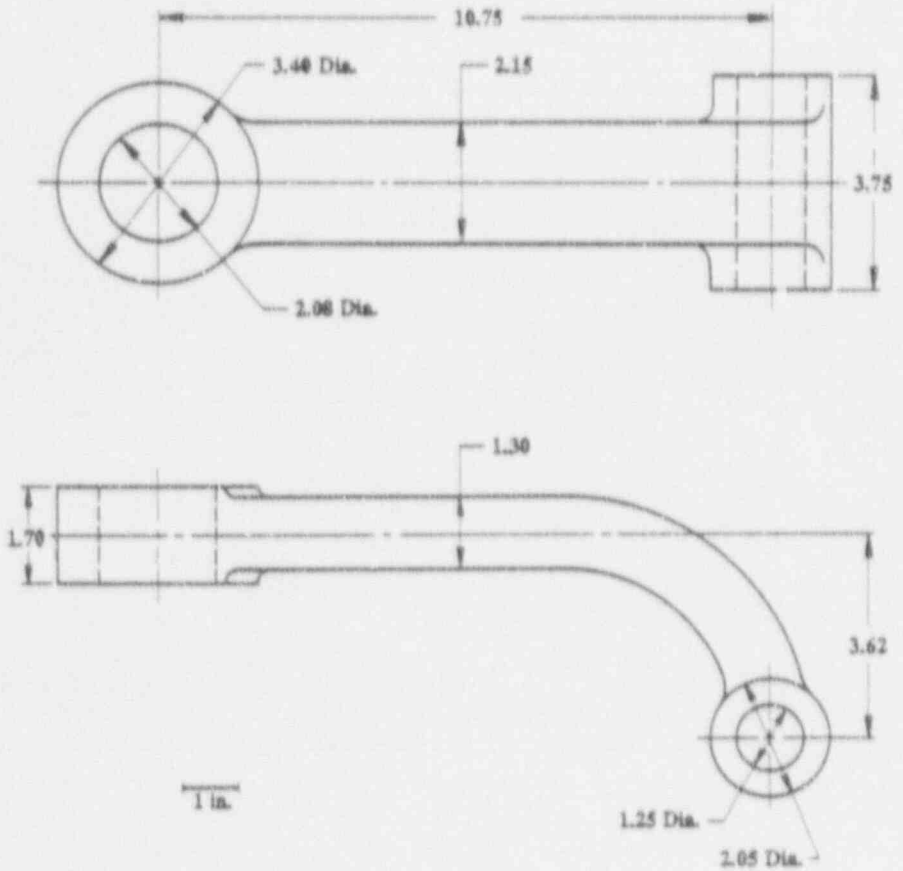

FIGURE A-1. SAMPLE NO. 239, 16-INCH CHECK VALVE.
Dimensions in inches. Diagram is schematic.

45433

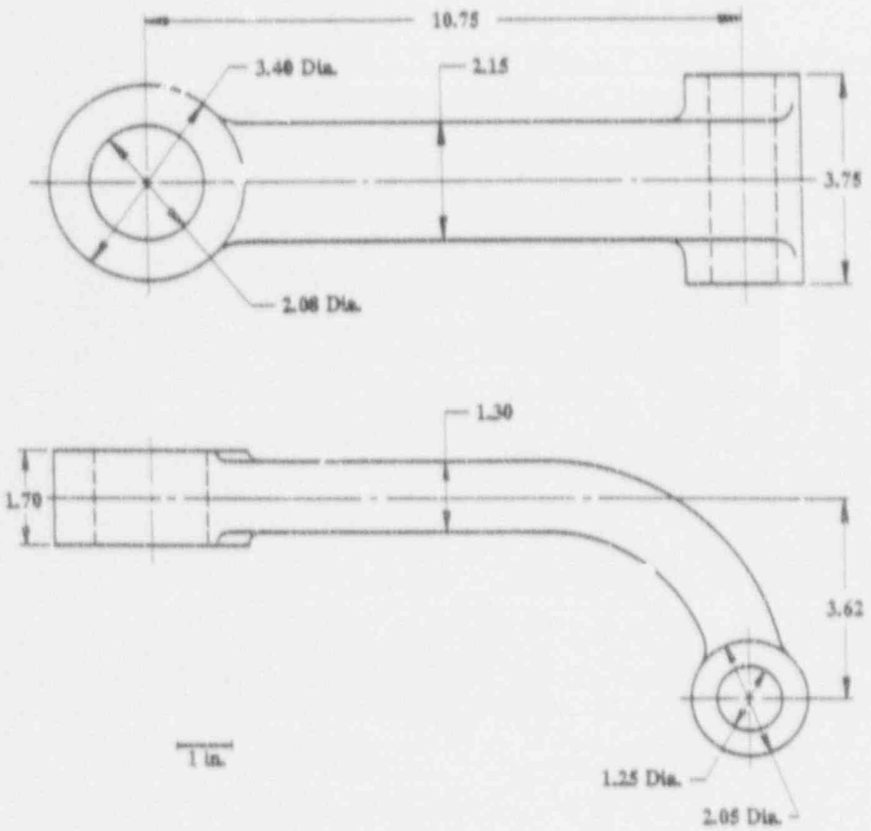

FIGURE A-2. SAMPLE NO. 240, 16-INCH CHECK VALVE.
Dimensions in inches. Diagram is schematic.

46475

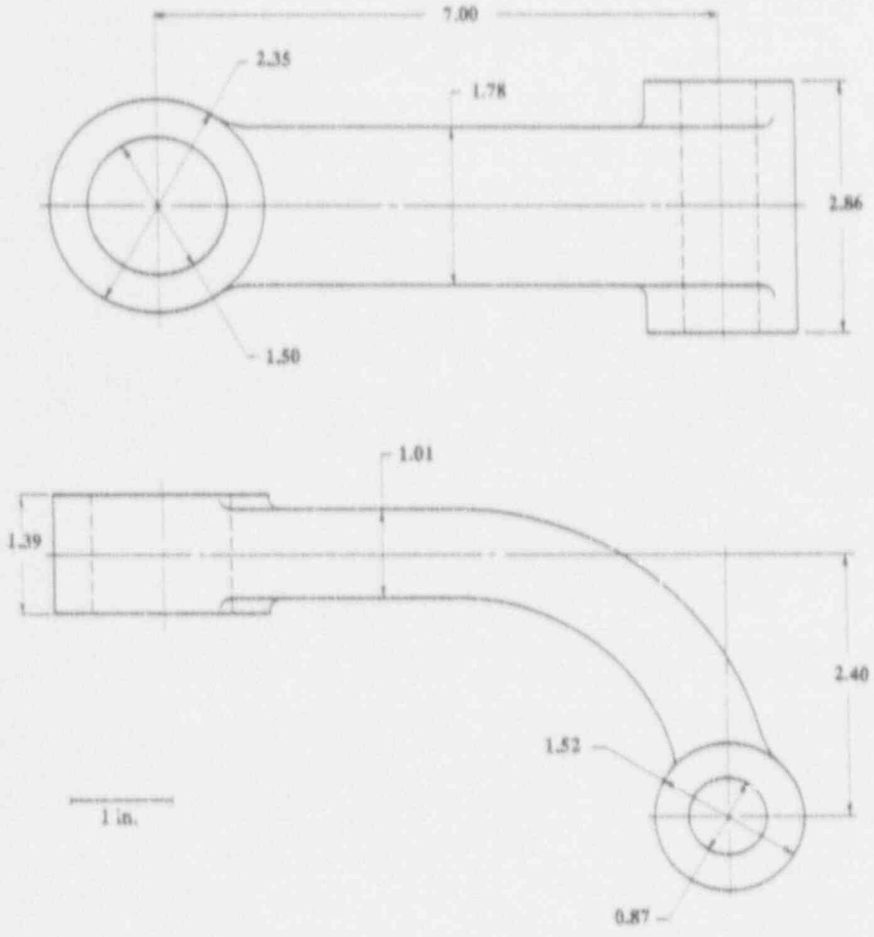

FIGURE A-3. SAMPLE NO. 255, 10-INCH CHECK VALVE.
Dimensions in inches. Diagram is schematic.

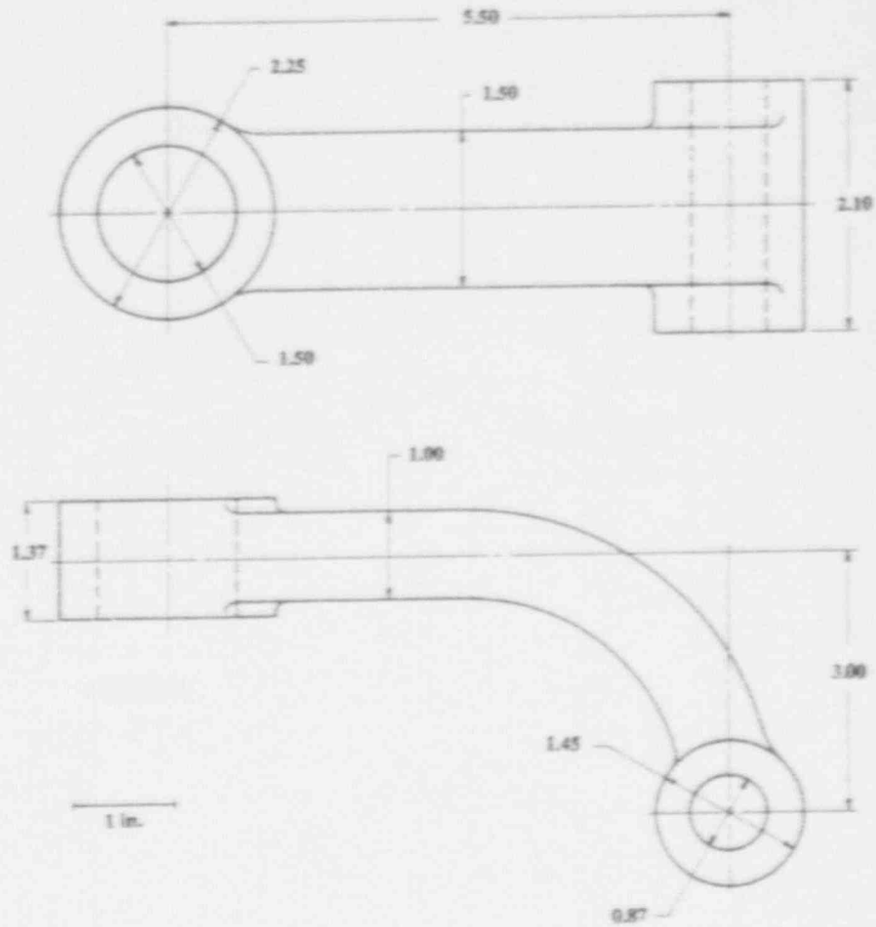

45815

FIGURE A-4. SAMPLE NO. 242, 8-INCH CHECK VALVE. Dimensions in inches. Diagram is schematic.

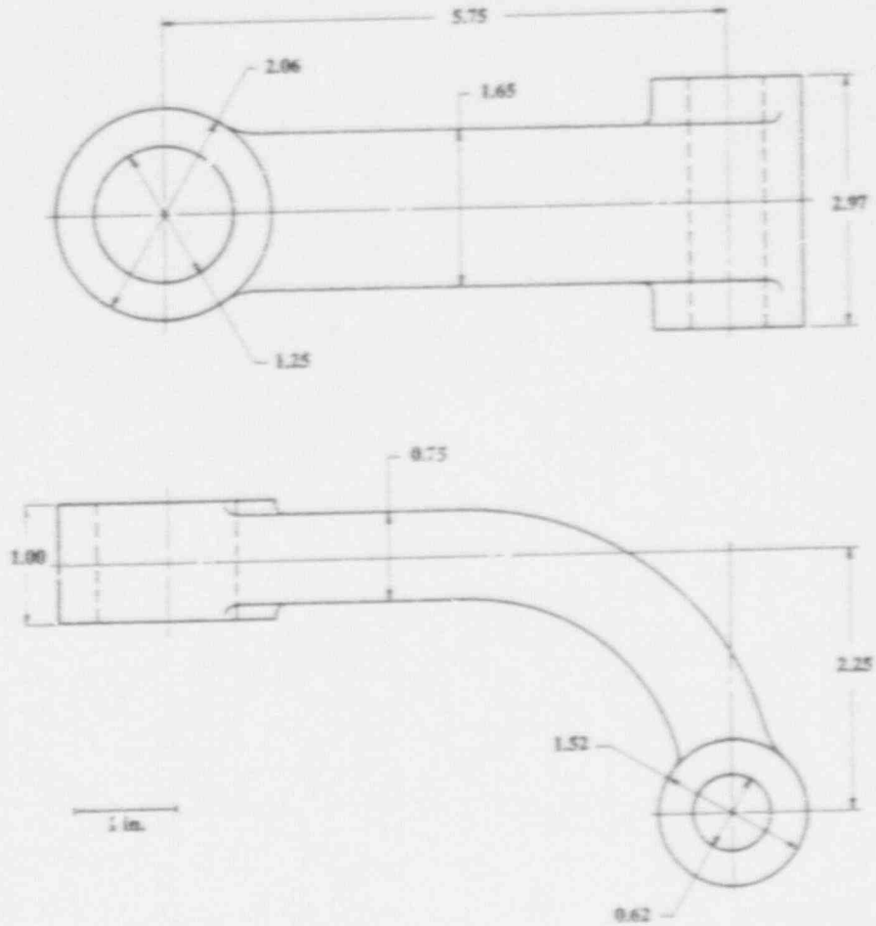

45816

FIGURE A-5. SAMPLE NO. 243, 8-INCH CHECK VALVE. Dimensions in inches. Diagram is schematic.

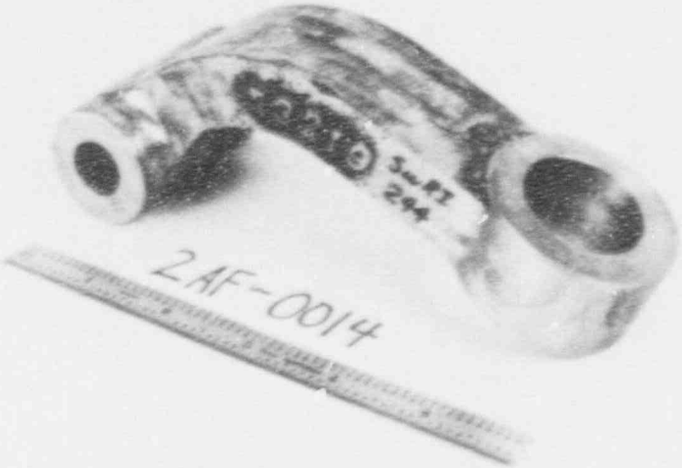

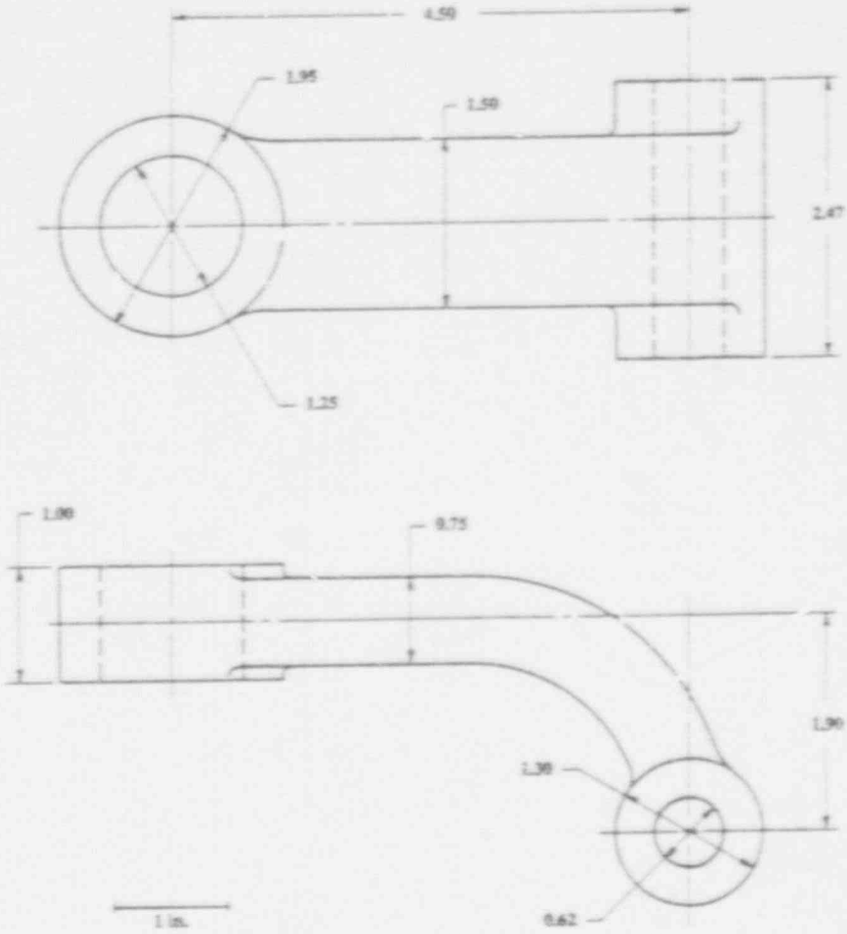

45735

FIGURE A-6. SAMPLE NO. 244, 6-INCH CHECK VALVE. Dimensions in inches. Diagram is schematic.

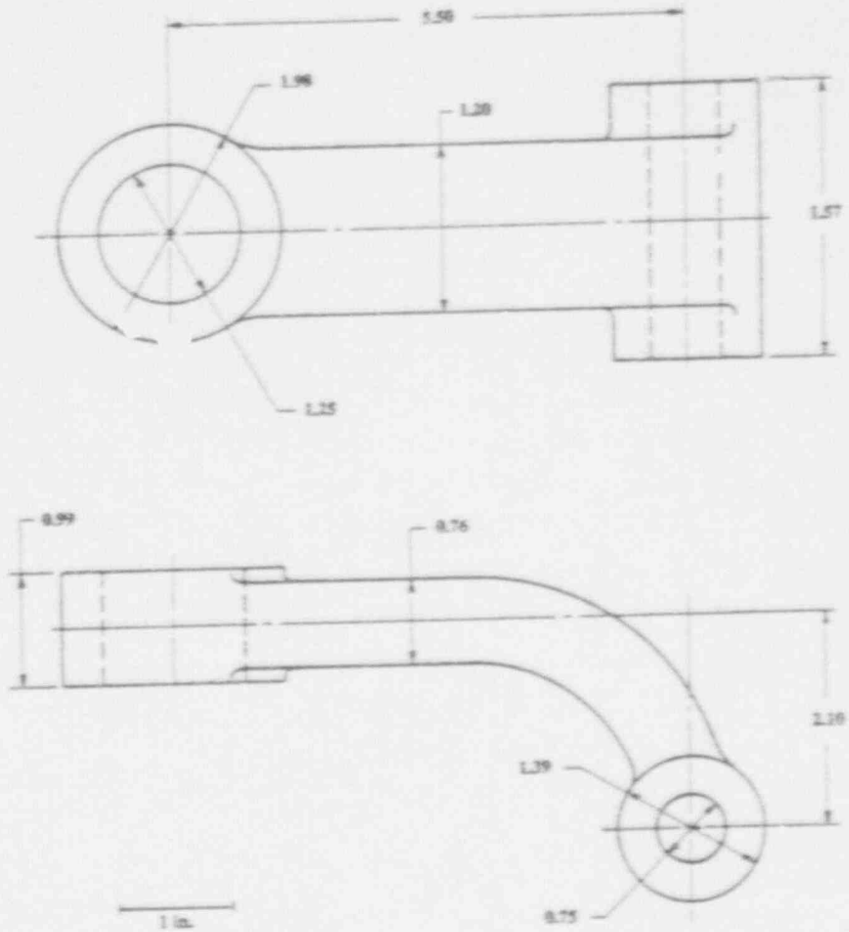

46474

FIGURE A-7. SAMPLE NO. 256, 6-INCH CHECK VALVE. Dimensions in inches. Diagram is schematic.

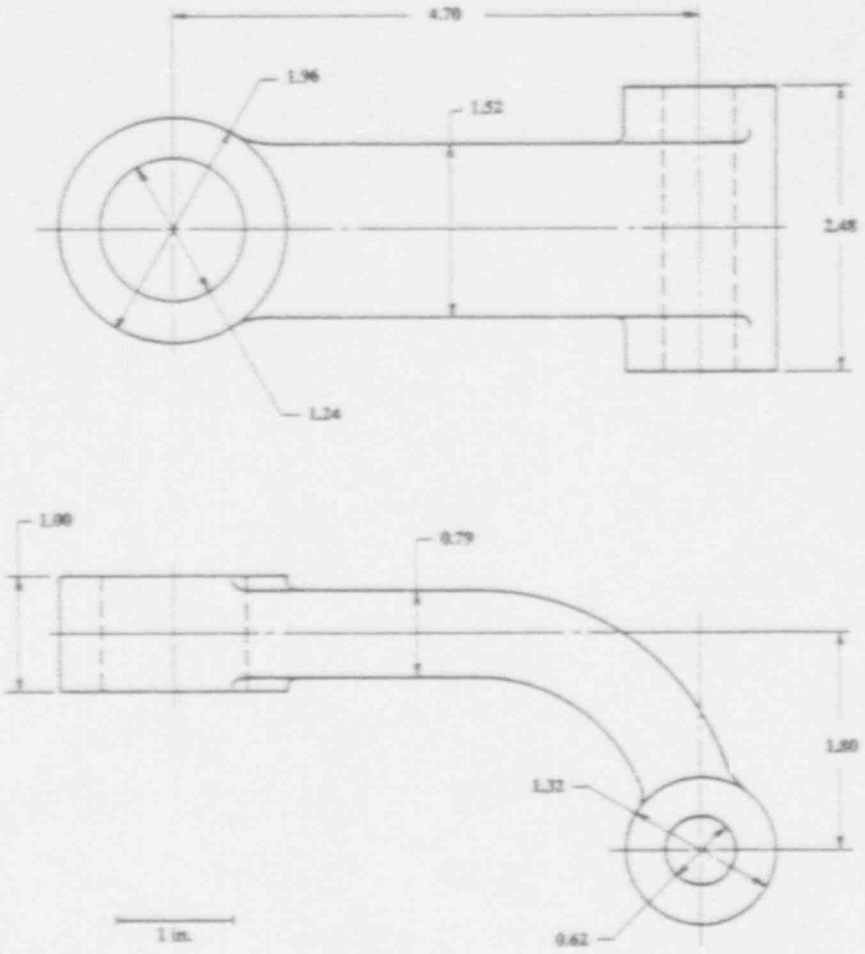

46473

FIGURE A-8. SAMPLE NO. 257, 6-INCH CHECK VALVE. Dimensions in inches. Diagram is schematic.

45736

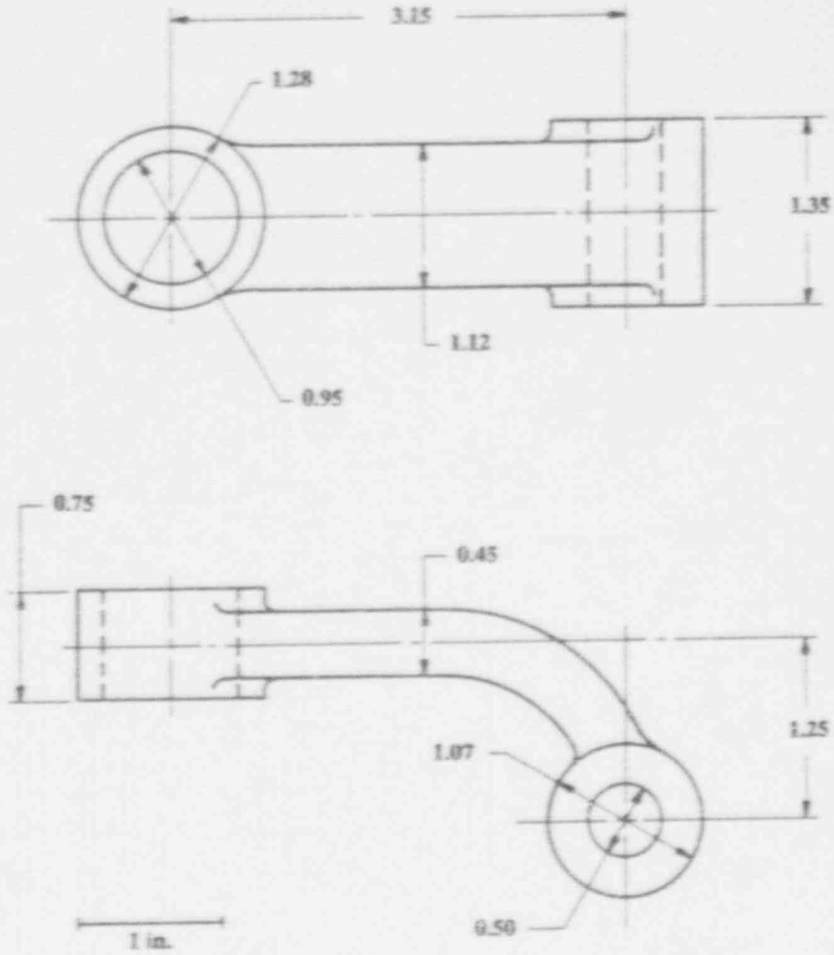

FIGURE A-9. SAMPLE NO. 245, 4-INCH CHECK VALVE. Dimensions in inches. Diagram is schematic.

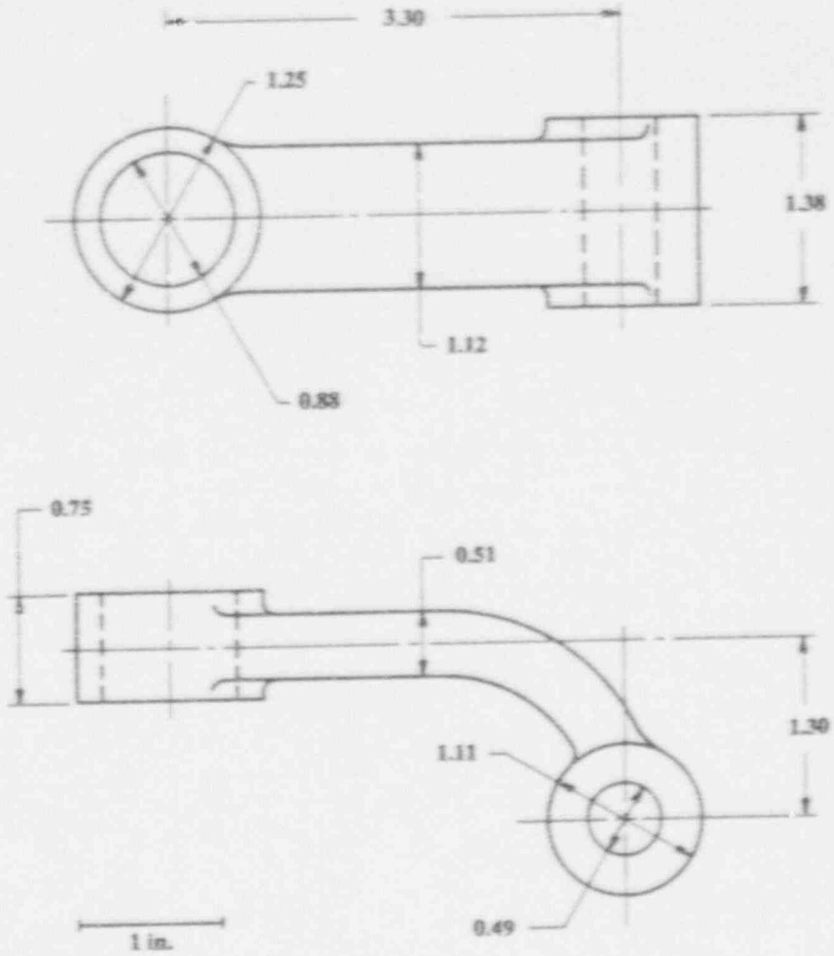

46525

FIGURE A-10. SAMPLE NO. 258, 4-INCH CHECK VALVE. Dimensions in inches. Diagram is schematic.

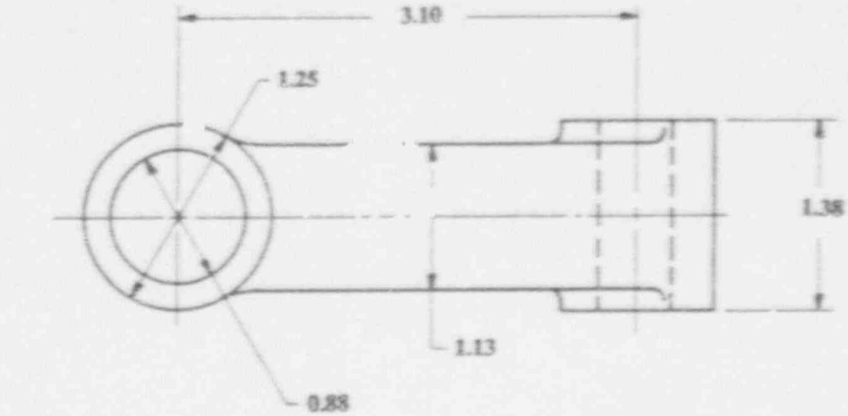

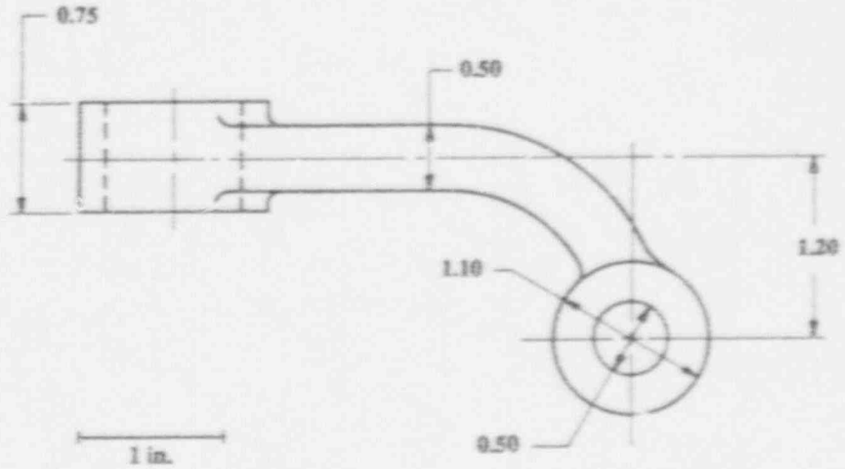

46476

FIGURE A-11. SAMPLE NO. 259, 4-INCH CHECK VALVE. Dimensions in inches. Diagram is schematic.

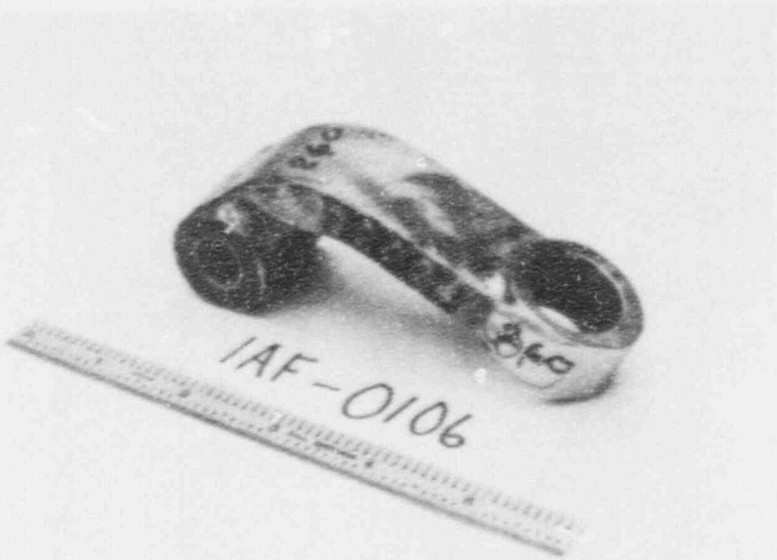

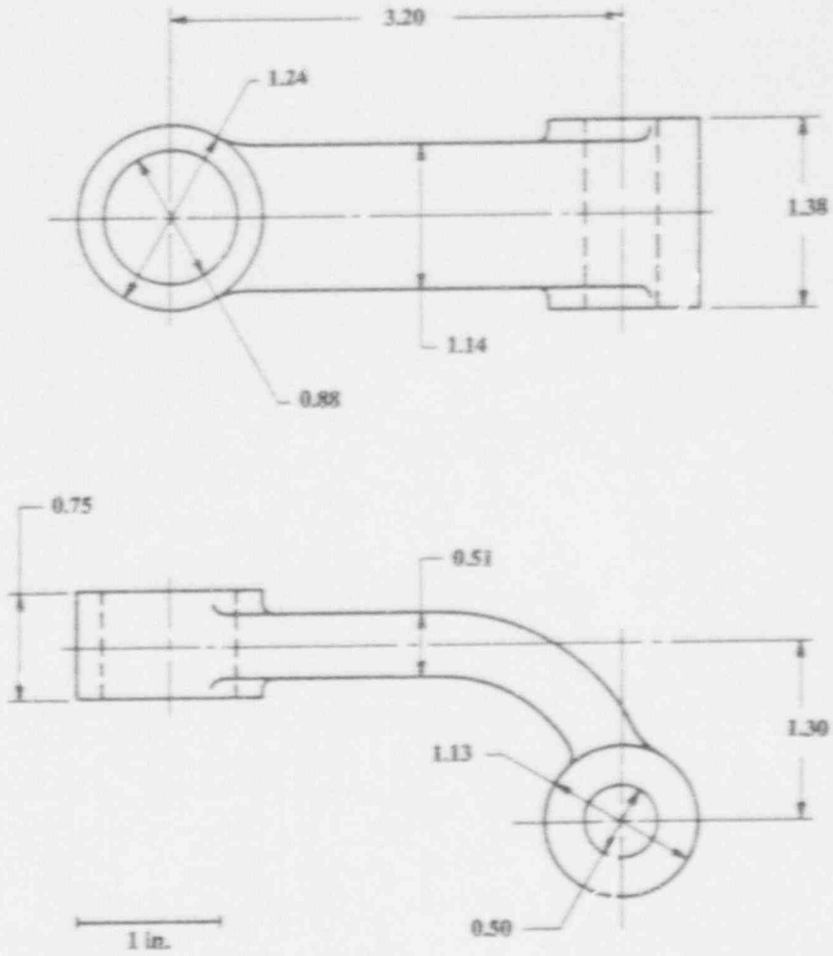

46524

FIGURE A-12. SAMPLE NO. 260, 4-INCH CHECK VALVE. Dimensions in inches. Diagram is schematic.

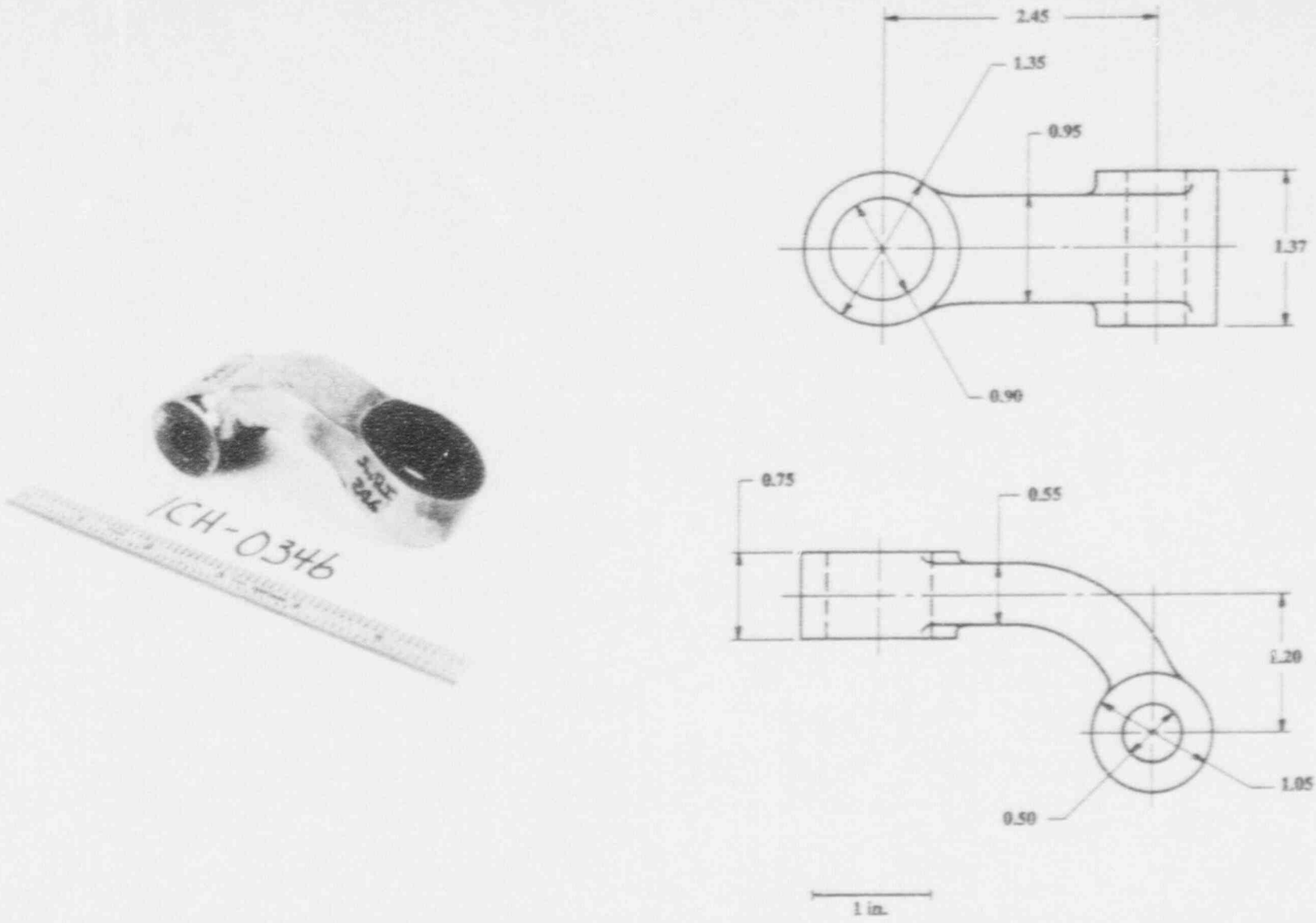

FIGURE A-13. SAMPLE NO. 246, 3-INCH CHECK VALVE. Dimensions in inches. Diagram is schematic.

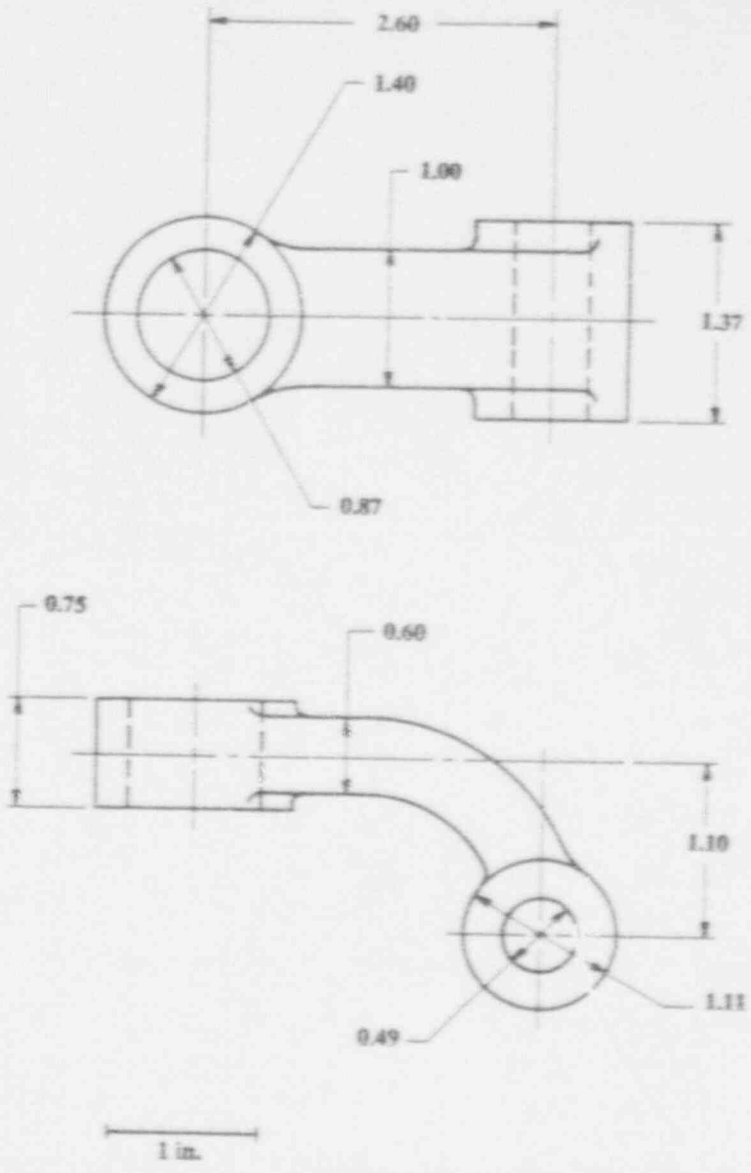

46528

FIGURE A-14. SAMPLE NO. 261, 3-INCH CHECK VALVE. Dimensions in inches. Diagram is schematic.

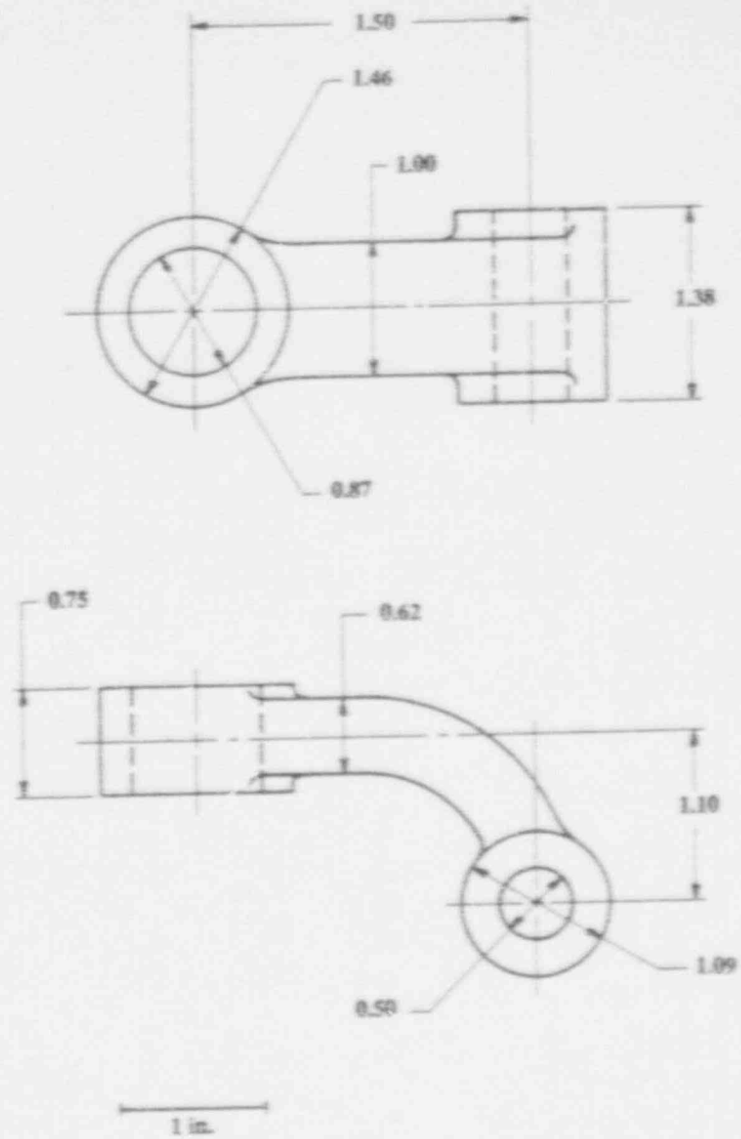

46526

FIGURE A-15. SAMPLE NO. 262, 3-INCH CHECK VALVE. Dimensions in inches. Diagram is schematic.

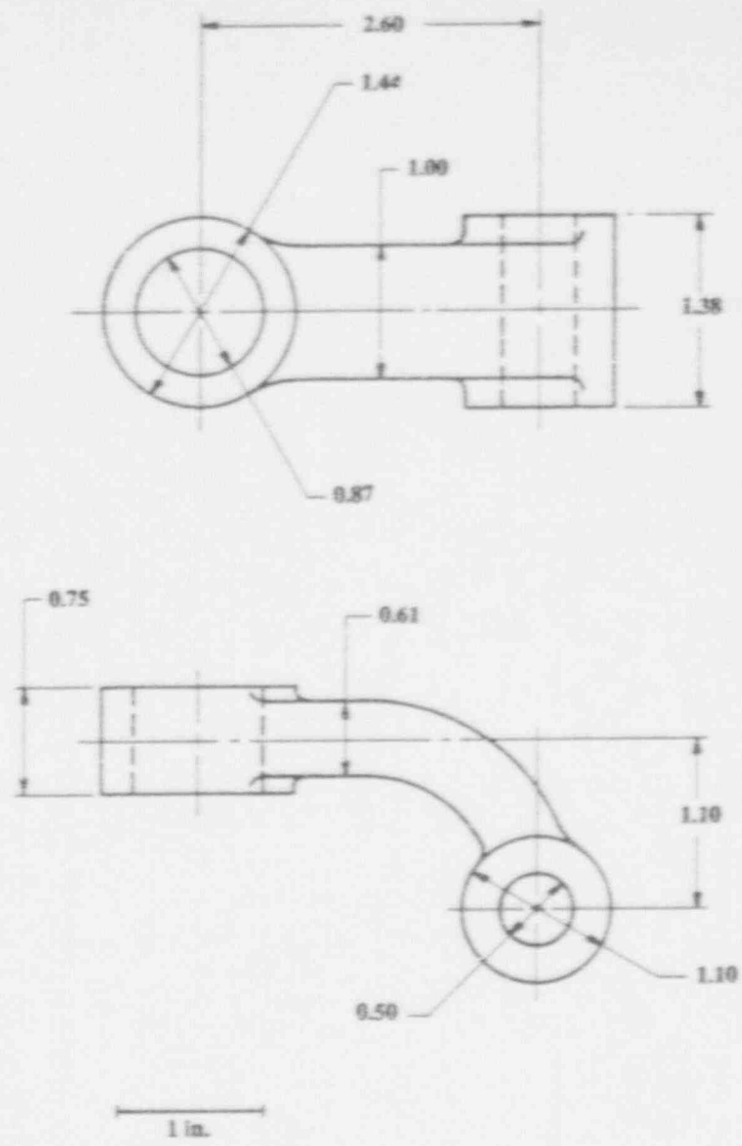

46527

FIGURE A-16. SAMPLE NO. 263, 3-INCH CHECK VALVE. Dimensions in inches. Diagram is schematic.

APPENDIX B

MICROSTRUCTURE OF SWING ARMS

16-inch, Sample Nos. 239 and 240:	Figures B-1 and B-2
10-inch, Sample No. 255:	Figure B-3
8-inch, Sample Nos. 242 and 243:	Figures B-4, B-5, and B-6
6-inch, Sample Nos. 244, 256, and 257:	Figures B-7 through B-10
4-inch, Sample Nos. 245, 258, 259, and 260:	Figures B-11 through B-14
3-inch, Sample Nos. 246, 261, 262, and 263:	Figures B-15 through B-18

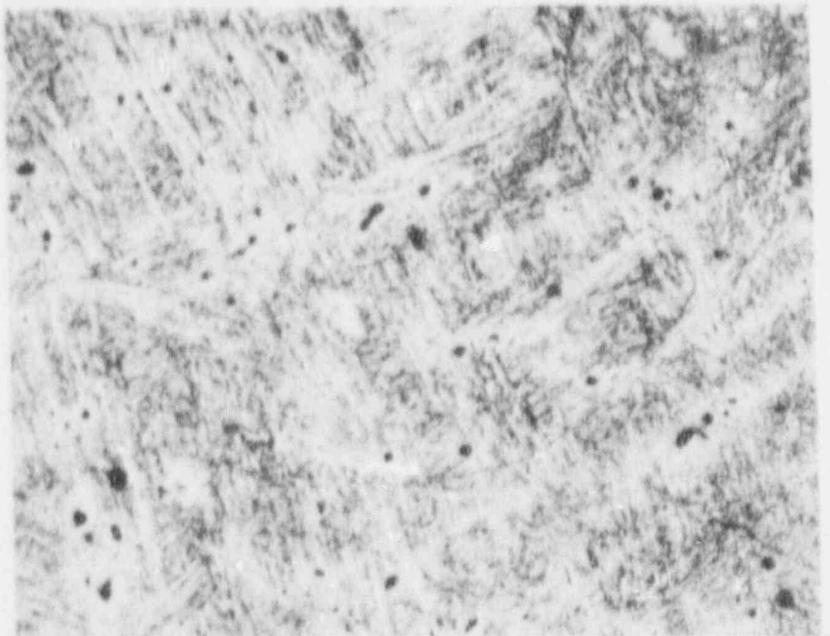

46523 200X

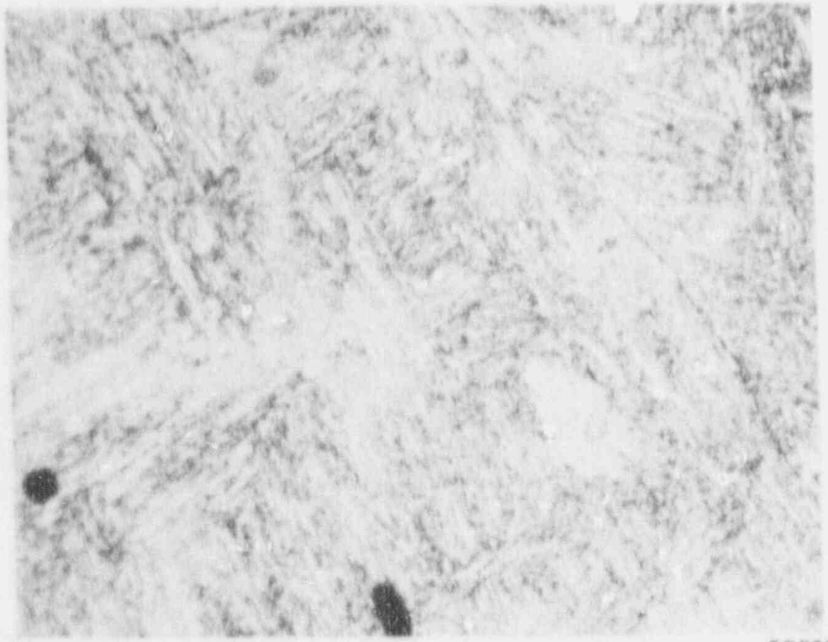

46590 500X

FIGURE B-1. TYPICAL MICROSTRUCTURE OF SAMPLE No. 239 (16-in.). Etchant: Fry's reagent.

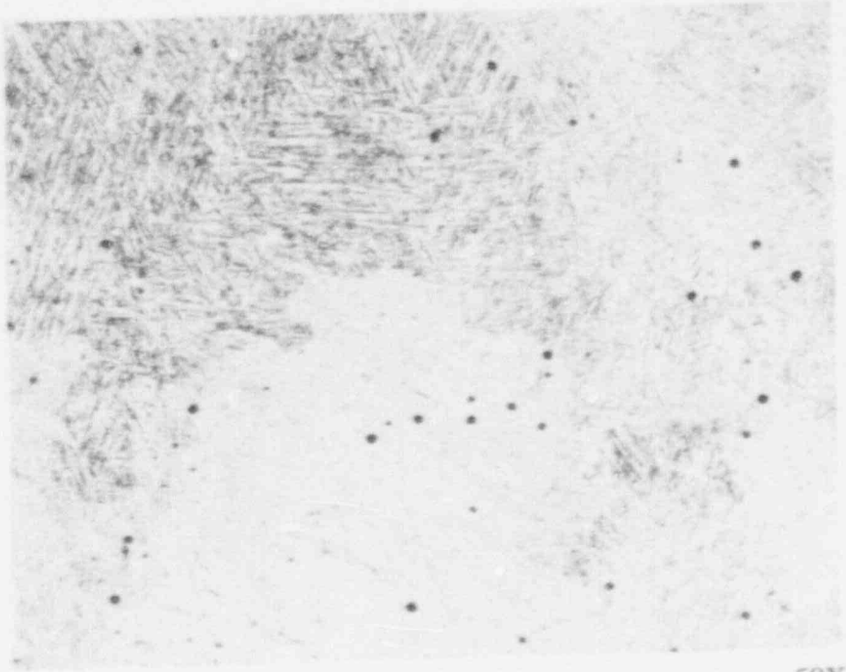

47816 (a) 50X

47819 (b) 200X

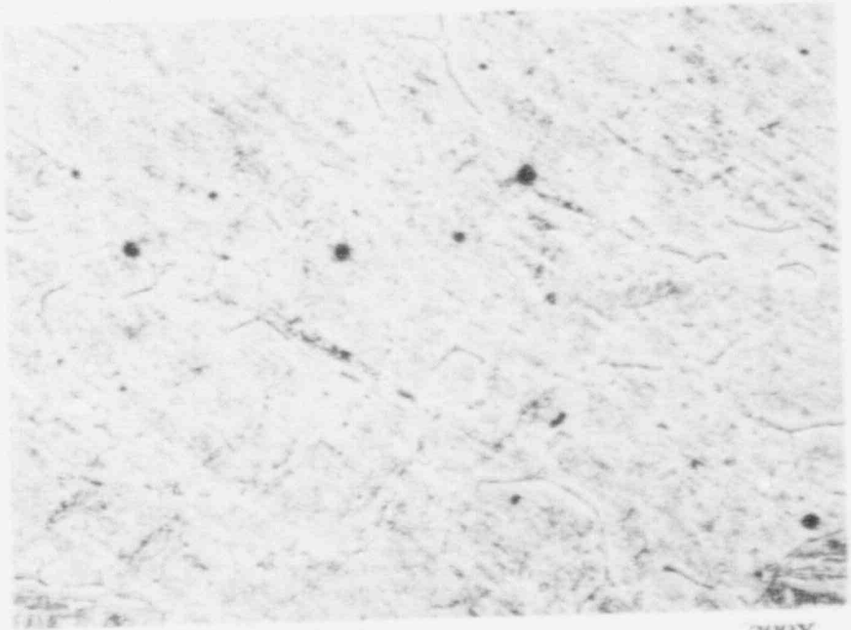

47818 (c) 200X

FIGURE B-2. MICROSTRUCTURE OF SAMPLE NO. 240 (16-in.). Etchant: Vilella's reagent

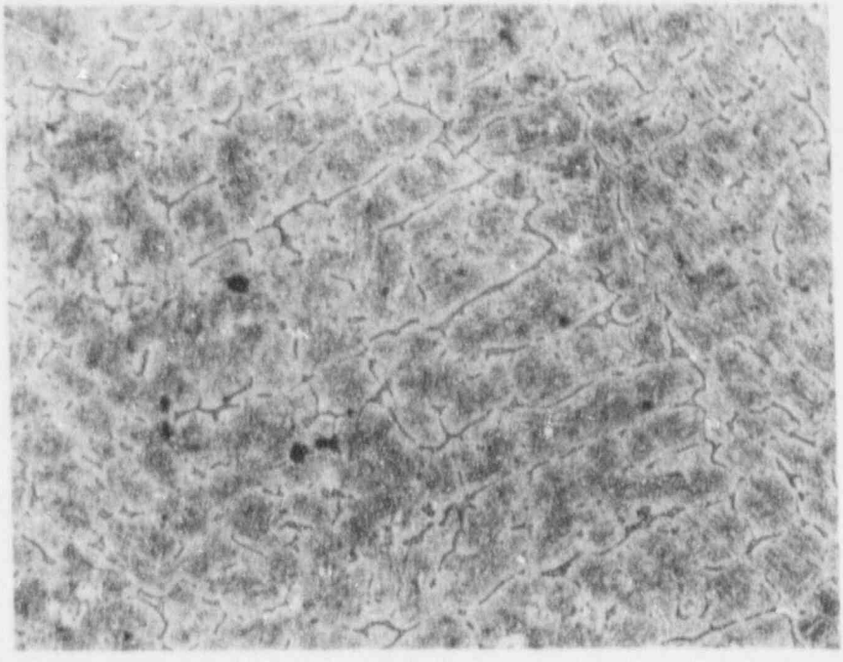

47230 100X

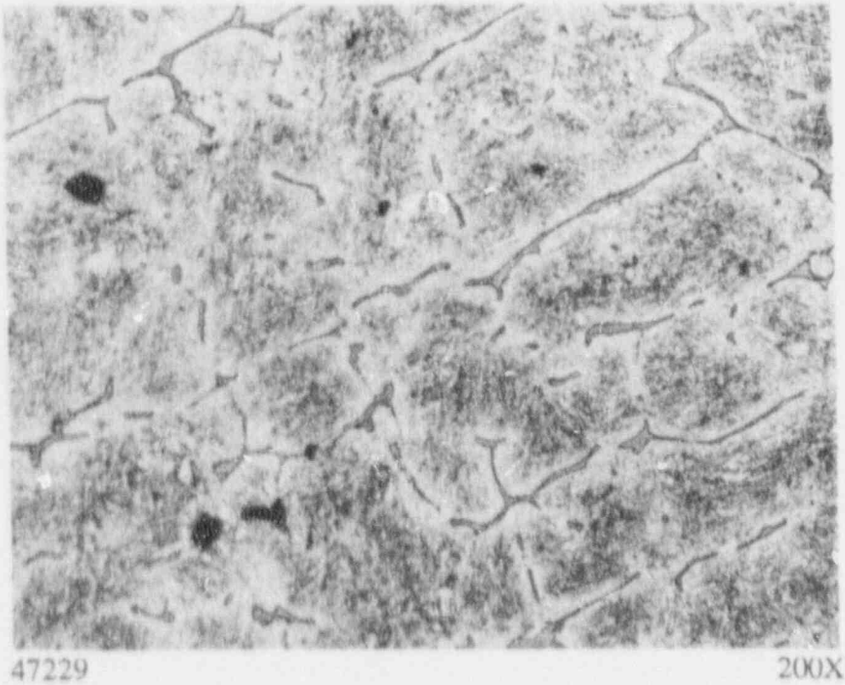

47229 200X

FIGURE B-3. TYPICAL MICROSTRUCTURE OF SAMPLE NO. 255 (10-in.). Etchant: Vilella's reagent

47188 100X

47187

FIGURE B-4. TYPICAL MICROSTRUCTURE OF SAMPLE NO. 242 (8-in.). Section B-B. (See Figure B-5). Etchant: Vilella's reagent

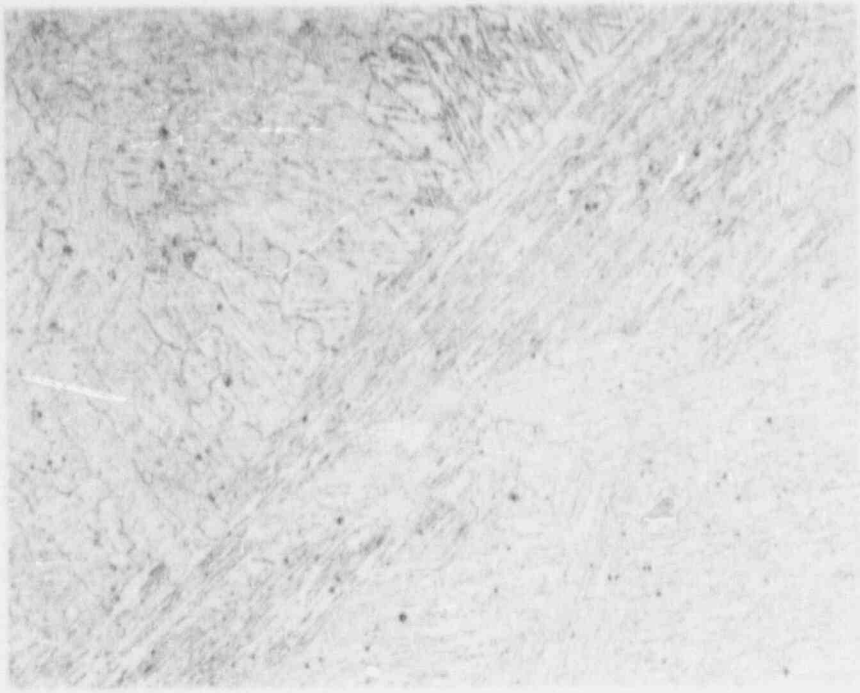

47192 100X

(a)

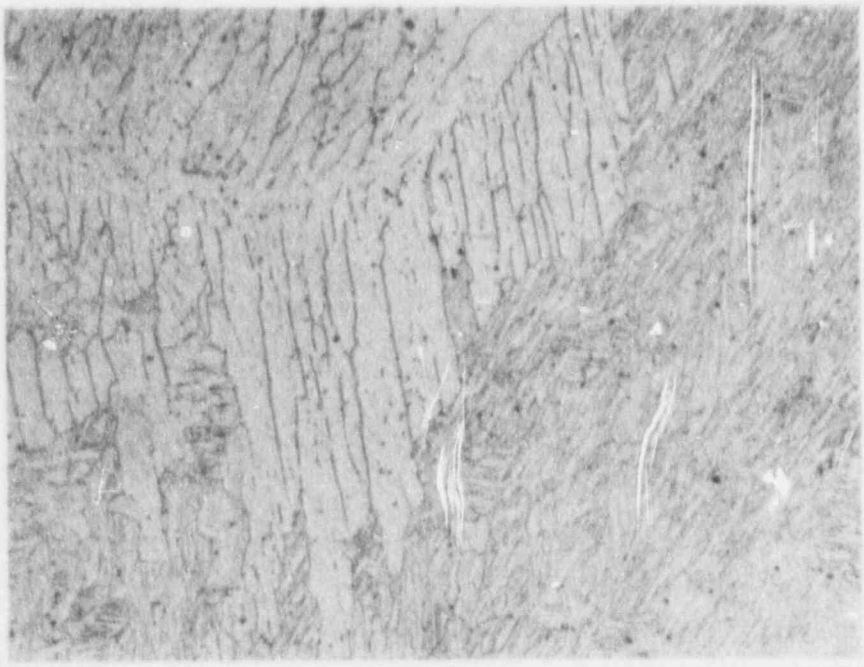

47190 100X

(b)

FIGURE B-5. MICROSTRUCTURE OF SAMPLE NO. 242 (8-in.).
See Figure B-4. Etchant: Vilella's reagent

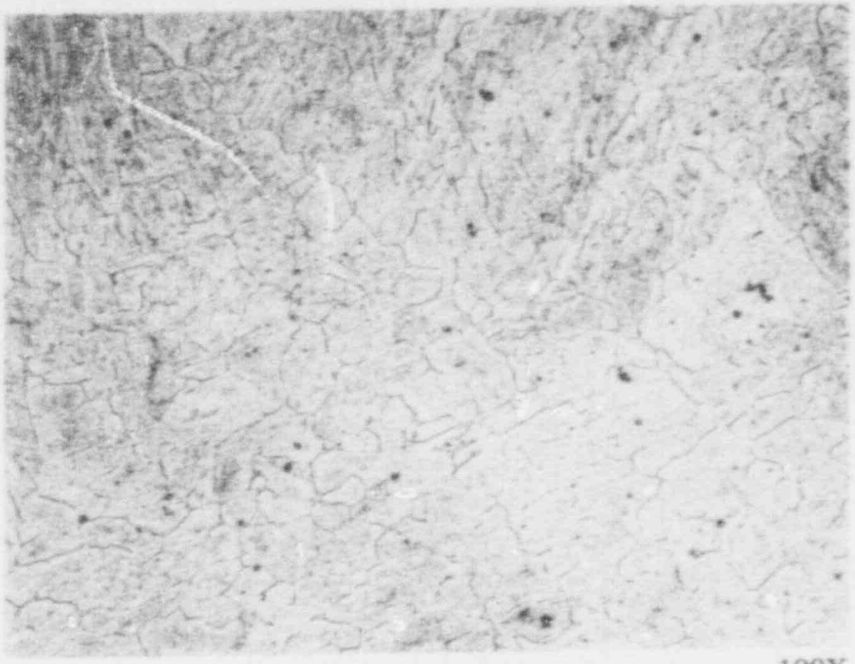

47196 100X

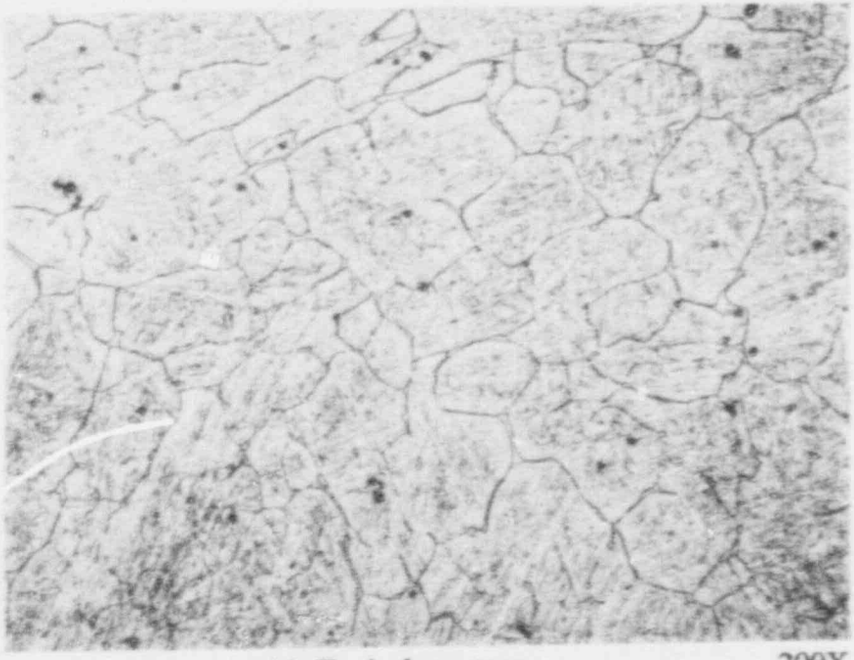

47195 (a) Typical structure. 200X

47193 100X

(b) Localized directional features.

FIGURE B-6. MICROSTRUCTURE OF SAMPLE NO. 243 (8-in.). Etchant: Vilella's reagent

47272 100X

47273 200X

FIGURE B-7. TYPICAL MICROSTRUCTURE OF SAMPLE NO. 244 (6-in.). See Figure B-8. Etchant: Vilella's reagent

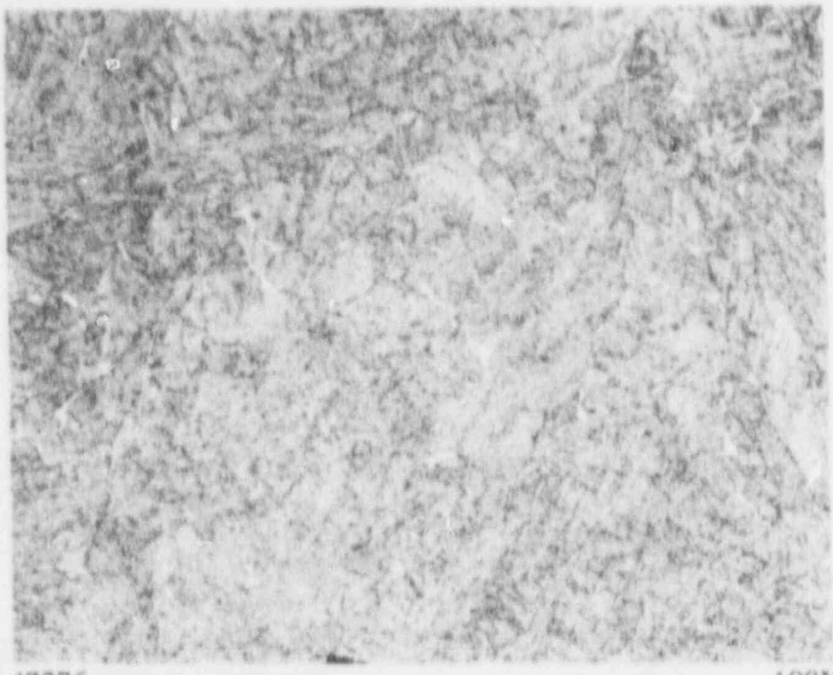

47276 100X

47275 200X

FIGURE B-8. MICROSTRUCTURE OF SAMPLE NO. 244 (6-in.).
See Figure B-7. Etchant: Vilella's reagent

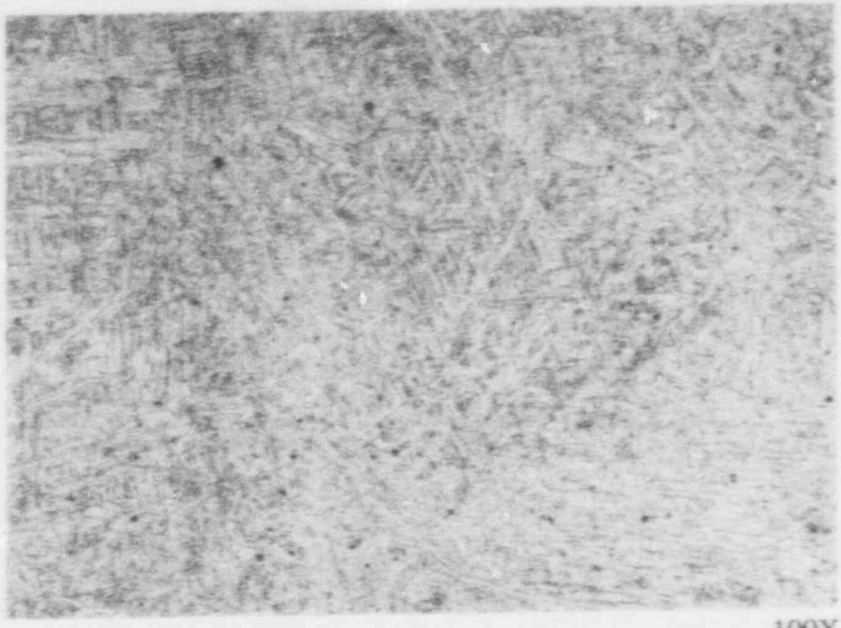

47278 100X

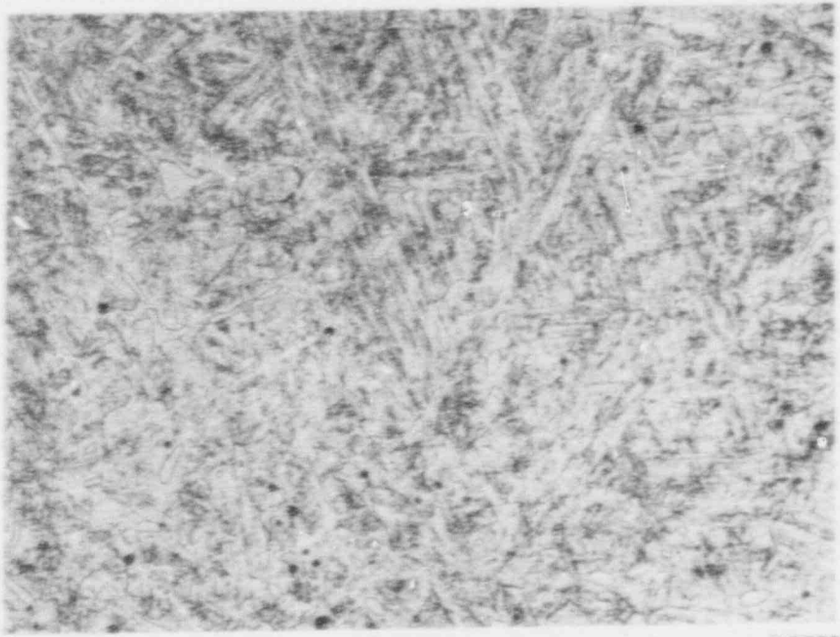

47277 (a) Typical structure. 200X

47280 (b) 100X

FIGURE B-9. MICROSTRUCTURE OF SAMPLE NO. 256 (6-in.). Etchant: Vilella's reagent

47309 100X

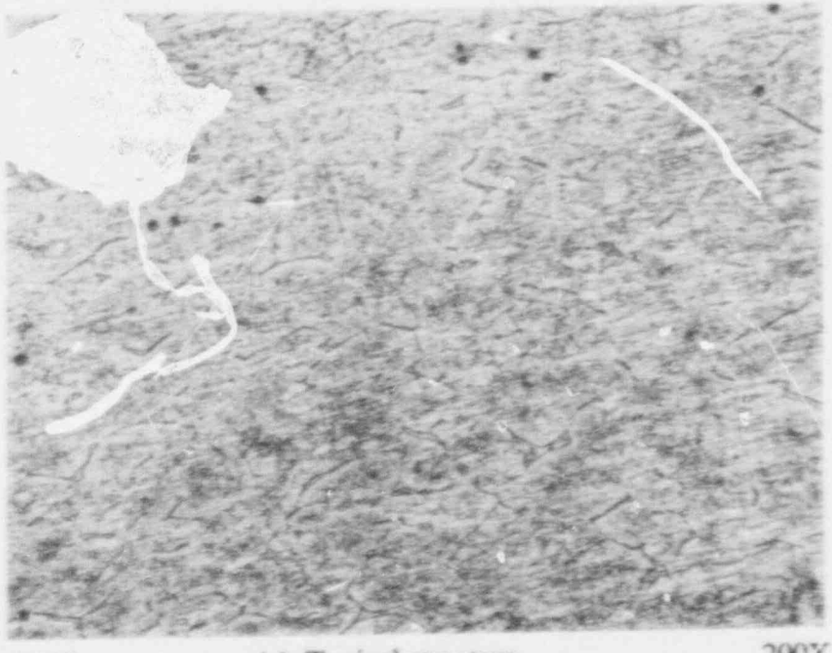

47310 (a) Typical structure. 200X

47307 (b) 100X

FIGURE B-10. MICROSTRUCTURE OF SAMPLE NO. 257 (6-in.). Etchant: Vilella's reagent

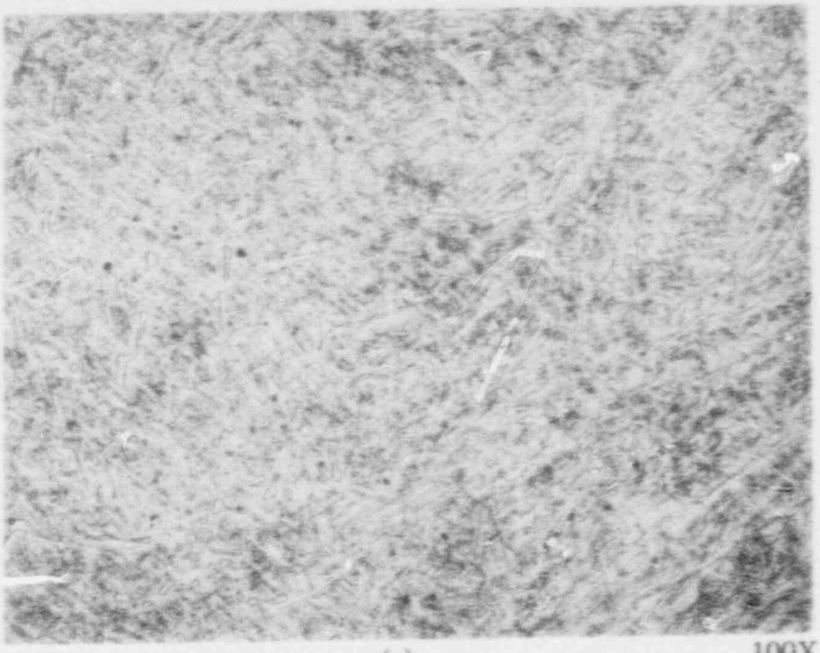

47375 (a) 100X

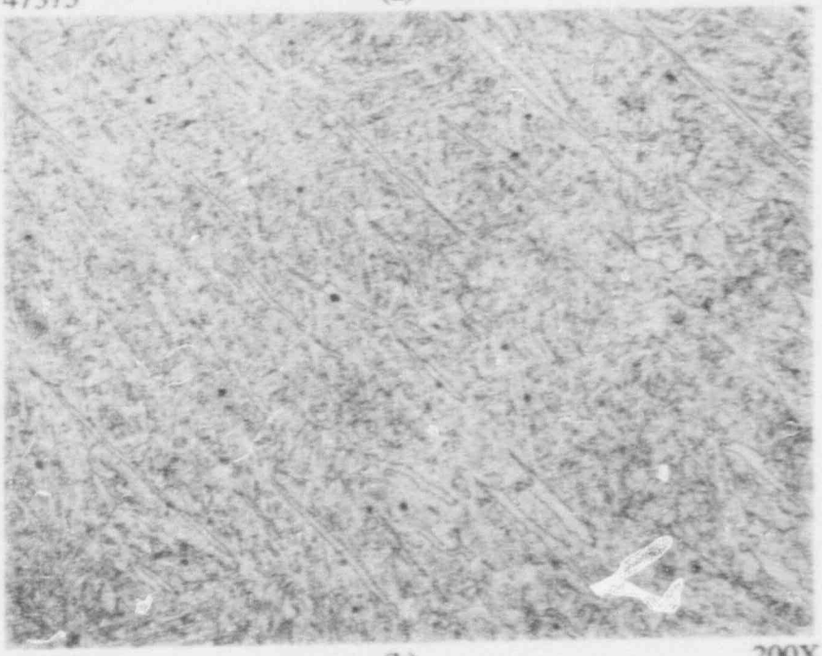

47378 (b) 200X

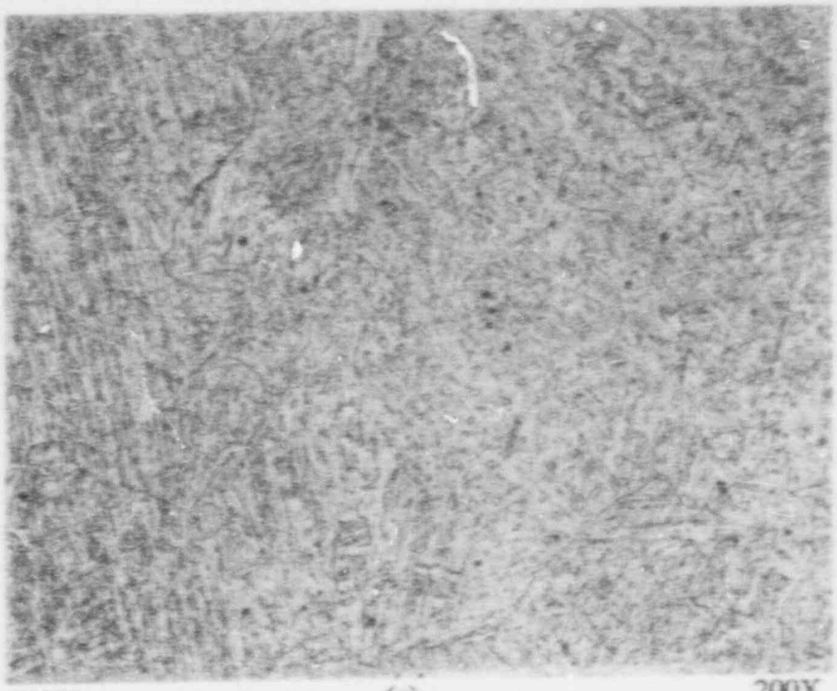

47374 (c) 200X

FIGURE B-11. MICROSTRUCTURE OF SAMPLE NO. 245 (4-in.). Etchant: Vilella's reagent

47384 (a) 100X

47385 (b) 200X

47386 (c) 200X

FIGURE B-12. MICROSTRUCTURE OF SAMPLE NO. 258 (4-in.). Etchant: Vilella's reagent

47388 100X

47387 200X

FIGURE B-13. TYPICAL MICROSTRUCTURE OF SAMPLE NO. 259 (4-in.). Etchant: Vilella's reagent

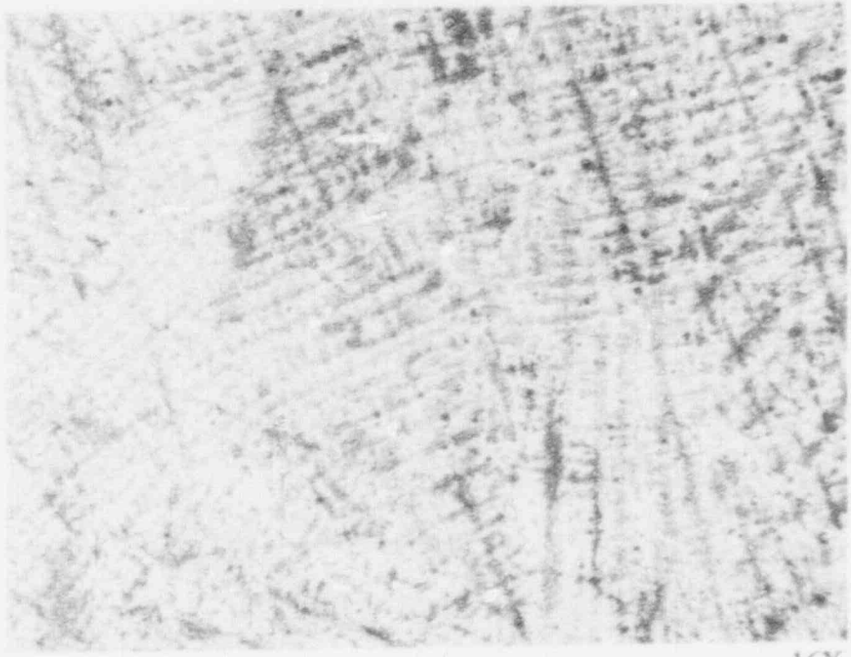

47369 (a) 16X

47370 (b) 50X

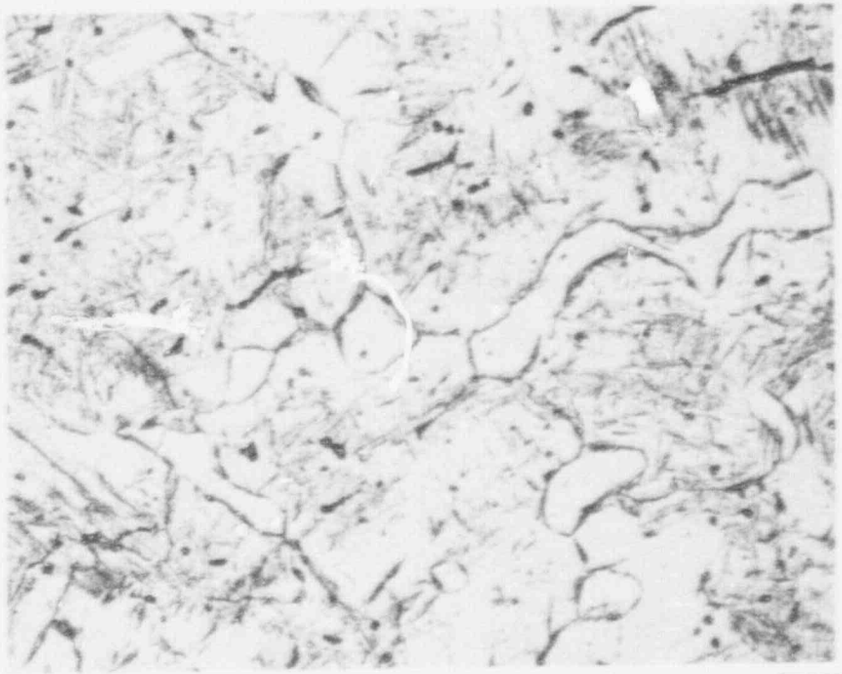

47372 (c) 200X

FIGURE B-14. MICROSTRUCTURE OF SAMPLE NO. 260 (4-in.). Etchant: Vilella's reagent

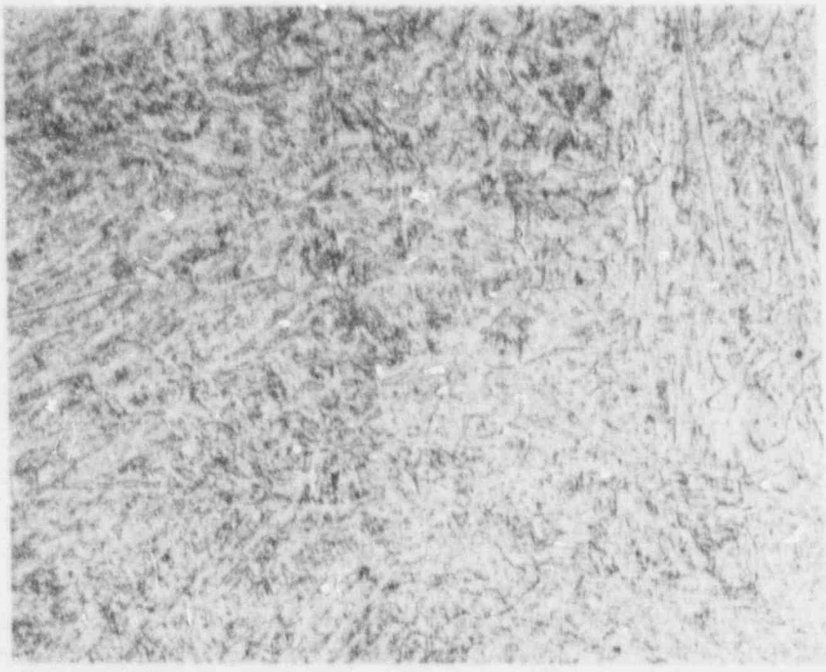

47483 200X

47484 500X

FIGURE B-15. TYPICAL MICROSTRUCTURE OF SAMPLE NO. 246 (3-in.). Etchant: Vilella's reagent

47486 200X

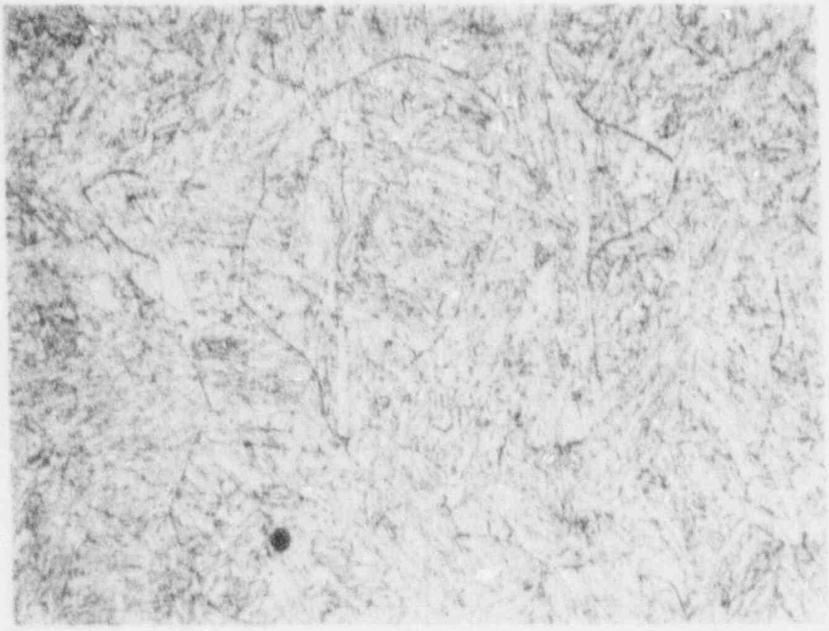

47487 500X

FIGURE B-16. TYPICAL MICROSTRUCTURE OF SAMPLE NO. 261 (3-in.). Etchant: Vilella's reagent

47491

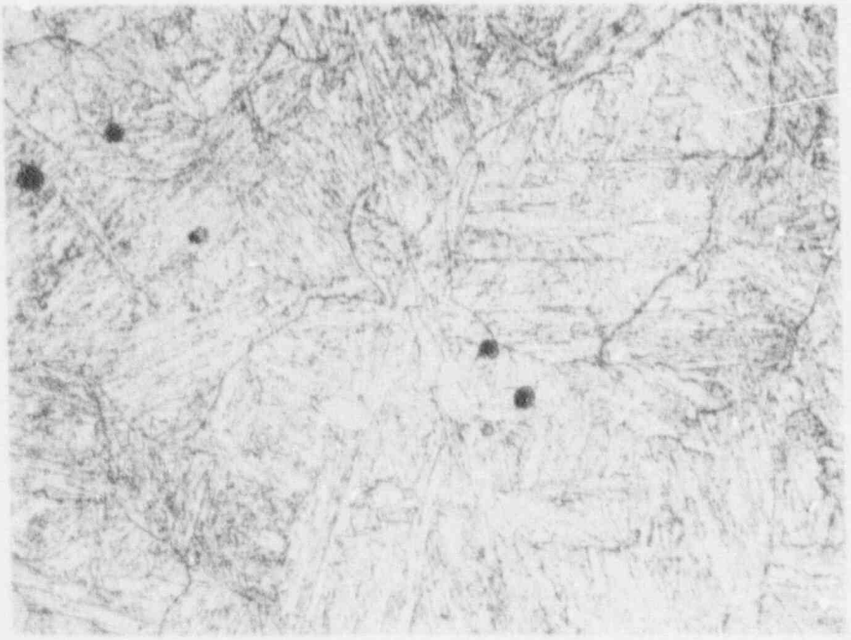

47492 500X

FIGURE B-17. TYPICAL MICROSTRUCTURE OF SAMPLE NO. 262 (3-in.). Etchant: Vilella's reagent

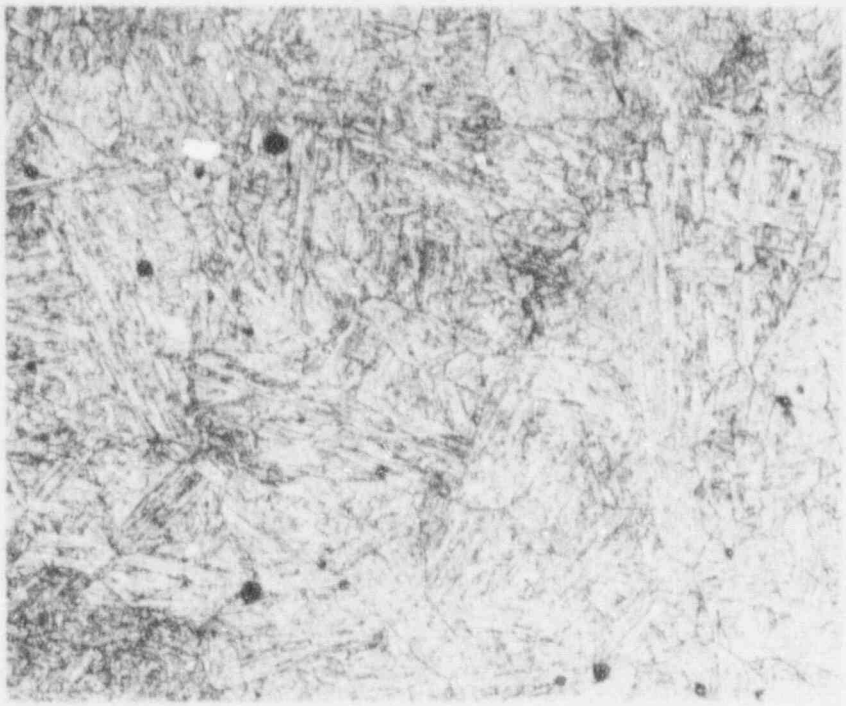

47479 200X

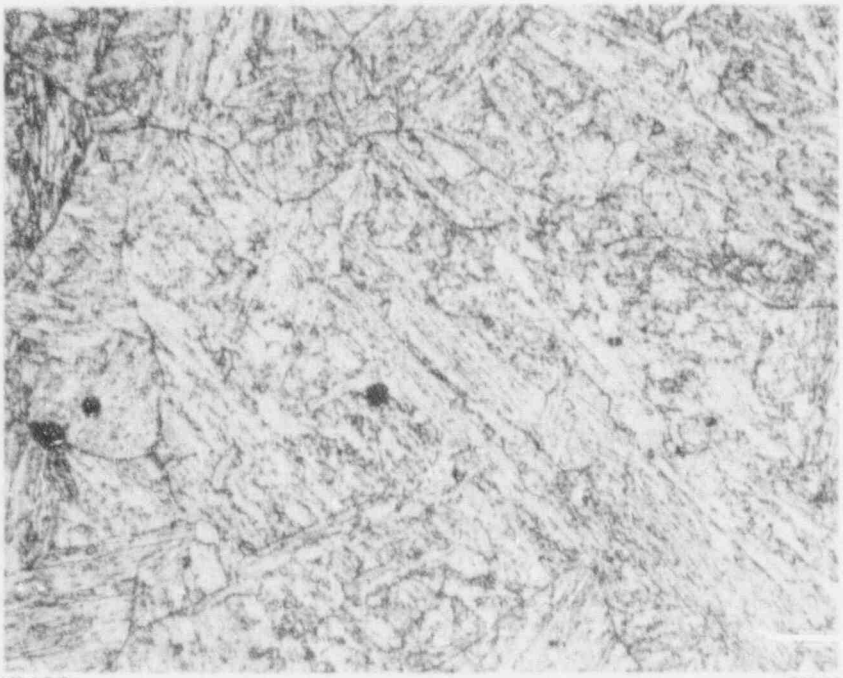

47480 500X

FIGURE B-18. TYPICAL MICROSTRUCTURE OF SAMPLE NO. 263 (3-in.). Etchant: Vilella's reagent

APPENDIX C

EQUATION FOR THE STRESS INTENSITY FACTOR (K_I) FOR A SURFACE CRACK

The development of the equation for the stress intensity factor for a surface crack, abstracted from Newman and Raju [1] is presented below. The equation is developed for the general case of a semi-elliptical surface crack in a member with a rectangular cross section, subjected to combined bending and uniform tensile stresses.

The notations for the deviation are as follows:

S_t	=	remote uniform tensile stress	2c	=	crack length
S_b	=	remote outer fiber bending stress	ϕ	=	parametric angle of ellipse
t	=	section thickness	Q	=	crack geometry factor
2b	=	section width	and F and H	=	boundary correction functions

For the special case of pure bending and K_{Imax} at $\phi = \frac{\pi}{2}$, the generalized equation reduces to that shown in Section 5.3 of this report.

STRESS-INTENSITY FACTOR EQUATION FOR THE SURFACE CRACK

An empirical equation for the stress-intensity factors for a surface crack in a finite plate subjected to tension and bending loads has been fitted to the finite-element results from Raju and Newman[5-7] for a/c values from 0.2 to 1.0. To account for the limiting behavior as a/c approaches zero, the results of Gross and Srawley[8] for a single-edge crack have also been used. Two types of loads were applied to the surface-cracked plate: remote uniform tension and remote bending. The remote uniform-tension stress is S_t in Fig. 2(a); the remote outer-fiber bending stress S_b in Fig. 2(b) is calculated from the applied bending moment M. The stress-intensity factor equation for combined tension and bending loads is

$$K_I = (S_t + HS_b)\sqrt{\pi \frac{a}{Q}}\, F\left(\frac{a}{t}, \frac{a}{c}, \frac{c}{b}, \phi\right) \qquad (1)$$

for $0 < a/c \leq 1.0$, $0 \leq a/t \leq 1.0$, $c/b < 0.5$ and $0 \leq \phi \leq \pi$. A useful approximation for Q,

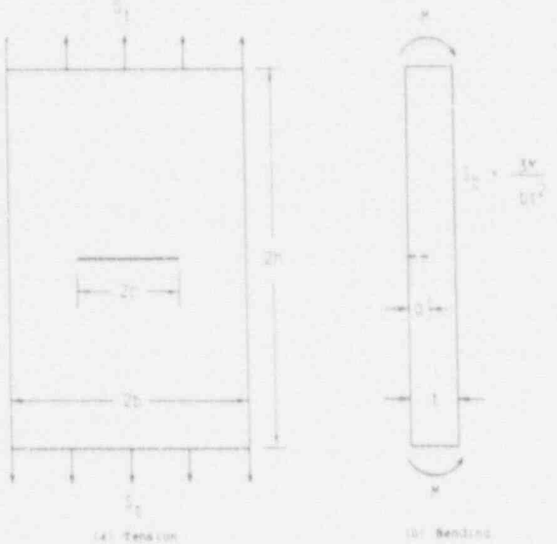

(a) Tension (b) Bending

Fig. 2. Surface-cracked plate subjected to tension or bending loads

developed by Rawe and used in Ref. [9], is

$$Q = 1 + 1.464\left(\frac{a}{c}\right)^{1.65} \quad \left(\frac{a}{c} \leq 1\right). \tag{2}$$

The functions F and H are defined so that the boundary-correction factor for tension is equal to F and the boundary-correction factor for bending is equal to the product of H and F. The function F was obtained from a systematic curve-fitting procedure by using double-series polynomials in terms of a/c, a/t, and angular functions of ϕ. The choice of functions was based on engineering judgment. The function F was taken to be

$$F = \left[M_1 + M_2\left(\frac{a}{t}\right)^2 + M_3\left(\frac{a}{t}\right)^4\right] f_\phi g f_w \tag{3}$$

where

$$M_1 = 1.13 - 0.09\left(\frac{a}{c}\right) \tag{4}$$

$$M_2 = -0.54 + \frac{0.89}{0.2 + (a/c)} \tag{5}$$

$$M_3 = 0.5 - \frac{1.0}{0.65 + (a/c)} + 14\left(1.0 - \frac{a}{c}\right)^{24} \tag{6}$$

$$g = 1 + \left[0.1 + 0.35\left(\frac{a}{t}\right)^2\right](1 - \sin\phi)^2. \tag{7}$$

The function f_ϕ, an angular function from the embedded elliptical-crack solution[10], is

$$f_\phi = \left[\left(\frac{a}{c}\right)^2 \cos^2\phi + \sin^2\phi\right]^{1/4} \tag{8}$$

The function f_w, a finite-width correction from Ref. [11], is

$$f_w = \left[\sec\left(\frac{\pi c}{2b}\sqrt{\frac{a}{t}}\right)\right]^{1/2} \tag{9}$$

The function H, developed herein also by curve fitting and engineering judgment, has the form

$$H = H_1 + (H_2 - H_1)\sin^p\phi \tag{10}$$

where

$$p = 0.2 + \frac{a}{c} + 0.6\frac{a}{t} \tag{11}$$

$$H_1 = 1 - 0.34\frac{a}{t} - 0.11\frac{a}{c}\left(\frac{a}{t}\right) \tag{12}$$

$$H_2 = 1 + G_1\left(\frac{a}{t}\right) + G_2\left(\frac{a}{t}\right)^2 \tag{13}$$

In this equation for H_2,

$$G_1 = -1.22 - 0.12\frac{a}{c} \tag{14}$$

$$G_2 = 0.55 - 1.05\left(\frac{a}{c}\right)^{0.75} + 0.47\left(\frac{a}{c}\right)^{1.5}. \tag{15}$$

APPENDIX D

LOWER BOUND VALUE FOR THE FRACTURE TOUGHNESS TEST DATA BY USING STATISTICAL METHODOLOGY APPROACH

by

Tony Yi Torng

1. INTRODUCTION

The questions arises as to what would be the lowest fracture toughness expected from any swing arm that has not yet been replaced. In order to search for an appropriate lower bound value for the sixteen experimental fracture toughness tests, the statistical methodology approach is the most reasonable tool. The purpose of this analysis is to provide some statistical assessments and to select the most reasonable characterization of the data. Inherent statistical uncertainty can be characterized, for purposes of analysis, by an analytical model describing the distribution, based on a random sample of data. But the choice of a distribution is very subjective and not at all reliable. It is necessary to determine which of the several competing statistical models best fit a random sample of data by using a goodness of fit test methodology. After the distribution model and corresponding parameters (mean and standard deviation) are determined, a one-sided α% lower bound with γ% of confidence can be identified. This lower bound can also be called the "tolerance limit." The reason for using this tolerance limit is due to its ability to provide a certain confidence in handling the uncertainty. Note that there still exists some finite possibility of finding values below the chosen limit, no matter how small the limit is. In other words, the choice of the limit depends on engineering judgement, since there are lower limits to which K_{IC} values can occur.

2. MODEL PARAMETER CALCULATION

A total of five distributions have been selected for this study. They are Normal, Lognormal, Weibull, and Extreme Value Distribution (EVD). The parameters for each distribution are calculated using the maximum likelihood method. These parameters and the corresponding cumulative distribution function (CDF) are summarized as follows:

a. Normal

$$\mu(\text{mean}) = 79.1$$

$$\sigma(\text{standard deviation}) = 18.76$$

$$\text{CDF} = \Phi\left(\frac{X - \mu}{\sigma}\right)$$

b. Lognormal

$$\mu_{log}(\text{mean}) = 4.345$$

$$\sigma_{log}(\text{Standard Deviation}) = 0.22985$$

$$\text{CDF} = \Phi\left(\frac{\log(X) - \mu_{log}}{\sigma_{log}}\right)$$

c. Weibull

$$\alpha = 4.16519$$

$$\beta = 86.42621$$

$$\text{CDF} = 1 - \exp^{-\left[\left(\frac{x}{\beta}\right)^{\alpha}\right]}$$

d. EVD

$$\alpha = 0.06176$$

$$\beta = 70.62699$$

$$\text{CDF} = \exp[-\exp(-\alpha(X - \beta))]$$

where X represents the fracture toughness random variable.

3. MODEL SELECTION

To determine the most appropriate model, a goodness of fit test using Cramer-Von Mises statistics was applied. The test uses a statistical value W_i to select the model and is defined as

$$W_i^2 = \frac{1}{N} \sum_{i=1}^{N} D_{ij}^2$$

where

$$D_{ij} = G_j\left(X_i ; \hat{\underset{\sim}{\Theta}}\right) - F_i$$

$G_j\left(X_i ; \hat{\underset{\sim}{\Theta}}\right)$ is the cumulative distribution function (CDF) of the defined distribution model, $\hat{\underset{\sim}{\Theta}}$ is the maximum likelihood estimate of the model, N is the total number of data points, and F_i is the empirical CDF defined as

$$F_i = \frac{i - 1/2}{N} \quad , \quad i = 1, N$$

All the CDF values including the empirical values are listed in Table D-1. Based on the results of the statistics; EVD produces the best fit.

Table D-1

	Data	Empirical CDF	Normal	Lognormal	Weibull	EVD
1	53.5	3.125%	8.64%	5.60%	12.68%	5.610%
2	57.1	9.375%	12.08%	9.57%	16.30%	9.960%
3	63.8	15.625%	20.79%	20.51%	24.60%	21.770%
4	65.4	21.875%	23.32%	23.71%	26.88%	25.130%
5	65.6	28.125%	23.64%	24.12%	27.18%	25.560%
6	67.4	34.375%	26.91%	27.96%	29.88%	29.500%
7	70.1	40.625%	31.64%	33.96%	34.16%	35.590%
8	74.2	46.875%	39.77%	43.39%	41.12%	44.840%
9	74.2	53.125%	39.77%	43.39%	41.12%	44.840%
10	78.2	59.375%	48.10%	52.47%	48.28%	53.450%
11	81.1	65.625%	54.32%	58.73%	53.57%	59.230%
12	87.8	71.875%	67.93%	71.42%	65.60%	70.730%
13	100.4	78.125%	87.23%	87.48%	84.50%	85.290%
14	101.2	84.375%	88.10%	88.17%	85.47%	85.950%
15	109.7	90.625%	94.80%	93.76%	93.27%	91.435%
16	115.3	96.875%	97.32%	96.00%	96.39%	93.860%
$W_i =$			0.07241	0.05303	0.07254	0.04502

4. TOLERANCE LIMIT

It is obvious that when only sixteen samples are available, the sample mean and sample standard deviation are themselves random variables. Thus, there is uncertainty in the parameters themselves, which is reflected in the corresponding lower bound of the data. The tolerance limit is the value above which we may predict with α% confidence that γ% of the population will lie, that is,

$$Prob_{\alpha\%}(X_L < X < X_U) \quad = \quad \gamma\%$$

where X_L and X_U represent the lower and upper bounds of the predicted variable, X. For analyzing fracture toughness data, we are concerned only about the lower bound; therefore, we expect to construct the following:

$$Prob_{\alpha\%}(X > X_L) \quad = \quad \gamma\%$$

In References D-1 and D-2, tolerance limit tables for Normal distributions are given. However, the EVD distribution was selected to best represent the data. To simplify the estimation of the tolerance limit, a simple assumption has been made for both types of distributions, that is:

> The uncertainty occurring in the Normal distribution will be applied to the other distribution types, by assuming the cumulative distribution value at the lower bound of the Normal distribution is the same for other distribution types. The first step is to find the K value from the tolerance limit table, based on the required population and confidence, and find the corresponding CDF value,
>
> $$cdf \quad = \quad \Phi\left(\frac{X_{LN} - \mu_N}{\sigma_N}\right) \quad = \quad \Phi(-K)$$
>
> where Φ is the cumulative distribution function for the standard Normal, μ_N and σ_N are the mean and standard deviation values of the Normal distribution, and X_{LN} is the lower bound value for the Normal distribution. Based on this assumption, the lower bound value, X_L for other distributions can be solved by the following function:
>
> $$F(X_L) \quad = \quad \Phi(-K)$$
>
> where $F(X_L)$ represents the CDF function for other distributions.

This assumption was proven by using the Lognormal distribution to run a Monte Carlo simulation program to compare with the Normal distribution results. Based on the comparison, it shows the assumption was accurate.

According to the assumption, several levels of population and confidence are solved using the Normal (for comparison) and the EVD distributions, as shown in Table D-2.

Table D-2

Lower Bound	Normal	EVD
90% confidence 90% population K = 1.842	44.54	50.72
90% confidence 95% population K = 2.299	35.97	46.15
90% confidence 99% population K = 3.172	19.59	38.69
95% confidence 90% population K = 2.032	40.98	49.03
95% confidence 95% population K = 2.523	31.76	44.09
95% confidence 99% population K = 3.463	14.13	36.5
99% confidence 90% population K = 2.458	32.99	44.67
99% confidence 95% population K = 3.028	22.29	39.83
99% confidence 99% population K = 4.124	1.734	31.96

5. SUMMARY AND DISCUSSION

Based on the results shown in Table D-2, the following observations are evident:

- The Normal model predicts smaller lower bounds of K_{IC}, thus, leading to overly conservative results.

- The EVD provides the best goodness of fit to the data. It is seen that for the 99% confidence and 99% population case, the EVD predicts a lower bound of fracture toughness of about 32.0 ksi$\sqrt{in}$.

From the statistical distributions evaluated, we can thus predict with 99% confidence that 99% of the remaining swing arms presently in service have fracture toughness values greater than 32.0 ksi$\sqrt{in}$. Other values of the lower bound for different confidence levels and different population levels are given in Table D-2.

6. REFERENCES

D-1. Hine., W.W., And Montgomery, D.C., **Probability and Statistics in Engineering and Management Science**, John Wiley, 1980.

D-2. Wirsching, P.H., **Reliability Methods in Mechanical and Structural Design**, class note, University of Arizona, 1985.